

Evaporative drying from hydrophilic and hydrophobic single pores and porous media

by

Partha Pratim Chakraborty

B.S., Chittagong University of Engineering and Technology, 2015

AN ABSTRACT OF A DISSERTATION

submitted in partial fulfillment of the requirements for the degree

DOCTOR OF PHILOSOPHY

Alan Levin Department of Mechanical and Nuclear Engineering
Carl R. Ice College of Engineering

KANSAS STATE UNIVERSITY
Manhattan, Kansas

2022

Abstract

Reduction of water usage is a challenging issue in food-energy-water nexus; approximately two-thirds of the global water withdrawals are responsible for food production, and water withdrawals are predicted to increase in the future to produce more food to meet the demands of a growing global population, projected to reach 9.8 billion by 2050. Arid or semi-arid areas are facing increasing pressure for water resources, yet irrigation is critical for increasing yields; 20% of global land is irrigated, but it accounts for 40% of crop production [1]. One approach to conserving soil moisture is to restrict evaporation by altering soil wettability. Any material can be classified into two categories of wettability: hydrophilic (i.e., water loving) and hydrophobic (i.e., water repelling), and the wettability is measured using the contact angle (i.e., the angle formed by the liquid at the solid-liquid-vapor interface) of liquid droplets. For hydrophilic surfaces, the contact angle is less than 90° , and for hydrophobic surfaces, it is greater than 90° . Wettability impacts evaporation; previous studies indicated that inclusion of hydrophobicity can reduce evaporation rates by 50-65% in a porous media.

In this dissertation, the impacts of wettability on evaporation of water from porous media were investigated from single pores and porous media. The evaporation phenomena were studied from simulated soil pores created with three hydrophilic glass 2.38-mm-diameter spheres or three hydrophobic 2.38-mm-diameter spheres. Water droplets (i.e., 4- μL) were evaporated from the pore in three different experiments. Experimental conditions were varied, including air temperatures (i.e., 20-22.2 $^\circ\text{C}$), relative humidities (RH) (i.e., 30%, 45%, 60%, and 75% RH), and single pore geometries [i.e., center-to-center distances of the spheres (i.e., 2.7 mm, 2.8 mm, 3.13 mm)]. The relative humidity played a role in droplet evaporation, as evaporation rates were slower at higher RH. For all cases, the wettability impacted the droplet evaporation. At each relative humidity level

set for experiments (i.e., 30%, 45%, 60% and 75%), the evaporation rates were 1.11-1.47 times higher for hydrophilic pores than hydrophobic pores. The pore size also affected the evaporation phenomena, as the evaporation rates were 1.23-1.3 times higher for larger pore sizes (e.g., center-to-center distances of 3.13 mm compared to 2.7, 2.8 mm) at 20°C, 60% RH.

Evaporation from single pores was observed using a high-speed camera. Wettability impacted the contact line movement, including pinning (i.e., solid-liquid-vapor contact lines do not move) and depinning (i.e., solid-liquid-vapor contact lines move). In glass pores comprised of three spheres, the solid-liquid-vapor contact line on one sphere was pinned and the contact line depinned on the remaining two spheres, resulting in contact line motion. In Teflon pores comprised of three spheres, all solid-liquid-vapor contact lines on each of the three spheres decreased with time. During evaporation, the whole droplet eventually ruptured and created a liquid island between two of the three spheres. Liquid islands formed between two spheres and in an isothermal condition both radii of curvature of the liquid islands decreased in size due to evaporation.

Subsequently, evaporation from simulated soil columns was investigated to understand evaporation dynamics and evaporation stages in multi-layered porous media. In a typical porous media, three different evaporation stages are found: constant rate period, falling rate period and subsequent slower rate period. In the constant rate period, the porous media remains saturated, and water is evaporated from the surface by means of natural or forced convection maintaining a constant rate. The constant rate continues until the water can move to the top surface by action of capillary force. The depth of drying front at the end of constant rate is marked as the characteristic length which is defined as the maximum hydraulically connected region from the evaporative front to the top surface. When this hydraulic connection breaks down, the evaporation rate experiences a sharp decrease, defined as the falling rate period, where liquid islands are formed throughout the

porous section. When the liquid islands rupture, the evaporation rate further reduces; this is defined as the slower rate period of evaporation. For multi-layered porous media, two different columns (i.e., hydrophilic and hydrophobic) were prepared. Approximately 1320 glass or Teflon 2.38-mm-diameter spheres were filled in 6-cm-height, 1.88-cm-diameter glass beakers. During these experiments, a heat flux of 1000 W/m^2 was applied using a solar simulator and 5 mL of water out of a total of 5.8 mL was evaporated. Experiments were conducted for seven days, and each experiment was replicated five times. The evaporative mass loss was recorded with a sensitive scale ($\pm 0.01 \text{ g}$) and the evaporation rates were measured at 22.2°C , 60% RH. The initial evaporation rate was 1.5 times higher in hydrophilic column (e.g., 7.5 mm/day) than the hydrophobic column (e.g., 5 mm/day).

In the experiments with hydrophilic or hydrophobic porous columns, different evaporation stages were analyzed. Due to homogeneity of the porous column, the constant rate period of evaporation was insignificant for both glass and Teflon spheres. From the very beginning, the evaporation experienced a sharp decrease (i.e., the falling rate period) and, subsequently, the slower period of evaporation for both glass and Teflon samples. The evaporative mass loss was greater in glass (i.e., 3 g) sample than the Teflon (i.e., 2.4 g) after seven days of experiment, indicating higher evaporation rate from hydrophilic porous media. The drying front, the distance from the unsaturated part to the saturated portion of the porous media, was visualized and captured with a high-resolution x-ray from the third day until seventh day of evaporation. The drying front propagated faster in glass sample than Teflon.

Evaporation of water from three hydrophilic homogeneous 3D-printed structures made with translucent acrylonitrile butadiene styrene (ABS) plastic was conducted at 22.2°C , 13-17% RH with the application of 1000 W/m^2 heat flux on the top surface. Two structures, 3D structure-

1 and 2, had the same dimensions (i.e., $L = 8.35$ mm, $W = 8.35$ mm, $H = 14.07$ mm) with similar effective pore sizes of 0.41 mm. The only difference between the two structures was in 3D structure-2, two layers in the y - z direction were filled with material to restrict lateral interactions of water. The 3D structure-3 ($L = 11.19$ mm, $W = 11.19$ mm, $H = 19.2$ mm) was more complex in design with cross-shaped cylinders connecting the spheres in all directions, making the effective pore radius 0.16 mm; 3D structure-3 held more water (i.e., 0.8 g) than the other two (i.e., 0.44 g for 3D structure-1 and 0.3 g for 3D structure-2), but the evaporation rate was faster due to larger the evaporative surface and lower pore size leading to extend period of constant rate of evaporation. The drying front depths was visualized with a high-speed camera, and they were also calculated from transient saturation. The evaporation rates from the three 3D structures were calculated and a steady-state energy balance was modeled to predict the evaporative mass loss flux from the porous structures.

Evaporative drying from hydrophilic and hydrophobic single pores and porous media

by

Partha Pratim Chakraborty

B.S., Chittagong University of Engineering and Technology, 2015

A DISSERTATION

submitted in partial fulfillment of the requirements for the degree

DOCTOR OF PHILOSOPHY

Alan Levin Department of Mechanical and Nuclear Engineering
Carl R. Ice College of Engineering

KANSAS STATE UNIVERSITY
Manhattan, Kansas

2022

Approved by:

Major Professor
Melanie M. Derby

Copyright

© Partha Chakraborty 2022.

Abstract

Reduction of water usage is a challenging issue in food-energy-water nexus; approximately two-thirds of the global water withdrawals are responsible for food production, and water withdrawals are predicted to increase in the future to produce more food to meet the demands of a growing global population, projected to reach 9.8 billion by 2050. Arid or semi-arid areas are facing increasing pressure for water resources, yet irrigation is critical for increasing yields; 20% of global land is irrigated, but it accounts for 40% of crop production [1]. One approach to conserving soil moisture is to restrict evaporation by altering soil wettability. Any material can be classified into two categories of wettability: hydrophilic (i.e., water loving) and hydrophobic (i.e., water repelling), and the wettability is measured using the contact angle (i.e., the angle formed by the liquid at the solid-liquid-vapor interface) of liquid droplets. For hydrophilic surfaces, the contact angle is less than 90° , and for hydrophobic surfaces, it is greater than 90° . Wettability impacts evaporation; previous studies indicated that inclusion of hydrophobicity can reduce evaporation rates by 50-65% in a porous media.

In this dissertation, the impacts of wettability on evaporation of water from porous media were investigated from single pores and porous media. The evaporation phenomena were studied from simulated soil pores created with three hydrophilic glass 2.38-mm-diameter spheres or three hydrophobic 2.38-mm-diameter spheres. Water droplets (i.e., 4- μL) were evaporated from the pore in three different experiments. Experimental conditions were varied, including air temperatures (i.e., 20-22.2 $^\circ\text{C}$), relative humidities (RH) (i.e., 30%, 45%, 60%, and 75% RH), and single pore geometries [i.e., center-to-center distances of the spheres (i.e., 2.7 mm, 2.8 mm, 3.13 mm)]. The relative humidity played a role in droplet evaporation, as evaporation rates were slower at higher RH. For all cases, the wettability impacted the droplet evaporation. At each relative humidity level

set for experiments (i.e., 30%, 45%, 60% and 75%), the evaporation rates were 1.11-1.47 times higher for hydrophilic pores than hydrophobic pores. The pore size also affected the evaporation phenomena, as the evaporation rates were 1.23-1.3 times higher for larger pore sizes (e.g., center-to-center distances of 3.13 mm compared to 2.7, 2.8 mm) at 20°C, 60% RH.

Evaporation from single pores was observed using a high-speed camera. Wettability impacted the contact line movement, including pinning (i.e., solid-liquid-vapor contact lines do not move) and depinning (i.e., solid-liquid-vapor contact lines move). In glass pores comprised of three spheres, the solid-liquid-vapor contact line on one sphere was pinned and the contact line depinned on the remaining two spheres, resulting in contact line motion. In Teflon pores comprised of three spheres, all solid-liquid-vapor contact lines on each of the three spheres decreased with time. During evaporation, the whole droplet eventually ruptured and created a liquid island between two of the three spheres. Liquid islands formed between two spheres and in an isothermal condition both radii of curvature of the liquid islands decreased in size due to evaporation.

Subsequently, evaporation from simulated soil columns was investigated to understand evaporation dynamics and evaporation stages in multi-layered porous media. In a typical porous media, three different evaporation stages are found: constant rate period, falling rate period and subsequent slower rate period. In the constant rate period, the porous media remains saturated, and water is evaporated from the surface by means of natural or forced convection maintaining a constant rate. The constant rate continues until the water can move to the top surface by action of capillary force. The depth of drying front at the end of constant rate is marked as the characteristic length which is defined as the maximum hydraulically connected region from the evaporative front to the top surface. When this hydraulic connection breaks down, the evaporation rate experiences a sharp decrease, defined as the falling rate period, where liquid islands are formed throughout the

porous section. When the liquid islands rupture, the evaporation rate further reduces; this is defined as the slower rate period of evaporation. For multi-layered porous media, two different columns (i.e., hydrophilic and hydrophobic) were prepared. Approximately 1320 glass or Teflon 2.38-mm-diameter spheres were filled in 6-cm-height, 1.88-cm-diameter glass beakers. During these experiments, a heat flux of 1000 W/m^2 was applied using a solar simulator and 5 mL of water out of a total of 5.8 mL was evaporated. Experiments were conducted for seven days, and each experiment was replicated five times. The evaporative mass loss was recorded with a sensitive scale ($\pm 0.01 \text{ g}$) and the evaporation rates were measured at 22.2°C , 60% RH. The initial evaporation rate was 1.5 times higher in hydrophilic column (e.g., 7.5 mm/day) than the hydrophobic column (e.g., 5 mm/day).

In the experiments with hydrophilic or hydrophobic porous columns, different evaporation stages were analyzed. Due to homogeneity of the porous column, the constant rate period of evaporation was insignificant for both glass and Teflon spheres. From the very beginning, the evaporation experienced a sharp decrease (i.e., the falling rate period) and, subsequently, the slower period of evaporation for both glass and Teflon samples. The evaporative mass loss was greater in glass (i.e., 3 g) sample than the Teflon (i.e., 2.4 g) after seven days of experiment, indicating higher evaporation rate from hydrophilic porous media. The drying front, the distance from the unsaturated part to the saturated portion of the porous media, was visualized and captured with a high-resolution x-ray from the third day until seventh day of evaporation. The drying front propagated faster in glass sample than Teflon.

Evaporation of water from three hydrophilic homogeneous 3D-printed structures made with translucent acrylonitrile butadiene styrene (ABS) plastic was conducted at 22.2°C , 13-17% RH with the application of 1000 W/m^2 heat flux on the top surface. Two structures, 3D structure-

1 and 2, had the same dimensions (i.e., $L = 8.35$ mm, $W = 8.35$ mm, $H = 14.07$ mm) with similar effective pore sizes of 0.41 mm. The only difference between the two structures was in 3D structure-2, two layers in the y - z direction were filled with material to restrict lateral interactions of water. The 3D structure-3 ($L = 11.19$ mm, $W = 11.19$ mm, $H = 19.2$ mm) was more complex in design with cross-shaped cylinders connecting the spheres in all directions, making the effective pore radius 0.16 mm; 3D structure-3 held more water (i.e., 0.8 g) than the other two (i.e., 0.44 g for 3D structure-1 and 0.3 g for 3D structure-2), but the evaporation rate was faster due to larger the evaporative surface and lower pore size leading to extend period of constant rate of evaporation. The drying front depths was visualized with a high-speed camera, and they were also calculated from transient saturation. The evaporation rates from the three 3D structures were calculated and a steady-state energy balance was modeled to predict the evaporative mass loss flux from the porous structures.

Table of Contents

List of Figures	xv
List of Tables	xx
Acknowledgements	xxi
Dedication	xxii
Preface	xxiii
Chapter 1 - Introduction	1
Chapter 2 - Literature Review	3
2.1 Evaporative drying from flat surface	4
2.1.1 Estimation of contact angle in different wettable material	4
2.1.2 Contact line dynamics: Pinning and depinning of hydrophilic and hydrophobic material	8
2.1.3 Modeling of evaporation of sessile droplet from flat surface	10
2.2 Liquid islands formed in a single pore	13
2.3 Evaporation from porous media	15
2.3.1 Evaporation from porous packed beds made with spheres	16
2.3.2 Evaporation from 2D porous networks	18
2.3.3 Evaporation from sand/soil columns	20
2.4 Research objectives	21
Chapter 3 - Experimental apparatus	23
3.1 Evaporation of sessile droplet from single pores	23
3.1.1 Physical properties of glass and Teflon spheres	26
3.2 Evaporation from simulated soil columns	28
3.2.1 Evaporation from small hydrophilic porous column	28
3.2.2 Evaporation from hydrophilic and hydrophobic porous column to study effects of wettability	30
3.2.3 X-ray image capturing technique	32
3.2.4 X-ray image post-processing	33
3.3 Evaporation of water from 3D printed structure	34
3.3.1 3D-printed porous structures	34

3.3.2 Wettability of 3D-printed material.....	35
3.3.3 Evaporation of water from 3D printed porous structure	36
Chapter 4 - Evaporation from single pores	38
4.1 Experiment 1- Evaporation from single pore: Effects of Relative Humidity	38
4.1.1 Evaporation time	38
4.1.2 Formation of liquid islands	41
4.2 Experiment 2 – Effects of wettability, liquid island, and breakup on evaporation from simulated soil pores	45
4.2.1 Evaporation time and projected area.....	45
4.2.2 Liquid island formation and change in radius of curvature	48
4.2.3 Volume and contact angles of liquid island.....	50
4.2.4 Capillary force and rupture of liquid islands	54
4.3 Experiment 3 – Contact line pinning and depinning prior to rupture of an evaporating droplet.....	57
4.3.1 Evaporation time	58
4.3.2 Contact line pinning and depinning	59
4.3.3 Change in projected areas	62
4.3.4 Change in radius of curvature of the liquid-vapor interface	63
4.4 Uncertainty analysis.....	67
Chapter 5 - Evaporation from porous columns.....	69
5.1 Liquid transport during evaporation from small hydrophilic soil columns	69
5.1.1 Evaporation time	69
5.1.2 Transient mass measurement and evaporation stages.....	70
5.1.3 Drying front imaging captured with 2D x-rays.....	73
5.2 Evaporative drying from hydrophilic and hydrophobic porous columns: consequences of wettability, porous structure, and hydraulic connectivity	76
5.2.1 Evaporation Phenomena	76
5.2.2 Propagation of drying front.....	80
5.2.3 Rayleigh-Nusselt correlation and calculation (fully saturated state)	86
5.2.4 Calculation of Bond number and Capillary number	88
5.2.5 Permeability modeling.....	90

5.2.6 Physical measurement of permeability	92
Chapter 6 - Droplet penetration and water evaporation from 3D-printed porous structures	95
6.1 Evaporation of deionized water from 3D-printed porous structure	95
6.1.1 Evaporative mass loss	95
6.1.2 Transient saturation and drying front propagation.....	98
6.1.3 Modeling evaporation rates.....	101
Chapter 7 - Conclusions and future works.....	110
7.1 Conclusions.....	110
7.2 Future works	114

List of Figures

Figure 2.1: Estimation of contact angles in (a) Young’s model where three-phase interfacial tensions create equilibrium and (b) Wenzel’s model where the droplet penetrates the cavities in a rough surface (c) Cassie-Baxter model where air is entrapped in the pores and creating a resistance to droplet penetration.....	6
Figure 2.2: Contact angle in (a) super-hydrophobic, (b) hydrophobic, (c) hydrophilic and (d) super-hydrophilic material	7
Figure 2.3: Evaporation stages from porous media i.e., constant rate, falling rate and slower rate period	16
Figure 3.1: Experimental apparatus of evaporation from single pore (a) schematic of the test section in an environmental chamber (b) 3D printed structure to hold the spheres in desired location (c) and (d) top view and side view of the droplet in a single pore [Evaporation from single pore (experiment: 1,2,3)].....	25
Figure 3.2: Spheres’ orientation for (a) experiment 1 (center-to-center distance 3.15 mm), (b) experiment 2 (equilateral combination, center-to-center distance $a = 3.1$ mm), (c) experiment 2 (isosceles combination, $b=2.8$ mm, $c= 2.7$ mm), and (d) experiment 3 (center-to-center distance 3.1 mm).....	26
Figure 3.3: SEM (Scanning Electron Microscope) images of glass (a and b) and Teflon (c and d) spheres [151].....	27
Figure 3.4: Schematic of evaporation from small hydrophilic porous column in a controlled atmosphere with $T = 22.2^{\circ}\text{C}$ and $\text{RH} = 35\%$	29
Figure 3.5: Average temperature (22.2°C) and relative humidity ($60\pm 1\%$) of the experimental atmosphere [151]	31
Figure 3.6: Experimental apparatus of the test section in a controlled atmosphere where $T = 22.2^{\circ}\text{C}$ and $\text{RH} = 60\%$ [151].....	32
Figure 3.7: Front view, side view and top view of (a) 3D structure 1, (b) 3D structure 2 and (c) 3D structure 3	35
Figure 3.8: Contact angle (36.92°) on flat ABS translucent surface	36
Figure 3.9: Schematic of evaporation of water from 3D printed porous structure	37

Figure 4.1: Evaporation of 4- μ L water droplet from glass (a-e) and Teflon (f-j) pores at 45% RH; (a) and (f) correspond to $t = 0$ min, (b-e) and (g-j) are droplets at 14, 15, 21, 24 and 20, 21, 27 and 30 minutes, respectively, for glass and Teflon pores [31] 40

Figure 4.2: Evaporation of 4 μ L water droplet from glass (a-e) and Teflon (f-j) pore at 60% RH. (a) and (f) the initial position at $t = 0$ min, (b-e) and (g-j) are droplet state at 17, 18, 27, 30 and 26, 28, 36 and 42 minutes respectively for glass and Teflon [31] 41

Figure 4.3: Liquid island formed between two particles (a) for a non-isothermal situation, due to temperature gradient one side of the liquid island is experiencing evaporation and the other side is experiencing condensation (b) for an isothermal situation, both sides of the liquid island are experiencing evaporation..... 42

Figure 4.4: Change of radius of curvature of the liquid island at 45% RH for glass (a-d) and Teflon (e-h). The radius was measured on both sides (radius 1 and 2) and plotted on the same graph to demonstrate the gradual decrease of radius due to evaporation on both sides [31]..... 43

Figure 4.5: Change of radius of curvature of the liquid island at 60% RH for glass (a-d) and Teflon (e-h). The radius was measured on both sides (radius 1 and 2) and plotted on the same graph to demonstrate the gradual decrease of radius due to evaporation on both sides [31]..... 44

Figure 4.6: Projected areas of whole droplet during evaporation. The plot represents the change in projected area during evaporation and figures a_1, b_1, c_1, d_1 are the initial and a_2, b_2, c_2, d_2 are the final projected areas in glass and Teflon for symmetric (i.e., equilateral) and asymmetric (i.e., isosceles) combination respectively [59] 47

Figure 4.7: Projected areas of liquid island during evaporation. The plot represents the change in projected area during evaporation and figures a_1, b_1, c_1, d_1 are the initial and a_2, b_2, c_2, d_2 are the final projected areas just before rupture in glass and Teflon for symmetric (i.e., equilateral) and asymmetric (i.e., isosceles) combination respectively [59] 48

Figure 4.8: Change in radius of curvature of liquid island with time. Glass spheres at (a_1) $t = 18$ min and (a_2) $t = 30$ min and in Teflon (b_1) $t = 28$ min and (b_2) $t = 43$ min (equilateral/symmetric combination). Glass spheres at (c_1) $t = 34$ min and (c_2) $t = 42$ min and Teflon spheres at (d_1) $t = 42$ min and (d_2) $t = 52$ min (isosceles/ asymmetric combination) [59] ... 50

Figure 4.9: Formation of liquid island between two spheres [59] 52

Figure 4.10: Change of volume of liquid island with time from beginning until rupture [59]..... 53

Figure 4.11: Variation of contact angle of liquid island with reduction of volume [59]..... 53

Figure 4.12: Variation of rupture strength of liquid island formed between glass or Teflon spheres for both combinations with time. Willet et al., [110] , Rabinovich et al., [106] and Lambert et al., [116]models were used to calculate the rupture strength [59]..... 57

Figure 4.13: Liquid island formation in two spheres. (a-d) and (e-h) represent liquid island formation and propagation from glass and Teflon respectively at 75% RH. (a) and (e) represent the final state of whole droplet just before rupture [30]..... 59

Figure 4.14: Contact line pinning and depinning of glass and Teflon at 30% RH. The plots represent the change in contact length in glass and Teflon for three spheres. a, b, c and d, e, f represent the contact line pinning and depinning in glass and Teflon pores respectively. P, D1, D2 and D2 represent pinned, depinned 1, depinned 2 and depinned 3 contact lines [30] 61

Figure 4.15: Contact line pinning and depinning of glass and Teflon at 75% RH. The plots represent the change in contact length in glass and Teflon for three spheres. a, b, c and d, e, f represent the contact line pinning and depinning in glass and Teflon pores respectively. P, D1, D2 and D2 represent pinned, depinned 1, depinned 2 and depinned 3 contact lines [30] 62

Figure 4.16: Change in projected area for glass and Teflon during evaporation at 30% and 75% RH. (a) and (c) represent the initial projected areas in glass at 30% and 75% RH. (b) and (d) represent the initial projected areas in Teflon at 30% and 75% RH respectively [30]..... 63

Figure 4.17: Change of curvature in liquid-vapor interface at 30% RH. (a), (b), (c) and (d), (e), (f) represent the curvature change (arrow sign) in glass and Teflon pores respectively. The black elliptical marks on the plot represent the transformation of liquid-vapor interface from arc to parabolic shape [30]..... 66

Figure 4.18: Change of curvature in liquid-vapor interface at 75% RH. (a), (b), (c) and (d), (e), (f) represent the curvature change (arrow sign) in glass and Teflon pores respectively. The black elliptical marks on the plot represent the transformation of liquid-vapor interface from arc to parabolic shape [30]..... 67

Figure 5.1: Transient mass decrease due to evaporation from hydrophilic soil column. The evaporative mass loss trend for three replications is similar [158]..... 71

Figure 5.2: Average evaporation time or dm/dt for all three replications. The dm/dt has been calculated at 30 minutes' averaged value [158]..... 72

Figure 5.3: Evaporation rate at mm/min for all three replications. The evaporation stages were divided into falling rate period, transition, and slower rate period [158] 73

Figure 5.4: Drying front propagation during evaporation from beginning until the end. The light blue color represents presence and deep blue color represents absence of water [158] 75

Figure 5.5: Mass loss and cumulative mass loss of water from (a) glass and (b) Teflon columns vs. time. The cumulative mass of glass (i.e., 3 g) is greater than Teflon sample (i.e., 2.4 g) after seven days of experiment [151]..... 77

Figure 5.6: Evaporation rate and dm/dt vs time for glass [(a) and (c)] and Teflon [(b) and (d)] columns. Evaporation rates are categorized as falling rate period and slower rate period based on the evaporative mass loss. Transient time has been divided by total time, $t_L = 168$ hours and presented as non-dimensional time, t^* [(c) and (d)] [151]..... 79

Figure 5.7: Saturation vs. time and evaporation rate vs. transient saturation for glass (a and c) and Teflon (b and d) sample. Approximately, 40% and 30% of total evaporation occurred before slower rate period in glass and Teflon column respectively [151] 81

Figure 5.8: (a) Drying front depth vs. time and (b) fractional mass loss calculated from scale and x-ray (log transformed) for glass sample. The bottom pictures (c) show the X-ray imaging of drying front propagation where red and deep blue represents presence (100% water saturation) and absence (0% water saturation) of water respectively. Drying front propagated from ~19 mm to ~34 mm from 3rd day until 7th day. The color bar represents the range of saturation [0-1] and significant partial saturation is observed near the drying front [151]..... 83

Figure 5.9: (a) Drying front depth vs. time and (b) fractional mass loss calculated from scale and x-ray (log-transformed) for Teflon sample. The bottom pictures (c) show the X-ray imaging of drying front propagation where red and deep blue represents presence (100% water saturation) and absence (0% water saturation) of water respectively. The color bar represents the range of saturation [0-1] and some partial saturation is observed near the drying front [151]..... 84

Figure 5.10: Diffusive flux and evaporation rate for glass and Teflon. Diffusive flux matched well with the evaporation rate when it entered into slower rate period for both glass (after 90 hours) and Teflon (after 70 hours) sample [151]	86
Figure 5.11: Physical measurement of hydraulic conductivity of the porous system using constant head method [151]	94
Figure 6.1: Evaporative mass loss of water from three 3D-printed structures	97
Figure 6.2: Transient saturation vs. time for 3D structure-1, 3D structure-2 and 3D structure-3	98
Figure 6.3: Drying front depth during evaporation from 3D structure-1.....	100
Figure 6.4: Drying front depth during evaporation from 3D structure-2.....	100
Figure 6.5: Drying front depth during evaporation from 3D structure-3.....	101
Figure 6.6: Steady-state heat transfer in a single layer of the porous structure	102
Figure 6.7: Layer by layer thermal gradient while evaporation of water from 3D-printed structure-1	106
Figure 6.8: Evaporation rate (dm/dt) in g/min for 3D structure-1	108
Figure 6.9: Evaporation rate (dm/dt) in g/min for 3D structure-2	109
Figure 6.10: Evaporation rate (dm/dt) in g/min for 3D structure-3	109

List of Tables

Table 2.1: Comparison of initial contact angles in flat glass (hydrophilic) and Teflon (hydrophobic).....	7
Table 2.2: Particle size and porosity in previous studies of evaporation from packed beds	18
Table 3.1: Experimental parameters for evaporation of sessile droplet from a single pore	24
Table 3.2: Dimensions of three 3D printed porous structures	35
Table 4.1: Evaporation time for 4 μ L water droplet at 45% and 60% RH from hydrophilic (glass) and hydrophobic (Teflon) pores.....	39
Table 4.2: Evaporation time for 4- μ L water droplet from hydrophilic and hydrophobic pores for both equilateral and isosceles combination at 60% RH.....	46
Table 4.3: Average time to form liquid islands in glass and Teflon pores for both combination	49
Table 4.4: Evaporation time for 4 μ L water droplet at 30% and 75% RH from hydrophilic (glass) and hydrophobic (Teflon) pores.....	58
Table 4.5: Measuring radii of curvature at 45% RH for glass and Teflon in experiment 1	67
Table 4.6: Standard deviation in measuring contact angle and principal radius of curvature for glass at equilateral combination in experiment 2.....	68
Table 4.7: Standard deviation in measuring the solid-liquid-vapor contact lengths (pinned, depinned 1 and depinned 2) and projected areas for glass at 30% RH.....	68
Table 5.1: Time to evaporate 5 mL of water from a simulated hydrophilic soil column	70
Table 5.2: Rate of evaporation at slower rate period in previous studies	79
Table 5.3: Rayleigh-Nusselt number calculation for natural evaporation at fully saturated state and comparison with previous studies	88
Table 5.4: Bond and Capillary number calculation for different studies.....	89
Table 5.5: Calculation of permeability of previous and this study	91
Table 5.6: Predicted and measured values of permeability for the porous sample.....	93
Table 6.1: Mass properties of 3D-printed porous structures.....	96
Table 6.2: Porosity calculation of 3D printed porous structure	96
Table 6.3: Common parameters to model the steady-state evaporation rate	104
Table 6.4: Temperature and heat flux in different layers of the 3D-printed structures	106

Acknowledgements

At first, I would like to thank Dr. Melanie Derby from the core of my heart for being my major professor and my supervisor. With her profound guidance, I was able to overcome the hard journey of being a graduate student. She is very professional, kind, generous and a good-hearted person and without her continuous support I would not be able to survive in some difficult period of times. I would like to thank my committee members: Dr. Betz, Dr. Bindra, Dr. Kluitenberg and Dr. Kirk for their valuable feedbacks and suggestions in different stages of my Ph.D. research. I am deeply thankful to Dr. Bindra and Molly Ross for their continued support in conducting my experiments in their lab and being co-authors in two of my publications. I would also like to show my humble gratitude to Dr. Eckels for providing me the opportunity to conduct experiments in one of the chambers of IER. In addition, I want to thank all my lab-mates and colleagues who made it easier for me when I was struggling with any difficulties. I want to acknowledge the support from National Science Foundation grants #1651451 and #1828571.

I cannot thank enough my family members for their continued support and sacrifice that made me what I am today. I am grateful to my father Prasanta Chakraborty, my mother Kumkum Chakraborty, my uncle Dr. Sanjoy Chakraborty, my aunt Lipika Chakraborty, my in laws Kanu Chowdhury and Ronita Chowdhury, my grandmothers Monjushri Chakraborty and Bani Chakraborty for all their sacrifices all over the years. I wish my grandfathers Chintaharan Chakraborty and Priyo Ranjan Chakraborty were here to see me completing my Ph.D. journey. I convey lots of love to my siblings: Debjani, Debarati, little Rishi and Orthi who mean a lot in my life. Last but not the least, I am deeply indebted to Sulogna, my wife. Without her continuous support, assistance, and love, I would not be able to chase my dreams. Thank you for being in my life in my most difficult times and with you I want to achieve more things in life.

Dedication

I would like to dedicate my dissertation to “Ma Mahamaya” for all the blessings, perseverance, and guidance She bestowed on me. With Her blessings, I overcame the most difficult periods of my life.

Preface

Some of the work presented in this dissertation was presented in the following conference and journal papers, and was used with permission:

1. Chakraborty, P. P., Huber, R., Chen, X., & Derby, M. M. (2018). Evaporation from simulated soil pores: Effects of wettability, liquid islands, and breakup. *Interfacial Phenomena and Heat Transfer*, 6(4).
2. Chakraborty, P. P., & Derby, M. M. (2018, June). Evaporation from a simulated soil pore: Effects of relative humidity. In *International Conference on Nanochannels, Microchannels, and Minichannels* (Vol. 51197, p. V001T05A001). American Society of Mechanical Engineers.
3. Chakraborty, P. P., & Derby, M. M. (2020, July). Contact Line Pinning and Depinning Prior to Rupture of an Evaporating Droplet in a Simulated Soil Pore. In *International Conference on Nanochannels, Microchannels, and Minichannels* (Vol. 83693, p. V001T06A003). American Society of Mechanical Engineers.
4. Chakraborty, P. P., Ross, M., Bindra, H., & Derby, M. M. (2022). Evaporative Drying from Hydrophilic or Hydrophobic Homogeneous Porous Columns: Consequences of Wettability, Porous Structure and Hydraulic Connectivity. *Transport in Porous Media*, 1-28.
5. Chakraborty, P. P., Ross, M., Bindra, H., & Derby, M. M. (2019, July). Liquid Transport During Evaporation of Water From a Small Simulated Soil Column. In *Heat Transfer Summer Conference* (Vol. 59315, p. V001T10A015). American Society of Mechanical Engineers.

6. Derby, M. M., Adams, A. N., Chakraborty, P. P., Haque, M. R., Huber, R. A., Morrow, J. A., ... & Bindra, H. (2020). Heat and Mass Transfer in the Food, Energy, and Water Nexus—A Review. *Journal of Heat Transfer*, 142(9).

Chapter 1 - Introduction

The resources in food-energy-water nexus are limited and interconnected. The current global challenge is to make sustainable uses of the water to produce more food and energy for a growing population – projected to reach 9.8 billion in 2050 [2]. Despite a growing global population, the amount of global arable land is predicted to be nearly constant (i.e., 1661×10^9 ha in 2050 [3]) with predicted increase in food production by 50% within 2030 [4]. Currently, agriculture is a significant water user and is responsible for 2/3 of the global water withdrawals [5]. Arid or semi-arid areas are facing increasing pressure for water resources, yet irrigation is critical for increasing yields; 20% of global land is irrigated, but it accounts for 40% of crop production [1]. Surface-level water resources, such as rivers, ponds, reservoirs can serve as irrigation sources, but they are prone to drought [6]. In arid or semi-arid areas of the Great Plains in U.S, where rainfalls are limited, the Ogallala Aquifer is the primary source of irrigation water for food production, and the Ogallala is responsible for 20% of total production of corn, wheat, sorghum, and cattle in U.S. In southwestern Kansas, there are 1.5 million irrigated acres and the Ogallala provides 90% of the water for irrigation [7] and, due to increased water withdrawals, the Ogallala aquifer in the U.S Central High Plains declined [8-10], highlighting the need for sustainable water usage in the food-energy-water nexus.

One approach to conserve soil moisture is to restrict evaporation, thereby reducing irrigation demands and overall water consumption for crop production. Altering the wettability of the soil (i.e., inclusion of hydrophobicity in the soil) is a potential approach to restricting evaporation. Any material can be classified into two categories of wettability: hydrophilic (i.e., water loving) and hydrophobic (i.e., water repelling). The wettability of a material depends on the contact angle (i.e., the angle created by the liquid with solid where the liquid-vapor interface meets

the solid surface). For hydrophilic materials, the contact angle is less than 90° and in hydrophobic materials, the contact angle is greater than 90° . Previous researchers utilized hydrophobicity to reduce water evaporation from soil in laboratory environments [11-18]. Bachmann et al. [19], Davis et al., [20] and Shokri et al. [16] demonstrated that evaporation from hydrophobic soil can be 50–65% lower than that of hydrophilic soils.

Altering the wettability of a porous media impacts evaporation by altering the contact angle dynamics and formation of liquid islands (i.e., thin liquid films formed between two/ three particles of the porous media) [21-23]. The structure of the porous media impacts evaporation, including the texture (e.g. fine or coarse) [24] permeability [25], hydraulic conductivity [26, 27] and hydraulic connection of the liquid in the porous structures [28, 29]. Climate conditions, such as temperature, pressure, relative humidity also impact evaporation [30, 31]. In this dissertation, the impacts of wettability on evaporation of water were investigated from single pores and porous media.

Chapter 2 - Literature Review

Evaporation is a phase-change phenomena where liquid transforms into vapor at the liquid-vapor interface when the vapor pressure is less than the saturation pressure of the liquid [32, 33]. Based on the application, liquid can be dried or evaporated from a flat surface [34-41] or porous media. From a flat surface, sessile liquid droplets are evaporated to understand the influence of contact angle dynamics on wetting phenomena [36] and the knowledge can be applied in micro/nano fabrication [42, 43], ink-jet printing [44], spray mechanism [45, 46], DNA/RNA stretching and deposition [37, 47, 48] etc. On the other hand, evaporative drying from single/ multi-porous media is important for cooling at the micro [49] and macro scale [50, 51], heat pipes [52, 53], food drying [54], fuel cells [55, 56] and soil-water dynamics [11, 12, 14, 16, 29]. Several factors such as wettability (i.e., hydrophilic, or hydrophobic) [16, 57], contact angle dynamics [58], formation of liquid island [21, 22], atmospheric conditions (i.e., relative humidity, pressure, temperature, wind flow) [31, 59], porous structure (i.e., homogeneity [60] or heterogeneity [12]), pore size distribution [15] etc. play a vital role in natural evaporative drying and by varying these parameters faster or slower evaporation rate can be achieved based on the implication. Porous structure and pore size distribution lead to other intrinsic properties of the porous media such as capillary action [29], permeability [25, 27], and hydraulic conductivity which also contribute vitally in the evaporation phenomena.

The inclusion of hydrophobicity in soils affects evaporation, but also impacts infiltration and runoff. Inclusion of hydrophobicity on top soil layer can decrease evaporation rates by 50-65% [12, 16, 17]. Shokri et al. [14, 16] experimented on evaporation from heterogeneous sand columns. Four different columns with hydrophobic and hydrophilic sands were prepared: (a) completely hydrophilic sand, (b) top 7 mm of hydrophobic sand on top of hydrophilic sand (c), 25

mm of hydrophobic sand on top of hydrophilic sand, and (d) 7 mm hydrophobic sand layer placed 18 mm below hydrophilic sand. Column 'c' and 'd' experienced the lowest cumulative mass loss due to the hydrophobic layer on top and in 18 mm below of hydrophilic sand.

Although hydrophobicity offers advantages for reducing evaporation, the inclusion of hydrophobicity on the top soil layer (e.g., induced by forest fires) can have adverse effects. Though the addition of hydrophobicity can restrict evaporative loss, further infiltration is also restricted due to creation of a water-repellent front that decreases soil permeability [61]; for example, a 40% decrease in hydraulic conductivity has been reported in forest-fire induced hydrophobic soil [62]. To improve infiltration in hydrophobized soils, water amendments with inclusion of microbial based solution have been studied. Surfactin, which is a secondary metabolite produced from the bacteria *Bacillus Subtilis* [63], is a bio-surfactant that can reduce water surface tension (e.g., from 72 to 27 mN/m) leading to improve soil wettability (i.e., increase hydrophilic properties) [64], infiltration [65] and soil-water capacity [66]. In semi-arid regions, surfactant producing microbes play an important role in altering soil hydrological properties which enhances soil infiltration [67]. In addition, microbes in soil can enhance nutrient availability to plants by eliminating plant pollutants [66] resulting in improving plant health [68]; however, the impacts on hydrophobicity and altered water dynamics in soil has not been well quantified.

2.1 Evaporative drying from flat surface

2.1.1 Estimation of contact angle in different wettable material

Based on the interaction with water, any material can be characterized as hydrophilic (i.e., water-attracting) or hydrophobic (i.e., water-repelling) material [69]. The degree of hydrophilic or hydrophobic material can be estimated by measuring the contact angle of a liquid droplet placed

on a flat surface. The contact angle of a liquid droplet on a flat surface is defined as the angle created by the liquid with solid where the liquid-vapor interface meets the solid surface [70, 71]. For a typical hydrophilic surface, due to its affinity towards water, a sessile water droplet becomes stretched (high surface energy), resulting in a contact angle less than 90°. On the other hand, due to water repelling property (low surface energy), the contact angle in hydrophobic material is greater than 90°. When a droplet is placed on a flat surface, the droplet creates three-phase contact lines (i.e., solid-liquid-vapor), which move to balance the forces originating from the three interfacial tensions to reach an equilibrium position [72]. The relation between contact angle and three-phase contact line can be expressed as a form of Young's equation:

$$\cos\theta_{CA} = \frac{\gamma_{sv} - \gamma_{sl}}{\gamma_{lv}} \quad (2.1)$$

where, θ_{CA} is contact angle, γ_{sv} , γ_{sl} and γ_{lv} are solid-vapor, solid-liquid, and liquid-vapor interfacial tensions respectively. Young's equation assumes the solid surface to be smooth, flat, chemically homogeneous, non-porous and non-deformable. In a rough surface, where liquid droplet keeps contact with the solid and it completely penetrates the cavities, the previous equation to determine contact angle was modified by Wenzel [73]:

$$\cos\theta_{w(CA)} = r_s \cos\theta_{(CA)} \quad (2.2)$$

where, $\cos\theta_{w(CA)}$ is contact angle for Wenzel model and r_s is average roughness ratio. In a porous system, where the pores are initially entrapped by air and the air creates a resistance to the penetration of the water into the pore leading to a water repellent situation. To deal with the trapped air, Cassie and Baxter [74] modified the previous equation in following way:

$$\cos\theta_{c(CA)} = f_1 \cos\theta_1 + f_2 \cos\theta_2 \quad (2.3)$$

where, $\cos\theta_{c(CA)}$ is the Cassie contact angle, f_1 is the fractional area of the surface with contact angle θ_1 and f_2 is the fractional area of the surface with contact angle θ_2 . If one of the phases is air, the previous equation simplifies into the following one as the contact angle of air and water is 180° . Figure 2.1 demonstrates the Young's model, Wenzel's model and Cassie-Baxter model of estimation of contact angle of sessile water droplet.

$$\cos\theta_{c(CA)} = f_1\cos\theta_1 - f_2 \quad (2.4)$$

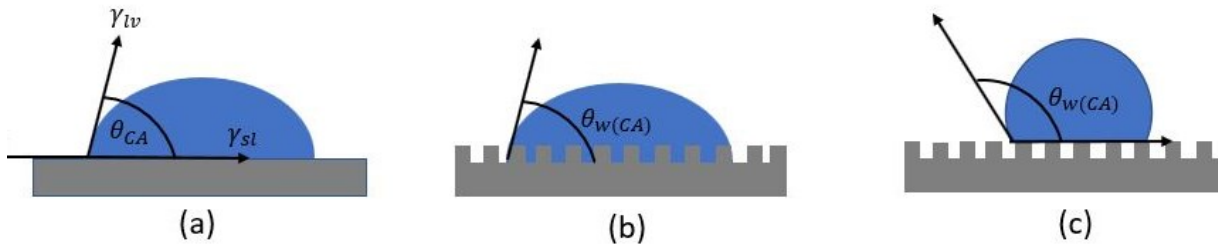


Figure 2.1: Estimation of contact angles in (a) Young's model where three-phase interfacial tensions create equilibrium and (b) Wenzel's model where the droplet penetrates the cavities in a rough surface (c) Cassie-Baxter model where air is entrapped in the pores and creating a resistance to droplet penetration.

Hydrophilic, and hydrophobic materials, super-hydrophilic and super-hydrophobic materials have been characterized in previous studies [57, 69, 75]. In super-hydrophilic material associated with super-wetting phenomena, the contact angle was found 0° - 5° due to rapid spread of the droplet [76, 77] and on the other hand, in super-hydrophobic surface, the initial contact angle was found greater than 150° [57, 77, 78]. Figure 2.2 represents contact angle of super-hydrophobic,

hydrophobic, hydrophilic, and super-hydrophilic materials.

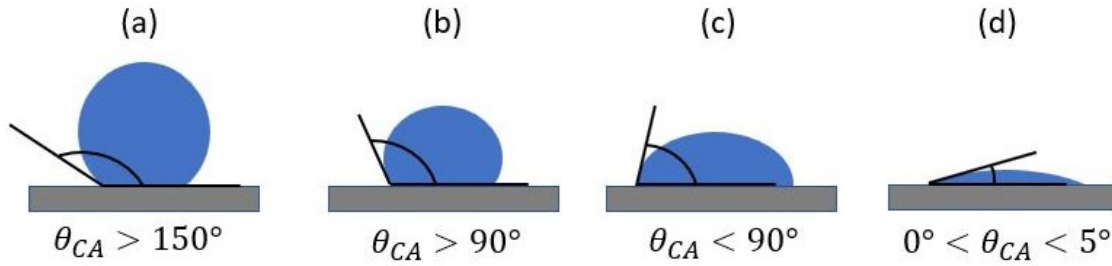


Figure 2.2: Contact angle in (a) super-hydrophobic, (b) hydrophobic, (c) hydrophilic and (d) super-hydrophilic material

In previous studies, different materials and methods have been used to understand contact angle dynamics while droplet evaporation. In most of the studies, to compare between hydrophilic and hydrophobic materials, flat glass and Teflon [34, 39, 57, 79-81] surfaces have been used and different technology such as: High-speed camera [79, 81], goniometer [38] and Optical microscopes [57] have been used to measure the contact angle. In a study with flat glass surface [34], the initial contact angle was found $\sim 41^\circ$ and it was independent of the droplet volume (5, 10, 15 μL), though in other studies with flat glass surface, the contact angle varied from 30° [39] to 58° [57] with droplet volumes of 3 μL and 5 μL . For Teflon, in all cases, the contact angle was found to be 100° - 114° and different droplet volumes (1, 2, 3, 6 3 μL) were studied [38, 39, 79, 82]. Table 2.1 represents the comparative study of initial contact angle for flat glass (hydrophilic) and Teflon (hydrophobic) surfaces presented in previous literature.

Table 2.1: Comparison of initial contact angles in flat glass (hydrophilic) and Teflon (hydrophobic)

Reference	Material	Type of material	Volume of water droplet (μL)	Initial contact angle ($^\circ$)
Birdi and Vu [34]	Glass	Hydrophilic	5, 10, 15	41
Fang et al. [79]	Teflon	Hydrophobic	2	100

Fang et al. [80]	Teflon	Hydrophobic	1-2.1	100
Liu et al. [81]	Glass	Hydrophilic	6	40
	Teflon	Hydrophobic	6	110
Orejon et al. [39]	Glass	Hydrophilic	3	30
	Teflon	Hydrophobic	3	114
Shin et al. [57]	Glass	Hydrophilic	5	58
Nguyen et al. [38]	Teflon	Hydrophobic	2	110

Besides glass and Teflon, other materials such as smooth gold ($\sim 80^\circ$) [79], copper ($\sim 60^\circ$ - 70°) [81], silicon (57° - 60° , 78°) [38, 39, 83], Polymethylmethacrylate (67°), Poly-alpha-methyl styrene (87°) [82] etc. have been used for comparative study of contact angle dynamics. Inclusion of hydrophobic coating can introduce hydrophobicity in a hydrophilic material. In some recent studies, deep coating of Teflon on copper [84-86] and aluminum [87] increased the contact angle from 70° to 110° and 49° to 120° respectively. Contact angle dynamics and change in droplet geometry during evaporation contribute to surface pinning and depinning which is discussed in next section.

2.1.2 Contact line dynamics: Pinning and depinning of hydrophilic and hydrophobic material

When a droplet is deposited on a substrate, based on the nature of the material (i.e., roughness, surface energy) and other environmental parameters (i.e., wind flow, pressure, temperature, RH etc.), the droplet can experience partial or complete wetting. Complete wetting exhibits full spreading of water on substrate leading to equilibrium contact angle of approximately 0° [69, 76]. In partial wetting, the contact angle becomes measurable and based on the static contact angle measurement, hydrophilic ($< 90^\circ$) or hydrophobic ($> 90^\circ$) material can be characterized.

During evaporation of a droplet deposited on a flat surface, the droplet deforms due to evaporative mass loss and three distinct stages of droplet contact line dynamics are noticed: CCR (constant contact radius) – where solid-liquid contact line does not decrease (i.e., pinned) but contact angle decreases [35, 39, 57, 88, 89], CCA (constant contact angle) – where contact angle remains almost constant throughout the evaporation process but contact line decreases (i.e., depinned) [38, 39, 57, 82, 90-92], and mixed mode – where the droplet experiences reduction in both contact lines and contact radius after a transition point of evaporation [89, 90, 93]. In smooth flat surfaces, pinning phenomena was dominant in hydrophilic materials [35, 39, 94, 95] than hydrophobic one in previous studies and the contact angle decreased until depinning occurred. Orejon et al. [39] studied 3- μL droplet evaporation from flat glass (hydrophilic) and Teflon (hydrophobic) surfaces and found constant contact radius (~ 2 mm) in glass and gradual decrease (0.8 mm to 0.1 mm) in Teflon during evaporation. The contact angle was found continually decreasing (28° to 0°) in glass and in Teflon, the contact angle remained almost constant (120°) throughout the evaporation. In a study with Teflon-coated silicon (initial contact angle = 120°) [92], the contact radius of the droplet decreased gradually with time while contact angle decreased slowly (from 120° to $\sim 100^\circ$) until 40% of the total evaporation time and then it experienced constant contact angle (CCA) mode till 90% of total evaporation. Similar trend was found in another study with Teflon coated silicon, while the contact angle decreased slowly till 30% of the evaporation time and then it remained constant until the end of evaporation [38]. Gatapova et al. [91] experimented with larger volume of droplet (80-400 μL) evaporation from anodized aluminum (hydrophilic) and Teflon (hydrophobic) surface and found pinning (90% of the time) of contact radius and linear decrease in contact angle in hydrophilic surface and exact opposite scenario was observed in hydrophobic surface (i.e., depinned). Shin et al., [57] experimented with hydrophilic, hydrophobic and

superhydrophobic surfaces where droplet pinning was observed for 75% and 40% of the time in hydrophilic and hydrophobic surface respectively and the superhydrophobic surface experienced no pinning i.e., depinning phenomenon.

2.1.3 Modeling of evaporation of sessile droplet from flat surface

Sessile droplet evaporation from flat surface have been modeled and experimented in previous studies and key parameters such as contact angle, contact radius, droplet height, contact area etc. have been identified as contributing factors leading towards faster or slower evaporation rate. Birdi and Vu [34] experimented with sessile water droplet from flat glass surface and the evaporation rate was estimated both theoretically and experimentally and droplet evaporation rate was expressed as:

$$-\frac{dm}{dt} = -\rho_L \frac{dV}{dt} \quad (2.5)$$

where, m is mass, V is volume and ρ_L is liquid density. For millimeter size droplet with axial symmetry, this equation was modified by Fuchs [96] to :

$$-\frac{dm}{dt} = -4\pi R^2 D \frac{dc}{dR} \quad (2.6)$$

where, R is the radial distance from the center of the droplet, D is diffusion coefficient and c is the vapor concentration. When a droplet evaporates in air, the gaseous phase becomes mixed with vapor and air concentration [36] and applying proper boundary condition ($c = c_s$ when $R = R_s$, and $c = c_\infty$ when $R = R_\infty$) the equation becomes:

$$-\frac{dm}{dt} = 4\pi R_s D (c_s - c_\infty) \quad (2.7)$$

where, R_s radius of the spherical droplet from center to surface, c_s is vapor concentration at the sphere surface and c_∞ is ambient vapor concentration. Assuming ambient vapor concentration to be approximately zero at infinite distance the equation becomes:

$$-\frac{dm}{dt} = -\rho_L \frac{dV}{dt} = 4\pi R_s D c_s. \quad (2.8)$$

If the vapor pressure of the liquid is not very small due to presence of vapor molecule in the medium the previous equation can be modified [97, 98] and expressed as follows:

$$-\frac{dm}{dt} = \frac{4\pi MDP_T}{\mathfrak{R}T} \ln\left(\frac{1}{1 - \frac{P_s^v}{P_T}}\right) R_s \quad (2.9)$$

where, M is molecular weight, P_s^v is vapor pressure of the evaporating liquid, P_T is total atmospheric pressure, \mathfrak{R} is ideal gas constant, T is temperature and the previous equation can be modified in following way to express relationship between evaporation rate and relative humidity (RH):

$$-\frac{dm}{dt} = 4\pi R_s D \left(\frac{MP_0^{vs}}{\mathfrak{R}T}\right) (1 - RH) \quad (2.10)$$

where, $RH = \frac{P_0^v}{P_0^{vs}}$, P_0^v is actual vapor pressure of the medium and $P_s^v = P_0^{vs}$ is vapor pressure of the evaporating liquid. This equation expresses that, the evaporation rate is proportional to the droplet contact radius, and it increases with decreasing relative humidity (RH). During droplet evaporation, droplet height along with droplet volume were found to be decreased for both hydrophilic and hydrophobic surfaces and the following modifications were made to relate droplet height and volume with contact angle dynamics [36, 79, 81, 82]:

$$h = r_b \tan\left(\frac{\theta}{2}\right) \quad (2.11)$$

$$V = \frac{\pi R_s^3 (2 - 3 \cos \theta + \cos^3 \theta)}{3 \sin^3 \theta} \quad (2.12)$$

Where, $r_b = R_s \sin \theta$, is contact radius, h is droplet height, V is droplet volume. The evaporation rate then was modified as follows [37, 97, 99]:

$$-\frac{dm}{dt} = 4\pi R_s D (1 - RH) c_s f(\alpha) g(T) \quad (2.13)$$

Where, $f(\alpha)$ is dependence on contact angle and $g(T)$ is dependence on ambient and interfacial temperature.

In the study of Birdi and Vu [34], the evaporation rate of sessile water droplet from flat glass surface increased from 0.0001175 g/min to 0.0002028 g/min with increase in droplet volume from 5 μL to 15 μL , leading to greater contact radius of the droplet as contact radius is directly proportional to the evaporation rate. Shin et al. [57] experimented droplet evaporation from three surfaces: glass (hydrophilic), octadecyltrichloro-silane (OTS) (hydrophobic) and alkylketene dimmer (AKD) (superhydrophobic) coatings where in hydrophilic and hydrophobic surface the droplet was pinned for 75% and 40% of the total time leading to a faster evaporation in glass than OTS. The superhydrophobic surface (AKD) did not experience any pinning (i.e., the solid-liquid contact line moved) leading to smaller contact line and subsequent slower evaporation. Liu et al. [81] evaporated 6- μL water droplets from flat glass and Teflon surfaces where glass experienced pinning phenomena with higher reduction rate in droplet volume i.e., higher evaporation rate than Teflon. In the work of Orejon et al., [39], glass surface experienced pinning phenomena for most of the time of total evaporation with higher contact radius (~ 2 mm) than Teflon (~ 0.9 mm) which led to faster evaporation in glass. Surface temperature also plays a vital role in droplet evaporation as it is directly proportional to the evaporation rate. In a study with increasing surface heat flux from 1000 W/m^2 to 7000 W/m^2 [100], the droplet evaporation rate increased sharply though for all heat fluxes, hydrophilic surface experienced higher evaporation rate than hydrophobic one due to greater pinning span.

2.2 Liquid islands formed in a single pore

During evaporation from a porous media (e.g., soil), formation of liquid islands between two or three particles is an important phenomenon as it indicates the termination of constant rate of evaporation and initiation of falling rate and subsequent slower rate of evaporation when the liquid islands rupture. Philip and De Vries [21, 22] postulated the theory of formation of liquid islands in a non-isothermal atmosphere where one side of the liquid island experiences increase in radius due to condensation and other side experiences decrease due to evaporation. The mechanism of liquid island formation and its consequences are discussed in section 4.1.2 (Figure 4.3). Due to its importance in evaporation from porous media, different parameters of liquid islands such as rupture energy/ force to break up the liquid island [101-110], Volume, surface area and contact angle [104, 111-114] estimation were modeled and analyzed both experimentally and numerically [111, 115] for liquid islands formed between two or three spherical spheres. Bisschop and Rigole [101], Gladky and Schwarze [102], Rabinovich et al., [106], Wang et al., [108] and Willett et al., [110] estimated the required rupture energy of the liquid islands formed between two spheres as capillary bridge model (CBM). The models predicted the liquid island as capillary bridge formed between two spheres and the rupture energy required to snap off the island is deduced from the active capillary force of the liquid island. The rupture energy/ force is dependent on the volume, surface area, distance between the particles/ spheres, contact angle and half filling angle. The typical liquid island between two spheres is demonstrated in Figure 4.9. Bisschop and Rigole [101] mathematically deduced the capillary bridge model to estimate rupture energy of the liquid island, while Pitois et al., [105], Rabinovich et al., [106], Willett et al., [110] and Lambert et al., [116] estimated the rupture force/ energy both experimentally and analytically [equation (4.8), (4.10), (4.13)].

Farmer and Bird [111] estimated the contact angle, volume and surface area of asymmetric liquid islands formed between two contacting spheres and three different models were postulated for catenoidal, cylindrical and spherical liquid islands. Semprebon et al., [112] applied Young-Laplace equation to solve rupture force of the liquid island and used x-ray tomography to visualize deformation of liquid island formed between three spheres. Murase et al., [115] used Finite Element Method (FEM) to numerically evaluate liquid island rupture phenomenon and experimentally validated the data with analytical results.

The effect of movements of particles of the porous media on liquid island breakup were evaluated in some studies [104, 113, 117, 118]. Gras et al., [103] investigated the capillary action induced energy between in a liquid island formed between two spheres. They applied Young-Laplace equation to solve the critical rupture energy when the spheres were in relative motion with a suction control valve. Lievano et al., [104] estimated both the static and dynamic rupture force of a liquid island formed between two or three particles and the dynamics were controlled with a micro-mechanical suction device. The rupture was associated with the liquid island volume, contact angle and dynamic motion of the particle. Mielniczuk et al., [117] evaluated evaporation induced rupture in both static and dynamic condition (when the spheres have movement) of the liquid island and deduced that, rupture and evaporation occurred 25% more in the dynamic condition. Rossetti et al., [118] analytically modeled the energy stored in a liquid island formed between two spheres and experimentally measured the rupture force needed to break up the liquid island. Two micromotors were used to induce opposing velocity to the spheres and the rupture force was estimated using motor power and separation distance.

2.3 Evaporation from porous media

Multi-porous media typically is made with multiple particles, grains or meshes where porosity, porous structure and pore size distribution play a vital role in evaporative drying. A multi-porous media can be made with spherical particles, meshes, grains or soil sample (e.g., sand) to study evaporation dynamics during drying. In general, evaporation stages from porous media can be classified into three groups: constant-rate, falling-rate, and slower rate period [13, 29, 119]. In constant rate period, the porous media maintains a constant rate of evaporation for a certain time period until the top surface remains fully saturated, and a hydraulic connection is maintained between the unsaturated and saturated portion of the porous sample. The drying evaporative front propagates through the porous media and the maximum drying front at the end of constant rate is characterized as characteristic length which is defined as the maximum potential hydraulically connected region (hydraulic linkage between saturated and unsaturated part) between the top surface of evaporation and the saturated portion [11, 13, 14, 29]. When this hydraulic connection breaks down due to greater gravitational force than capillary force, the evaporation experiences a sharp decrease which is defined as the falling rate period of evaporation where the top surface remain partially saturated with formation of several liquid islands between particles [119]. The slower period of evaporation occurs when the water level drops down breaking most of the liquid islands and the evaporation is fully dominated by diffusion [12-14, 17]. Figure 2.3 represents different stages of evaporation in a porous media.

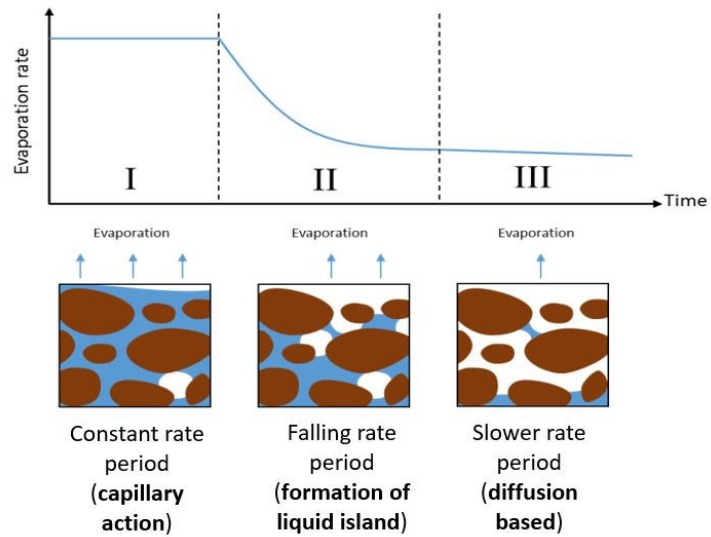


Figure 2.3: Evaporation stages from porous media i.e., constant rate, falling rate and slower rate period

2.3.1 Evaporation from porous packed beds made with spheres

Evaporative drying from porous media has been extensively analyzed both experimentally and theoretically and the porous media were made with packed spheres [120-131]. Borosilicate glass spheres of different sizes have been used mostly to understand and differentiate among evaporation stages [121-124], effects of pore size on evaporation [120, 128, 131] and formation of liquid island [120, 131]. In a study with more hydrophilic (contact angle = $16\pm 5^\circ$) and less hydrophilic ($82\pm 4^\circ$) packed beds made with glass spheres, greater mass loss was found in more hydrophilic porous media [120]. Due to hydraulic continuity in the more hydrophilic media, evaporative mass loss was greater and constant period of evaporation was significant than the less hydrophilic media and the hydraulic continuity was determined by numerical simulation. In a series of study of evaporation from hydrophilic porous media made with glass spheres of different sizes (0.1-3 mm of diameter) packed in a container with sample height ranging from 80-89 mm, the characteristic length found to be decreasing in porous sample made with larger particle (i.e., 122 mm for 0.1 mm particle size and 34 mm for 3 mm particle size) [121-123] which resulted in

extended period of constant evaporation rate in porous sample with smaller particle (0.1-0.85 mm) than sample with larger particles (2.5-3 mm). The characteristic length is expressed as follows:

$$L_c = \frac{2\gamma}{\rho_w g} \left(\frac{1}{r_1} - \frac{1}{r_2} \right) \quad (2.14)$$

where, L_c is characteristic length, γ is interfacial tension, ρ_w is density of water, g is acceleration due to gravity, r_1 and r_2 are smaller and larger pore radii of the porous media.

Due to heterogeneity (i.e., large range of pore size distribution) of the porous system, a distinctive constant rate, falling rate and slower rate period of evaporation was found in previous studies [120-123]. In another study of evaporation from porous sample made with combination of finer (i.e., 0.15 mm) and coarser (i.e., 0.4 mm) glass spheres, smaller spheres on the top of larger (i.e., 0.15 mm spheres' layer on top of 0.4 mm spheres) initiated capillary action and subsequent continuous hydraulic connection resulting in more evaporative mass loss at a constant rate than the other combination (i.e., 0.4 mm spheres' layer on top of 0.15 mm spheres) [128]. In a series of experiments with glass packed beds with spheres' sizes ranging from 0.1-0.85 mm, the evaporative mass loss was found greater (up to 5.52E-5 g/s) in fine layer (i.e., 0.1-0.15 mm) than the coarse (i.e., 0.8-0.85 mm) packed beds (up to 0.96E-5) [130]. The hydraulic linkage (determined by numerical simulations) between the saturated and unsaturated part contributing to the faster evaporation rate is influenced by formation of liquid island between spherical particles. Porous configuration directly contributes to the formation of liquid island and in three different combination of glass spheres (1 mm): straight, loose and closed packing, more liquid islands were formed in closed packing leading to a faster evaporation while the other two (straight and loose) experienced slower evaporation rate due to reduced ability of forming liquid islands [131]. Table 2.2 represents the porous configuration (i.e., materials, porous sample height, particle diameter and porosity) used in previous studies. Porosity is defined by the following equations:

$$\varphi = \frac{V_E}{V_T} \quad (2.15)$$

where, φ is porosity, V_E is empty volume and V_T is total volume of the porous media.

Table 2.2: Particle size and porosity in previous studies of evaporation from packed beds

Reference	Porous material	Porous sample Height (mm)	Particle diameter (mm)	Porosity, φ
Cejas et al. [120]	Glass spheres	135	0.5, 1	63%, 53%
Kumar et al. [121, 122]	Glass spheres	89	0.1-0.16, 2.5-3	33.2%, 34.31%
Kumar et al. [123]	Glass spheres	89	0.7-0.85	35.62%
Kumar et al. [124]	Glass spheres	80	0.2-0.3, 0.7-0.8	34.98%, 35.2%
Okuyama et al. [126]	Aluminum spheres	240	0.114	48%
Prommas [128]	Glass spheres	40	0.15, 0.4	38.7%, 37.1%
Ranzinger et al. [129]	Glass spheres	200	2	40.2%
Yiotis et al. [130]	Glass spheres	56.6, 79.8, 300	0.1-0.85	40%

2.3.2 Evaporation from 2D porous networks

Experimental and theoretical modeling have been done in previous studies to analyze evaporation dynamics from 2D porous networks (i.e., thickness is negligible compared to length and width) to understand effects of wettability [55, 132-134], influence of contact angle [135, 136], influence of liquid island or films [136-139], effect of pore size [140-145] and heterogeneity [146] of the porous structure on evaporation. In a 10×10 (10 pores on both x and y direction)

hydrophilic (plexi-glass) and hydrophobic (Teflon) porous network, evaporation rate was 46% faster in hydrophilic than the hydrophobic one [55]. In another work with numerical simulation of evaporation from 20×20 hydrophilic and hydrophobic porous network, drying rate was 20% faster in hydrophilic than hydrophobic [132]. In a initially hydrophilic microstructure, the drying time increased significantly (from 4.7 hour to 19.9 hour) with inclusion of hydrophobicity [134]. As wettability is influenced by contact angles, drying time increased significantly from porous network with higher contact angles due to smaller air-water contact area [136]. In a simulation study, drying rate was 65% slower with contact angle greater than 90° [135]. Wettability and contact angle dynamics influence the drying pattern in 2D structure: in hydrophilic porous system, liquid films or islands in forms of capillary fingering were developed throughout the porous structure where in contrast, hydrophobic structure experienced more uniform drying pattern with little or insignificant amount of capillary liquid island formation [55, 132, 136]. The capillary fingering pattern (finger-like liquid channel in the porous media) during evaporation from hydrophilic porous system contributed to a continuous hydraulic connection which resulted in faster evaporation from hydrophilic structure compared to hydrophobic one [55, 132, 135-137] and extended period of constant rate of evaporation was found in hydrophilic structure due to formation of capillary liquid films or islands [138, 139]. The pore sizes in a 2D network also affects the drying pattern as in smaller pores, the capillary action was found significant [140, 141] resulting in more liquid island formation [144], hydraulic connection [145] and subsequent faster evaporation rate due to extended constant rate period compared to larger pores of same material. In a 2D porous structure, the evaporation rate was dominated by diffusion and can be expressed as follows [132, 135]:

$$j = D \frac{M_v (P_{vi} - P_{v\infty})}{\mathcal{R}T \delta} \quad (2.16)$$

where, j is diffusion flux, D is diffusion coefficient of water vapor, M_v is vapor molar mass, \mathcal{R} is gas constant, T is ambient temperature, P_{vi} is vapor partial pressure at the porous surface, $P_{v\infty}$ is vapor partial pressure at ambient and δ is mass boundary layer thickness.

2.3.3 Evaporation from sand/soil columns

Evaporation of water from sand or soil columns were studied experimentally [11-18, 28, 29] and numerically [147-149], and the effects of wettability on evaporation were analyzed. Shokri et al. [14, 16] conducted research on evaporation from heterogeneous sand columns. Four different columns with hydrophobic and hydrophilic sands were prepared in 260-mm-height, 75-mm-width glass beakers: (a) completely hydrophilic sand, (b) top 7 mm of hydrophobic sand on top of hydrophilic sand (c), 25 mm of hydrophobic sand on top of hydrophilic sand, and (d) 7 mm hydrophobic sand layer placed 18 mm below hydrophilic sand. The experiments were conducted for over 30 days at 45% RH and $25.9 \pm 1^\circ\text{C}$ with no external heat flux. Column ‘c’ and ‘d’ experienced the lowest cumulative mass loss due to the hydrophobic layer on top and in 18 mm below of hydrophilic sand, resulting in a disruption in hydraulic connection with the top surface. The drying front became pinned at the hydrophilic-hydrophobic interface and slower period of evaporation (0-1 mm/day) started after that. Numerical modeling of contrast wettability (i.e., mixture of hydrophilic and hydrophobic particles) also demonstrated that inclusion of 10-20% hydrophobicity reduced the characteristic length, resulting in short period of constant rate period and extended period of slower rate of evaporation [12]. Lehmann et al., [29] and Shokri et al., [13] differentiated among different stages of evaporation such as constant rate, falling rate and subsequent slower rate period. In constant rate period, water evaporates from the top surface until

it reaches to a point where the capillary connection between the saturated and unsaturated portion breaks down. After constant rate period in a heterogeneous porous media, evaporation rate decreases sharply which is falling rate of evaporation. After that, a negligible diffusion-controlled evaporation starts which is slower period of evaporation and Shokri et al., [12, 17, 28] and Moldrup et al., [150] demonstrated that the evaporation flux can be estimated by Fick's law of diffusion:

$$J = \frac{\theta_a^{2.5}}{\phi} D \frac{C_{sat} - C_\infty}{L_D} \quad (2.17)$$

Where, J is diffusive flux, θ_a is volumetric air content, ϕ is porosity, D is water-vapor diffusion coefficient, C_{sat} water-vapor density at evaporating interface, C_∞ is water-vapor density at atmosphere, L_D is drying front depth. The liquid island formation in the forms of liquid cluster was visualized with NMR (Nuclear Magnetic Resonance) technology by Shokri et al. [13]. Although the drying front propagated throughout the porous column, the liquid clusters were present in the top portion of the porous media maintaining a hydraulic connection between the saturated and unsaturated parts. The liquid islands were susceptible to form more in hydrophilic column than hydrophobic leading to an enhanced evaporation rate in the former.

2.4 Research objectives

Previous studies of evaporation from single pores and multi-pore porous media analyzed liquid island formation, hydraulic linkages, characteristic lengths, and evaporation stages, although limited studies considered the impacts of wettability. The main research objectives of this study are to investigate the impacts of wettability on evaporation mechanisms in single or multiple pores. For single pores, the research objectives are to:

- Study the effects of wettability (i.e., hydrophilic and hydrophobic) on droplet evaporation and analyze the impacts of relative humidity (RH) on evaporation.

- Study the breakup of whole droplets and formation of liquid islands during evaporation, including contact angle dynamics, droplet deformation, and rupture of liquid islands.
- Analyze contact line motion, pinning and depinning of liquid-vapor interfaces, pressure difference associated with change in curvature along liquid-vapor interface

For porous media, the research objectives are to:

- Analyze evaporation phenomena from homogeneous porous media and identify different evaporation stages.
- Analyze impacts of wettability on evaporation from porous columns with externally applied heat flux.
- Observe drying front propagation during evaporation and evaluate the effects of wettability on liquid island formation and hydraulic connectivity.
- Calculate non-dimensional heat transfer and capillary numbers to compare them with previous studies to understand evaporation phenomena.

For 3D-printed structures the research objectives are to:

- Study and analyze evaporation from three 3D-printed porous structures with engineered porous structures.
- Analyze the effects of transient saturation on drying front depth and evaluate drying front propagation during evaporation with a high-speed camera.
- Model steady-state heat transfer energy balance to predict evaporative mass flux.

Chapter 3 - Experimental apparatus

A series of experiments have been conducted to understand evaporation dynamics from single pores and porous columns. This chapter discusses experimental design, methods of data collection and the data reduction procedures for the experiments.

3.1 Evaporation of sessile droplet from single pores¹²³

Evaporation of sessile deionized water droplet was studied and analyzed from three sets of experiments from simulated soil pores created with three borosilicate glass (i.e., hydrophilic) or three polytetrafluoroethylene/Teflon (i.e., hydrophobic) spheres of the same size (2.38-mm diameter). The experiments were conducted in a closed atmospheric chamber where the temperature, pressure, and relative humidity (RH) were controlled and monitored. Some fixtures were created with additive manufacturing to hold the spheres in desired position. In experiment 1 (Evaporation from simulated soil pore: effects of relative humidity), the center-to-center distances between the spheres were maintained at 3.15 mm which created an isosceles formation. The temperature was maintained at 20°C and the pressure was kept atmospheric. Evaporation was studied at two different relative humidities (i.e., 45% and 60%) to understand the effects of RH and wettability on evaporation.

¹ Figures and parts of section originally published in “Chakraborty, P. P., & Derby, M. M. (2018, June). Evaporation from a simulated soil pore: Effects of relative humidity. In *International Conference on Nanochannels, Microchannels, and Minichannels* (Vol. 51197). American Society of Mechanical Engineers.”

² Figures and parts of section originally published in “Chakraborty, P. P., Huber, R., Chen, X., & Derby, M. M. (2018). Evaporation from simulated soil pores: Effects of wettability, liquid islands, and breakup. *Interfacial Phenomena and Heat Transfer*, 6(4).”

³ Figures and parts of section originally published in “Chakraborty, P. P., & Derby, M. M. (2020, July). Contact Line Pinning and Depinning Prior to Rupture of an Evaporating Droplet in a Simulated Soil Pore. In *International Conference on Nanochannels, Microchannels, and Minichannels* (Vol. 83693, p. V001T06A003). American Society of Mechanical Engineers.”

In experiment 2 (Evaporation from simulated soil pores: Effect of wettability, liquid island, and breakup), the temperature (i.e., 22.2° C), pressure (i.e., 1 atm) and relative humidity (i.e., 60%) were kept constant, but the geometries between the spheres were different. Two combinations were created by changing the distance between the spheres: (1) the center-to-center distance (i.e., $a = 3.1$ mm) were kept constant by creating an isosceles formation and (2) an equilateral formation was created between three spheres (i.e., $b = 2.8$ mm, $c = 2.7$ mm). The different combinations were formed to understand the effect of pore size on droplet evaporation.

In experiment 3 (Contact line pinning and depinning prior to rupture of an evaporating droplet in a simulated soil pore), the spheres' distance (i.e., 3.1 mm), temperature (i.e., 20° C) and pressure (i.e., 1 atm) were kept constant, but effects of two additional relative humidities (30% and 75%) were observed and studied. Table 3.1 represents the experimental parameters (pore size, temperature, relative humidity, pressure) of evaporation from sessile droplet from a single pore.

Table 3.1: Experimental parameters for evaporation of sessile droplet from a single pore

Experiment	Center-to-center distance (mm)	Droplet volume (μ L)	Temperature ($^{\circ}$ C)	Relative Humidity, RH	Pressure (atm)
1	3.15	4	20	45%, 60%	1
2	$a = 3.1$	4	22.2	60%	1
	$b = 2.8, c = 2.7$	4			
3	3.1	4	20	30%, 75%	1

For all experiments (single pore), 4- μ L deionized sessile water droplet was evaporated from a single pore created with three glass or Teflon spheres. The droplet was placed on the center of the pore with a 0.2-2 μ L pipette (Fisherbrand Elite) and the droplet was deposited twice as the

highest capacity of the pipette was 2- μ L. The droplet was only in contact with the spheres and did not touch the fixture. Additionally, red food color (2-3% volumetric) was applied to the deionized water to improve imaging contrast.

The evaporation phenomena were recorded and captured with a high-speed camera (Fastec IL3) with 5x magnification. An LED lamp (WD-8W) with magnetic base was used to provide sufficient lighting to the test section for better imaging. The camera recorded the process at 24 frame per second and the evaporation time was determined from the videos, recorded with Fastec Fastmotion. All experiments were replicated four times for both glass and Teflon to validate repeatability. The captured images and videos were post-processed using ActivePresenter, ImageJ, SolidWorks and PFV (Photron FASTCAM Viewer). Figure 3.1 and Figure 3.2 represent the schematic diagram of the test section and spheres orientation according to the center-to-center distance respectively for all experiments.

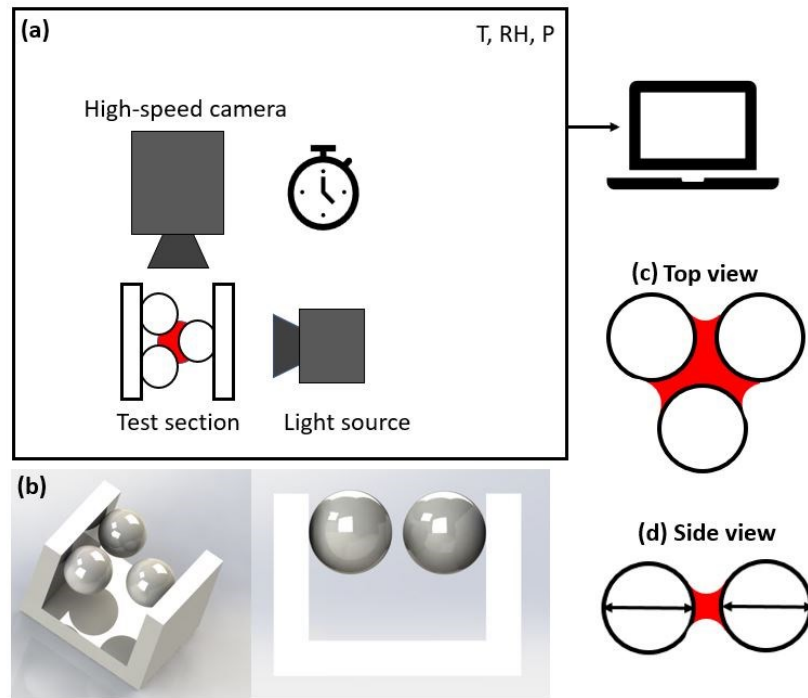


Figure 3.1: Experimental apparatus of evaporation from single pore (a) schematic of the test section in an environmental chamber (b) 3D printed structure to hold the spheres in desired

location (c) and (d) top view and side view of the droplet in a single pore [Evaporation from single pore (experiment: 1,2,3)]

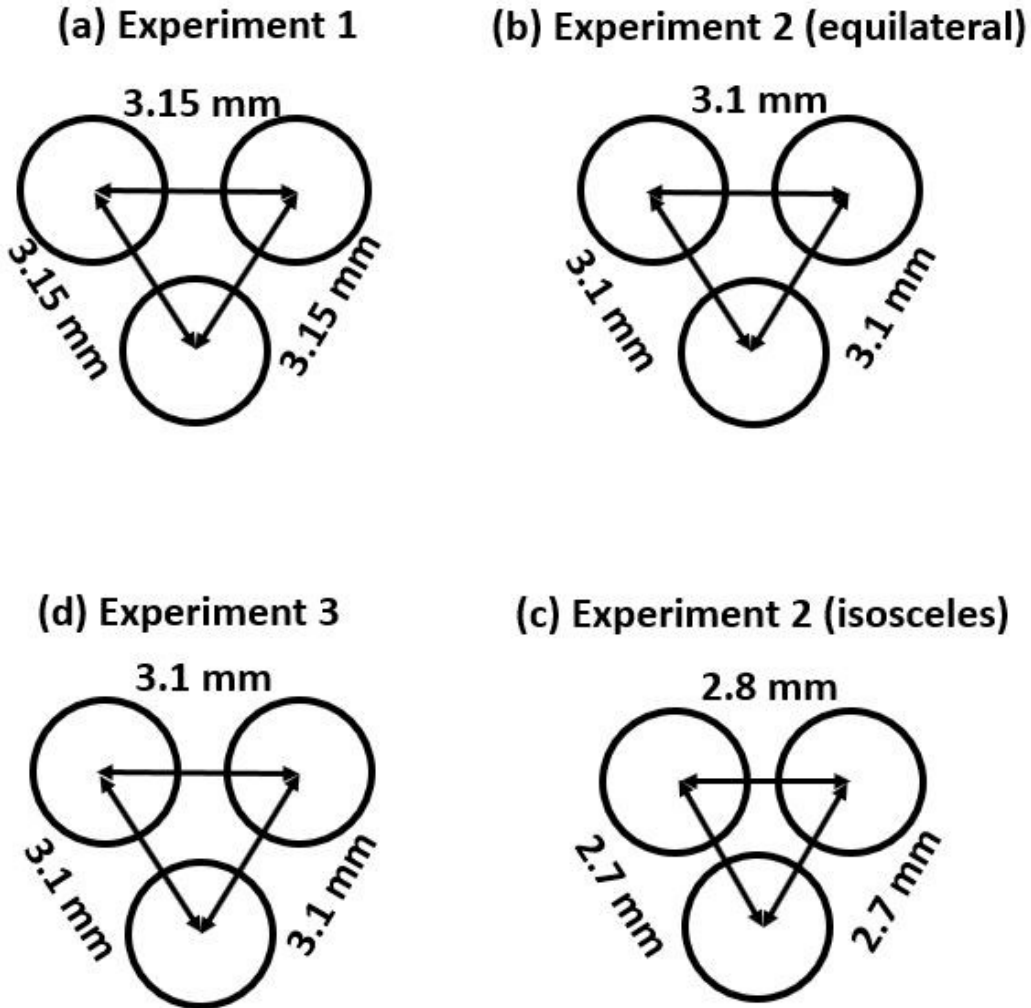


Figure 3.2: Spheres' orientation for (a) experiment 1 (center-to-center distance 3.15 mm), (b) experiment 2 (equilateral combination, center-to-center distance $a = 3.1$ mm), (c) experiment 2 (isosceles combination, $b=2.8$ mm, $c= 2.7$ mm), and (d) experiment 3 (center-to-center distance 3.1 mm)

3.1.1 Physical properties of glass and Teflon spheres

Borosilicate glass and PTFE (polytetrafluoroethylene) spheres with diameter of 2.38 mm were used for conducting these experiments. The spheres were procured from McMaster-Carr

(8996K21 and 9660K21, respectively) with stated sphericity of 99.90% with diameter tolerance of ± 0.0051 and ± 0.051 mm for glass and Teflon, respectively. To check the spheres' diameters, ten random glass and ten random Teflon spheres were chosen and the diameters were measured with a digital caliper. The average diameter was found 2.378 mm (0.0042 standard deviation) and 2.377 mm (0.0041 standard deviation) for glass and Teflon respectively. To observe the surface roughness, SEM (Scanning Electron Microscope) images (Figure 3.3) were captured with a Zeiss Evo MA10 microscope (accelerating voltage 200 V- 30 KV).

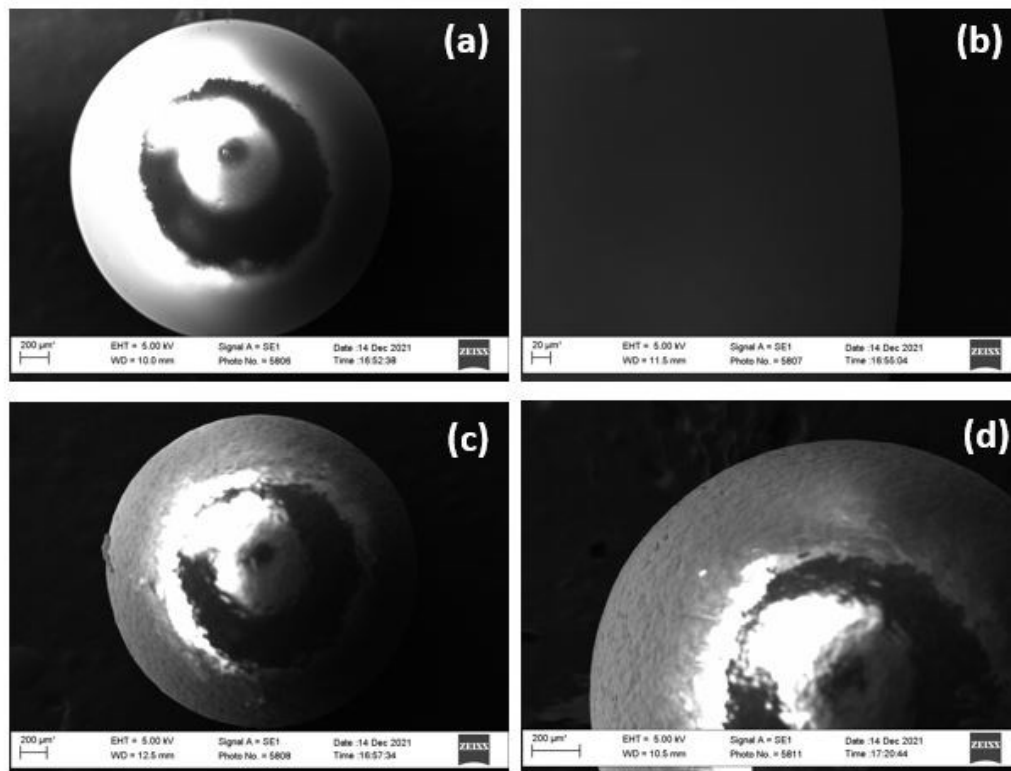


Figure 3.3: SEM (Scanning Electron Microscope) images of glass (a and b) and Teflon (c and d) spheres [151]

3.2 Evaporation from simulated soil columns

This experiment was done in two parts. In first part, a small hydrophilic porous column was prepared, and water was evaporated. In second part, two large columns made with hydrophilic and hydrophobic spheres were made to compare effect of wettability on evaporation.

3.2.1 Evaporation from small hydrophilic porous column ⁴

A simulated hydrophilic soil column was prepared for this experiment in a 2-cm-diameter, 3-cm-tall glass beaker filled with ~1720 2-mm-diameter borosilicate glass spheres. Experiments were conducted in a quiescent atmosphere where the relative humidity (RH) was 35% (maximum deviation of $\pm 2\%$) and the temperature was $22.2 \pm 0.2^\circ\text{C}$. A RH 62F rugged hygrometer (Omega engineering) (uncertainty 0.1%) was used to record and monitor temperature and RH of the air. Figure 3.4 represents the schematic of the experimental apparatus.

A total of 5.5-mL deionized water was added to the beaker filled with glass spheres and the beaker was placed on top of a sensitive scale (A&D, FX-1200i) to measure subsequent mass loss due to evaporation. An Abet LS-10500 solar simulator was used to apply a constant heat flux on top of the evaporative surface to mimic the effect of sun. The solar simulator has a maximum beam size of 35 mm, and a 90° beam tuner was used to project the beam on the top surface of the beaker vertically. For this experiment, 1500 W/m^2 heat flux was applied, and the beam size was maintained at 20 mm which encapsulates the whole top surface of the beaker. A LI-200R

⁴Figures and parts of section originally published in “Chakraborty, P. P., Ross, M., Bindra, H., & Derby, M. M. (2019, July). Liquid Transport During Evaporation of Water From a Small Simulated Soil Column. In *Heat Transfer Summer Conference* (Vol. 59315). American Society of Mechanical Engineers”

pyranometer with a sensitivity of $75 \mu\text{A}$ was used to measure the heat flux produced by the solar simulator.

To visualize the evaporative drying front propagation during evaporation, x-ray imaging was used to capture the images of the test section. An x-ray generator (AP72) and a detector (0822 xo/xp) were used to capture x-ray images where the pixel size of x-ray detector is $200 \mu\text{m}$ and the energy capacity is 20 kV-15 MV. The distance between x-ray generator and detector was maintained at 55 cm and the beaker was placed adjacent to the x-ray detector ($\sim 2 \text{ mm}$) to improve image quality. X-ray images were captured at 1 hour time intervals for the first four hours and then they were captured at 8 hours' interval until the end of replication. A T-type thermocouple was inserted at a depth of 1 cm to measure the temperature during evaporation and a thermocouple fixture was used to hold the thermocouple in fixed position. The thermocouple was connected to an Agilent 34972A and the data were logged with Agilent Benchlink data logger with 5 minutes' time interval. The experiment was replicated three times.

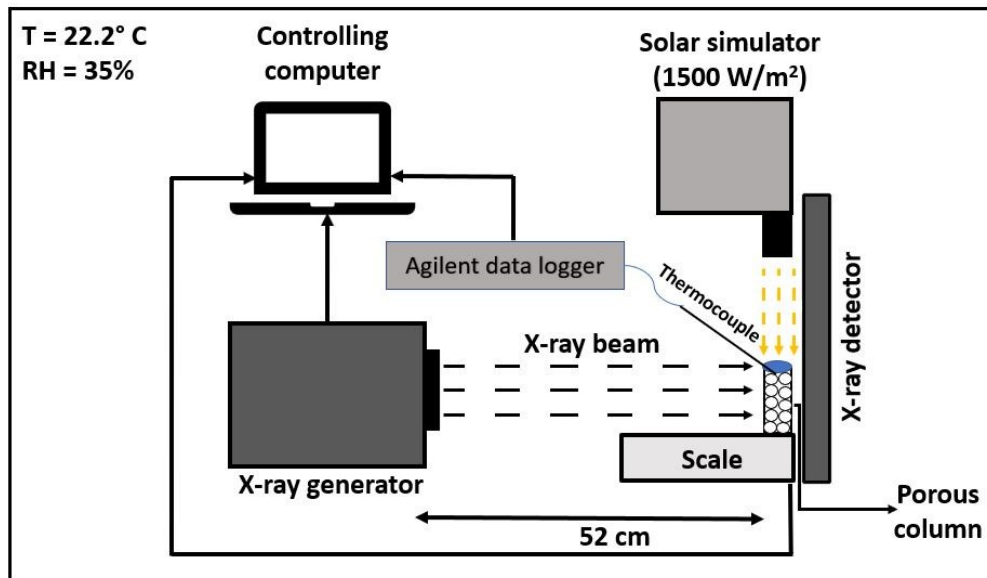


Figure 3.4: Schematic of evaporation from small hydrophilic porous column in a controlled atmosphere with $T = 22.2^\circ\text{C}$ and $\text{RH} = 35\%$

3.2.2 Evaporation from hydrophilic and hydrophobic porous column to study effects of wettability ⁵

In this experiment, evaporation of deionized water was studied from two separate porous columns made with ~1165 hydrophilic glass and hydrophobic Teflon spheres of same sizes (2.38 mm diameter), and the spheres were placed in two cylindrical borosilicate glass beakers (1.88-cm-inner-diameter, 6-cm-height, 0.126-cm-thickness). The experiments were conducted in a quiescent atmosphere with average relative humidity of $60 \pm 1\%$ and temperature of 22.2°C . The temperature and RH were recorded at 5 minutes' time interval with an OM-24 multiuse PDF temperature and humidity data logger (Omega Engineering) with $\pm 0.5^\circ\text{C}$ of temperature and $\pm 3\%$ of RH accuracy. Figure 3.5 and Figure 3.6 demonstrate the average temperature and RH and schematic of experimental apparatus, respectively.

A total of 5.8 mL of deionized water was added in the beaker, and it was evaporated under simulated sunlight. The evaporative mass loss was measured and recorded with an A&D, FX-1200i sensitive scale with ± 0.01 g of uncertainty. RS-multi software was used to record mass loss data at 5 minute's intervals. An Abet LS-10500 solar simulator was used to apply 1000 W/m^2 on top of the evaporative surface. A 2.36-cm-diameter, 3.63-cm-height LI-COR LI-200R pyranometer with a sensitivity of $75 \mu\text{A}$ per 1000 W/m^2 was used to measure the heat flux produced by the solar simulator and a 90° beam tuner was used to project the beam vertically on the top of

⁵ Figures and parts of section Reproduced with permission from Springer Nature“Chakraborty, P. P., Ross, M., Bindra, H., & Derby, M. M. (2022). Evaporative Drying from Hydrophilic or Hydrophobic Homogeneous Porous Columns: Consequences of Wettability, Porous Structure and Hydraulic Connectivity. *Transport in Porous Media*, 1-28”

the beaker. The intensity of the produced heat flux is inversely proportional to the beam diameter and the distance from the light source to top surface of the test section.

X-ray images were captured to visualize the drying front propagation. An EPX-Ecotron x-ray generator with operating parameters of 40 KeV and 20 mAs and a square (i.e., 20 cm by 20 cm) flat x-ray detector (Perkin-Elmer flat panel) with an exposure time of 250 ms were used to capture the x-ray images. The distance between the x-ray generator and detector was maintained at 30 cm and the beaker was placed in front of the detector with negligible distance (~ 2 mm) for better image quality. The vertical distance between the solar simulator and top surface of the beaker was kept at approximately 6 cm. The x-ray images were captured from the third day until the seventh day (i.e., end of replication) at 24 hours' interval. The duration of each experiment was seven days, and each experiment was replicated five times.

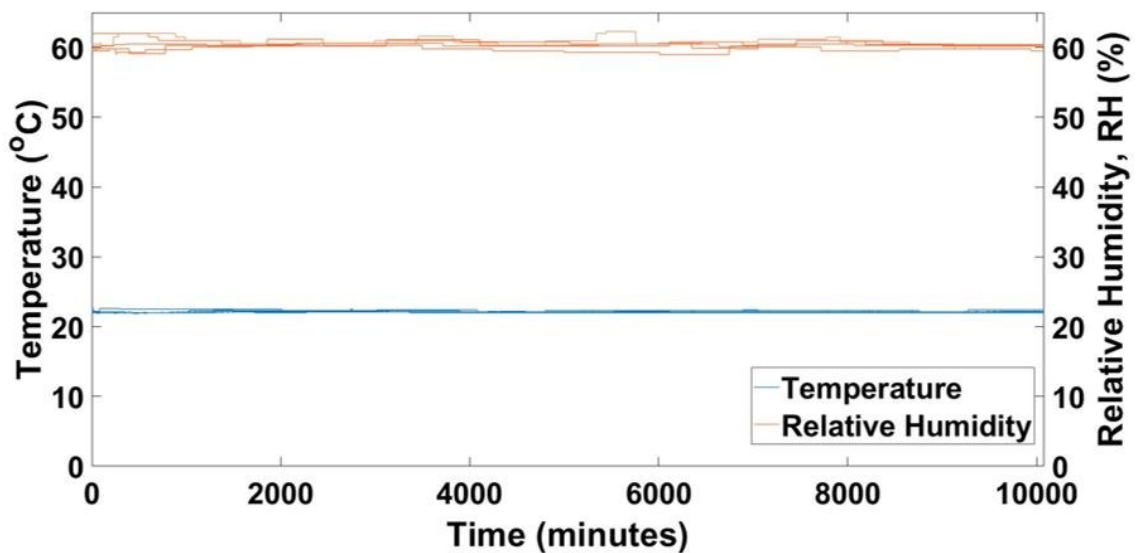


Figure 3.5: Average temperature (22.2°C) and relative humidity (60±1%) of the experimental atmosphere [151]

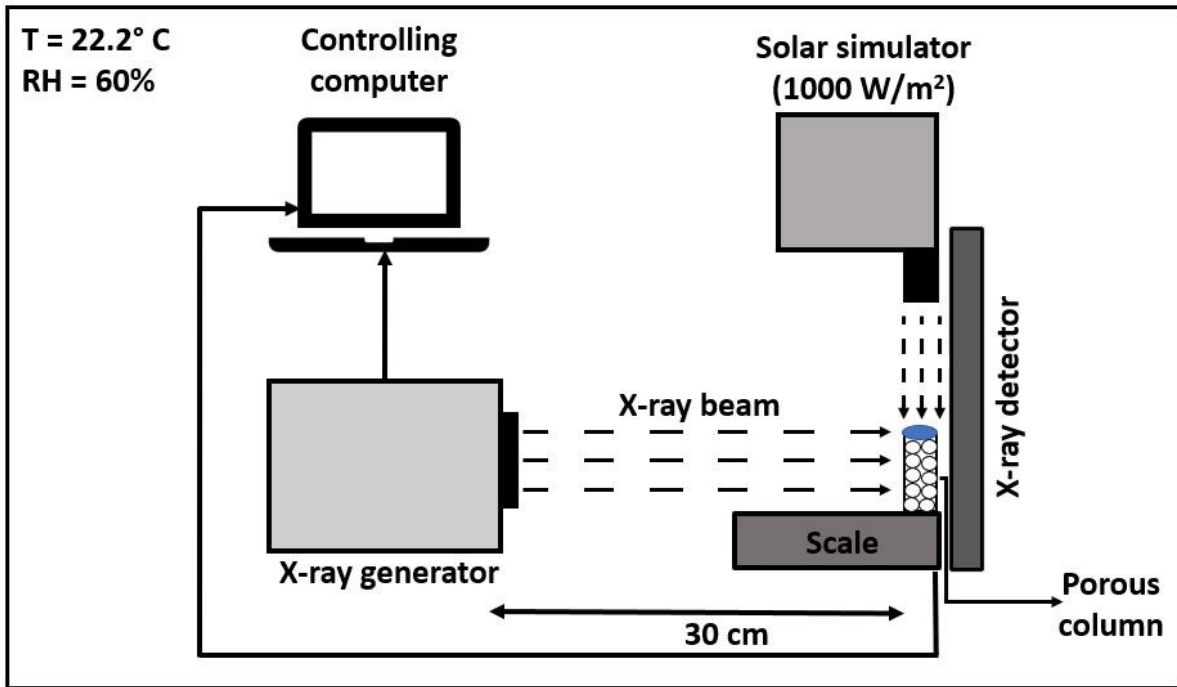


Figure 3.6: Experimental apparatus of the test section in a controlled atmosphere where $T = 22.2^\circ\text{C}$ and $\text{RH} = 60\%$ [151]

3.2.3 X-ray image capturing technique

Similar techniques were applied to capture images by x-ray for both experiments. At first, the beaker filled with spheres was placed in front of the x-ray detector on the top of the scale and an initial image (i.e., reference image) was captured without any water. Then, a constant amount of water (5.5 mL for first and 5.8 mL for second experiment) was added to the beaker filled with spheres and the evaporation was started due to the heat flux imposed by the solar simulator. From the beginning of the evaporation, x-ray images were captured at a certain time interval till the end of the evaporation. The x-ray generator was controlled with a software called XIS to capture image by using a manual trigger. Three images at a single time frame were captured for better resolution and the images were post-processed in MATLAB.

3.2.4 X-ray image post-processing

All the x-ray images were post processed using a MATLAB code where the reference image (i.e., beaker and spheres without any water) were subtracted from all images to visualize the water level and the drying front propagation during evaporation. Exponential attenuation of x-rays through materials including determination of log transform of the image pixel values were considered for post processing of x-ray images. The attenuation of x-rays through any material follows the Beer-Lambert law:

$$\frac{I}{I_0} = e^{-\eta t} \quad (3.1)$$

where, η is attenuation coefficient, t is the material thickness, I_0 is the x-ray beam intensity, and I is the attenuated x-ray intensity. The detector response is directly proportional to the x-ray intensity such that a pixel value can be defined in the same way:

$$a = C e^{-\eta t} \quad (3.2)$$

where, a is the detector response and C is a coefficient. Assuming the x-ray beam and detector settings to be constant, so the material attenuation is directly related to the log transformed pixel value:

$$b = \log(a) \quad (3.3)$$

where, b is log-transformed pixel value. An image of the beaker without water and with full of water are defined as b_a and b_w respectively. Assuming a linear relationship between the attenuation of the background and the water, the fractional volume of water can be calculated by:

$$V_{frac} = \frac{b - b_a}{b_w - b_a} \quad (3.4)$$

where, V_{frac} is fractional volume of water.

3.3 Evaporation of water from 3D printed structure

In this experiment, deionized water was evaporated from three 3D printed structures manufactured with ABS translucent material.

3.3.1 3D-printed porous structures

Three 3D-printed structures were manufactured for these experiments. The structures were designed in SolidWorks and were manufactured by PROTOLABS. All the structures were fabricated using stereolithography with ± 0.1 mm of thickness resolution and ABS translucent material (1.25 g/cm^3 density) was used to build the structures. Figure 3.7 shows the front, side, and top views of the 3D-printed structures. 3D structure-1 was manufactured with 360 uniform spheres of 1.2-mm-diameter stacked in 10 layers with 1.43 mm center-to-center spacing. The spheres were connected among themselves with 0.2-mm-diameter cylinder in x, y and z directions, and each layer contained 36 spheres. The total mass (i.e., mass of 3D structure) was 0.42 g with a porosity of 45.87%. 3D structure-2 is similar to 3D structure-1 except that two layers in the y-z direction were filled with solid material to restrict lateral movement of water. As a result of the filled in areas, the structure had porosity of 30.58% with 0.61 g of mass.

In 3D structure-3, 1.2-mm-diameter spheres were used in x, y, and z directions but the center-to-center distances were 2 mm, larger than structures 1 and 2. Similar to 3D structures 1 and 2, the spheres were connected with 0.2-mm-diameter cylinders in x, y and z directions. Four spheres in a single plane were connected with a cross structure made with 0.2-mm-diameter cylinder the x, y and z directions. To vary the pore size in the z-direction, a horizontal cross shaped structure was incorporated in the middle of each layer. Structure 3 had a porosity of 33.27% with 1.31 g of total mass.

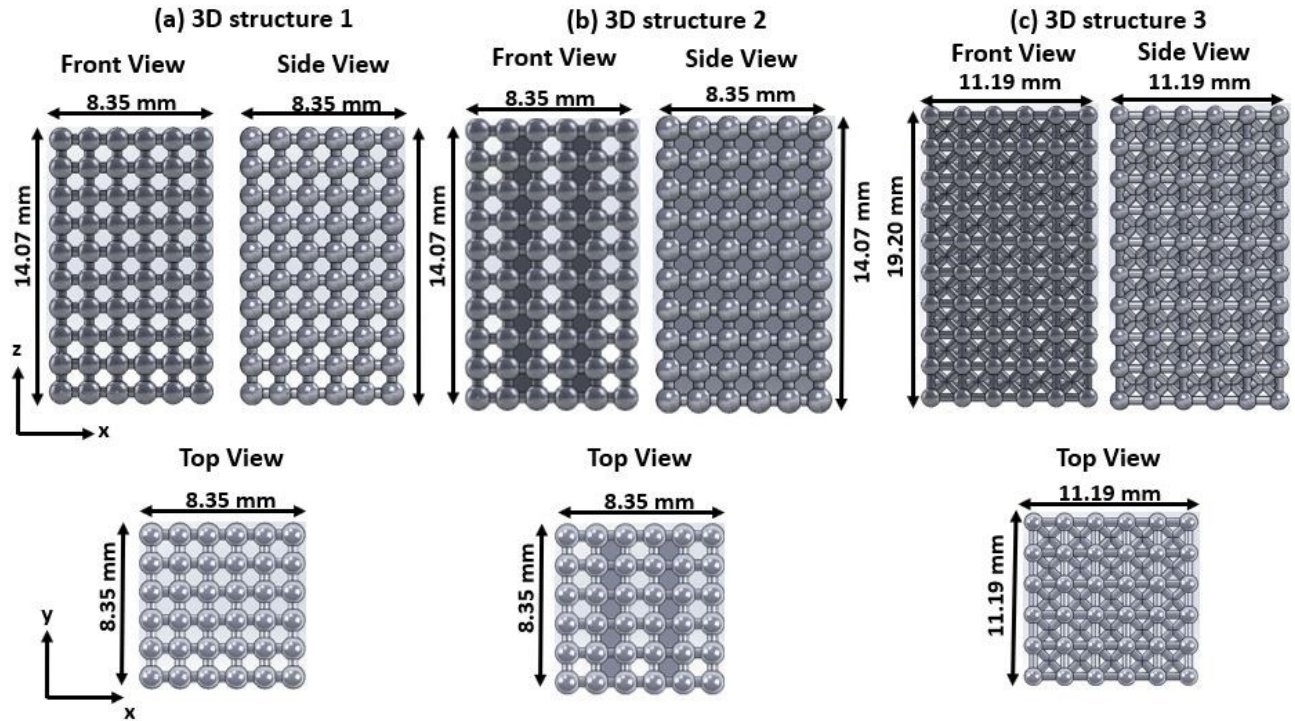


Figure 3.7: Front view, side view and top view of (a) 3D structure 1, (b) 3D structure 2 and (c) 3D structure 3

Table 3.2: Dimensions of three 3D printed porous structures

	3D structure 1	3D structure 2	3D structure 3
Dimension (L, W, H), mm	8.35, 8.35, 14.07	8.35, 8.35, 14.07	11.19, 11.19, 19.2
Porosity, ϕ (%)	45.87	30.58	33.27
Mass (g)	0.42	0.61	1.31
Effective pore radius (mm)	0.41	0.41	0.16

3.3.2 Wettability of 3D-printed material

Translucent ABS was selected for the 3D-printed structures to aid visualization of water with a high-speed camera. The material has density of 1.25 g/cm^3 with $55 \pm 10 \text{ MPa}$ of tensile

strength. The material is typically hydrophilic and to measure the contact angle, a small flat plate (L=30 mm, W = 30 mm, H = 3 mm) was 3D-printed with the same material. A 1- μ L water droplet was placed on the top of ABS flat surface with a 0.2-2 μ L pipette (Fisherbrand Elite) and the contact angle was measured using a goniometer. Figure 3.8 shows the contact angle measurement of 1- μ L water droplet on flat ABS surface and the material is hydrophilic since the contact angle is 36.92° (i.e., less than 90°).

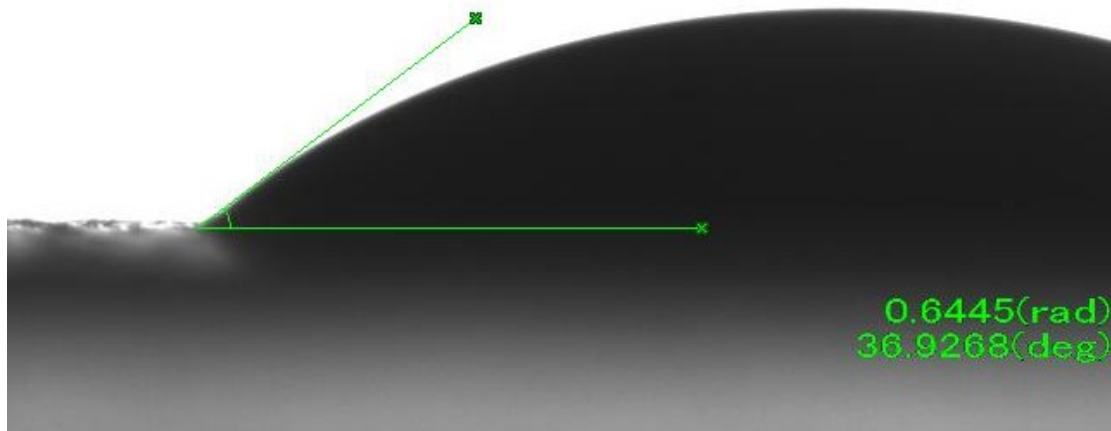


Figure 3.8: Contact angle (36.92°) on flat ABS translucent surface

3.3.3 Evaporation of water from 3D printed porous structure

Evaporation of deionized water from all three 3D-printed porous structures was experimented in a closed atmosphere with $T = 22.2^\circ\text{C}$, $\text{RH} = 13\text{-}17\%$ and $P = 1 \text{ atm}$ (Figure 3.9). Initially, the deionized water was placed in a beaker (2 cm diameter, 3 cm height). Then, the 3D-printed structure was dipped fully in the deionized water with tweezers until all the pores were invaded with water. Next, the structure with water was placed on the top of a sensitive scale (FX-1200i, A&D) with $\pm 0.01 \text{ g}$ of uncertainty. The 3D printed structure with water was placed on the

top of the scale to expose the sides of the structure to evaporation (i.e., experiments were always conducted without a container). A heat flux of 1000 W/m^2 was applied on the top of the structure with an Abet LS-10500 solar simulator and a 90° beam tuner was used to apply the simulated solar light vertically on the top of the test section. The heat flux was measured with a LI-COR LI-200R pyranometer with a sensitivity of $75 \mu\text{A}$ per 1000 W/m^2 . The evaporation phenomenon and drying front propagation was observed and recorded with a Fastec IL3 high-speed camera at 24 FPS (Frame Per Second) and total evaporation time were monitored. To observe the temperature profile of the test section, a Teledyne FLIR E8-XT thermal camera with 320×240 pixels resolution was used to capture thermal images at 15 minutes intervals. The mass loss was recorded at 15 minute intervals with RS-Multi software to monitor evaporative mass loss, and each experiment was replicated three times.

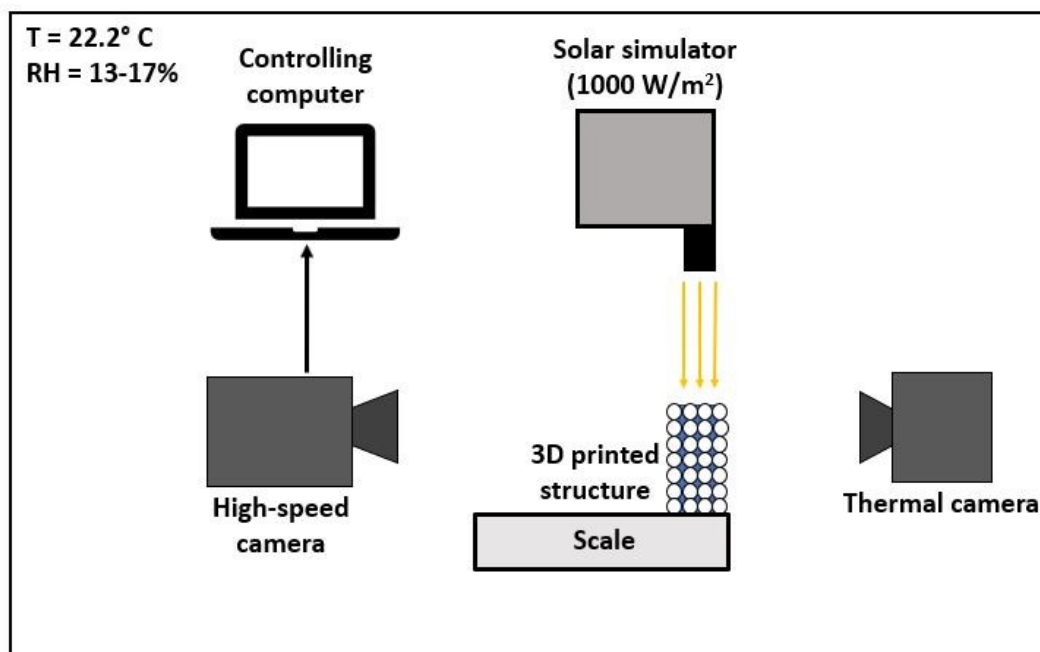


Figure 3.9: Schematic of evaporation of water from 3D printed porous structure

Chapter 4 - Evaporation from single pores

Evaporation from a single artificial soil pore created with three glass or Teflon spheres was been studied and the subsequent effects of atmospheric conditions such as relative humidity (RH), geometric configurations (e.g., pore size), breakup of whole droplets, formation of liquid islands, contact line pinning and depinning were analyzed to understand droplet deformation while evaporation. Since the experiments were conducted in three parts, the experimental and theoretical results will be analyzed and discussed sequentially.

4.1 Experiment 1- Evaporation from single pore: Effects of Relative Humidity ⁶

In this experiment, evaporation of 4- μ L water droplets were observed and analyzed at 45% and 60% RH for both hydrophilic (i.e., glass) and hydrophobic (i.e., Teflon) pores of same sizes. The center-to-center distance between the spheres were 3.15 mm. The evaporation phenomena were captured with a high-speed camera and the evaporation times were recorded; each experiment was replicated four times. In this study, along with the effect of relative humidity and wettability on droplet evaporation, the formation and propagation of liquid islands was also investigated.

4.1.1 Evaporation time

Table 4.1 represents the total time required to evaporate 4- μ L water droplet at 45% and 60% RH from both hydrophilic and hydrophobic pores. The total evaporation time for all four replicates were nearly identical. For glass (hydrophilic), the evaporation was faster than Teflon for both relative humidities: at 45% and 60% RH, the average time of evaporation was 1.11 times and

⁶ Figures and parts of section originally published in “Chakraborty, P. P., & Derby, M. M. (2018, June). Evaporation from a simulated soil pore: Effects of relative humidity. In *International Conference on Nanochannels, Microchannels, and Minichannels* (Vol. 51197). American Society of Mechanical Engineers.”

1.24 times faster than Teflon. The experimental results showed direct independence of evaporation on relative humidity (RH): for larger driving potential differences (i.e., lower air relative humidity), evaporation rates were faster. At 45% RH, the average evaporation time for glass and Teflon pores were 26 and 29 minutes, respectively, and at 60% RH, the evaporation times were 34 and 42 minutes, respectively. Evaporation phenomena correspond to the difference in relative humidity, which can also be expressed using humidity ratio:

$$\omega = \frac{m_v}{m_a} = 0.622 \frac{p_v}{p - p_v} \quad (4.1)$$

where, m_v is mass of water vapor, m_a is mass of dry air, p_v is partial pressure of water vapor and p is total pressure. At $T = 20^\circ \text{C}$, humidity ratios are $0.00652 \text{ kg}_w/\text{kg}_a$ at 45% RH and $0.00873 \text{ kg}_w/\text{kg}_a$ at 60% RH from psychrometric chart. For the liquid water droplet, the humidity ratio is $0.0146 \text{ kg}_w/\text{kg}_a$, so the driving potential for evaporation at 45% RH (i.e., $0.0081 \text{ kg}_w/\text{kg}_a$) is greater than at 60% RH (i.e., $0.0059 \text{ kg}_w/\text{kg}_a$). The greater driving potential corresponds to faster evaporation of same amount of water for the drier condition (i.e., 45% RH).

Table 4.1: Evaporation time for 4 μL water droplet at 45% and 60% RH from hydrophilic (glass) and hydrophobic (Teflon) pores

	Replication number	45% RH	60% RH
		Evaporation time (minutes)	Evaporation time (minutes)
Glass	1	27	32
	2	26	33
	3	27	35
	4	25	34
	Average time	26	34
Teflon	1	30	38
	2	28	43
	3	29	44
	4	29	41
	Average time	29	42

During evaporation, the whole water droplet reduced in size due to evaporative mass loss. Figure 4.1 and Figure 4.2 represent the images of droplet deformation due to evaporation at different time frame for glass and Teflon at 45% and 60% RH respectively. Initially, 4 μL water droplet containing 2-3% red food color was placed in the pore created with three hydrophilic glass [Figure 4.1 (a), Figure 4.2 (a)] and hydrophobic Teflon pores [Figure 4.1 (f), Figure 4.2 (f)]. Eventually, the droplet deformed its original shape and at a certain time frame it created a liquid island between two spheres [Figure 4.1 (c, h) and Figure 4.2 (c, h)].

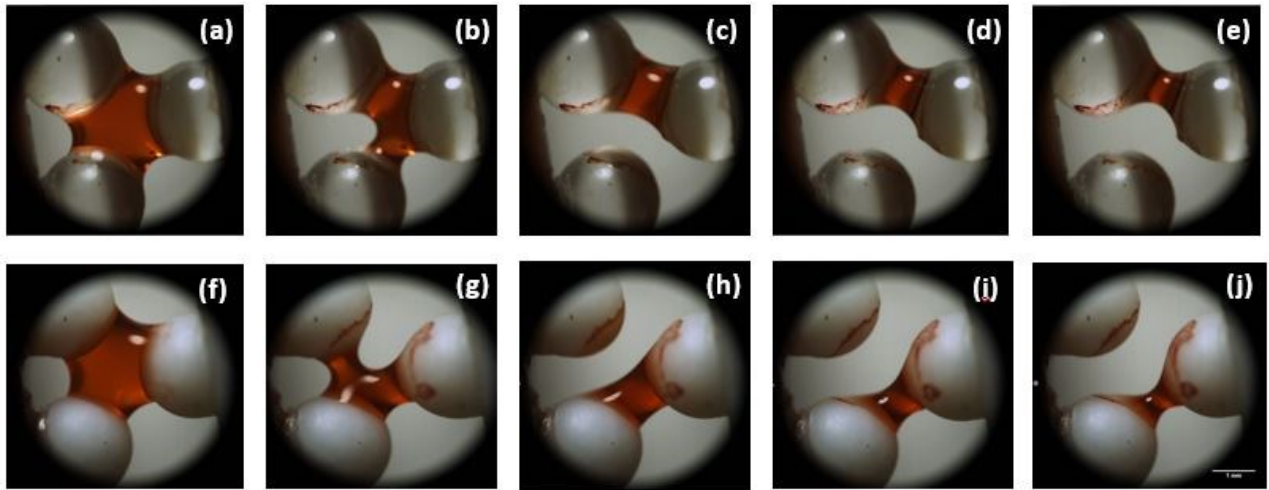


Figure 4.1: Evaporation of 4- μL water droplet from glass (a-e) and Teflon (f-j) pores at 45% RH; (a) and (f) correspond to $t = 0$ min, (b-e) and (g-j) are droplets at 14, 15, 21, 24 and 20, 21, 27 and 30 minutes, respectively, for glass and Teflon pores [31]

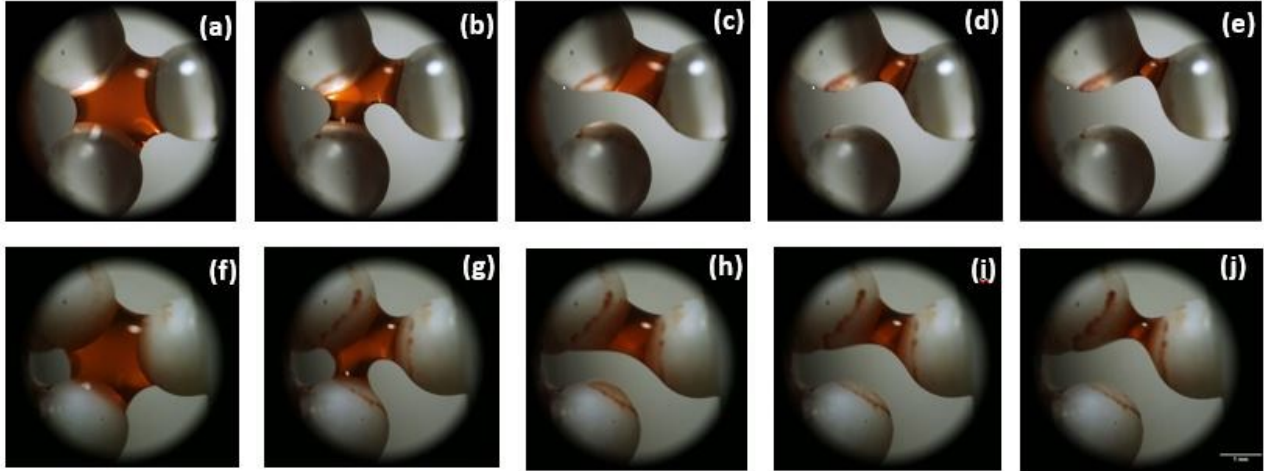


Figure 4.2: Evaporation of 4 μL water droplet from glass (a-e) and Teflon (f-j) pore at 60% RH. (a) and (f) the initial position at $t = 0$ min, (b-e) and (g-j) are droplet state at 17, 18, 27, 30 and 26, 28, 36 and 42 minutes respectively for glass and Teflon [31]

4.1.2 Formation of liquid islands

During evaporation, the whole water droplet breaks down and forms a liquid island between two spheres. In their pioneering work, Philip and De Vries [21, 22] analyzed transport through liquid islands formed between soil particles under an influence of temperature gradient. In previous studies [21, 22, 119, 152-154], the evaporation by vapor diffusion was estimated to be 1.5-5 times higher than the prediction of Fick's diffusion law and Philip and De Vries [21, 22] indicated the temperature gradient as enhancement factor. Due to an applied temperature gradient, one side of the liquid island will experience evaporation with a gradual decrease in radius of curvature and the other side will experience condensation with an increase in radius of curvature [Figure 4.3 (a)]. The current study was conducted in an isothermal atmosphere where temperature gradient across the liquid island was absent and both sides of the liquid island experienced gradual decrease in radius of curvature due to evaporation [Figure 4.3 (b)].

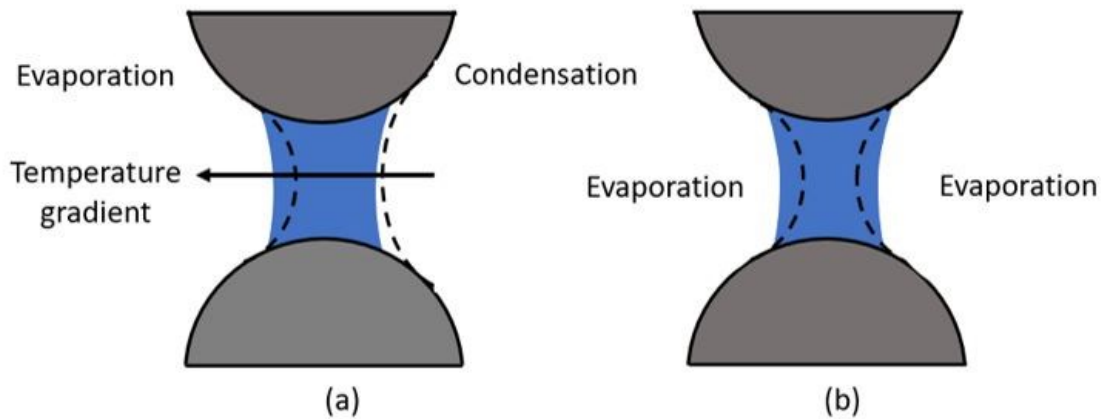


Figure 4.3: Liquid island formed between two particles (a) for a non-isothermal situation, due to temperature gradient one side of the liquid island is experiencing evaporation and the other side is experiencing condensation (b) for an isothermal situation, both sides of the liquid island are experiencing evaporation

Breakup of whole droplet and formation of a liquid islands between two particles is an important phenomena of evaporation dynamics of porous media. The droplets breakup indicates the termination of constant rate of evaporation and beginning of falling rate period of evaporation and reduction in liquid islands size and subsequent breakup indicates slower period of evaporation in a porous media. In this study, the radius of curvature of liquid islands from both sides were measured with SolidWorks 2018 at one minute time intervals from the beginning of formation of liquid islands until the rupture for both glass and Teflon at 45% (Figure 4.4) and 60% (Figure 4.5) RH. For both cases, the change in radius of curvature due to reduction were almost similar and, in most time frames, they overlapped. As the experiment was conducted in an isothermal atmosphere, both sides of the liquid islands experienced reduction at same rate due to evaporation.

For both cases (45% and 60% RH), the liquid islands formed in glass pores experienced sharp decrease from the beginning until the end of evaporation. But in Teflon, the liquid islands

retained its initial radius of curvature (i.e., the liquid islands did not change its shape until first five minutes and then it gradually decreased with time).

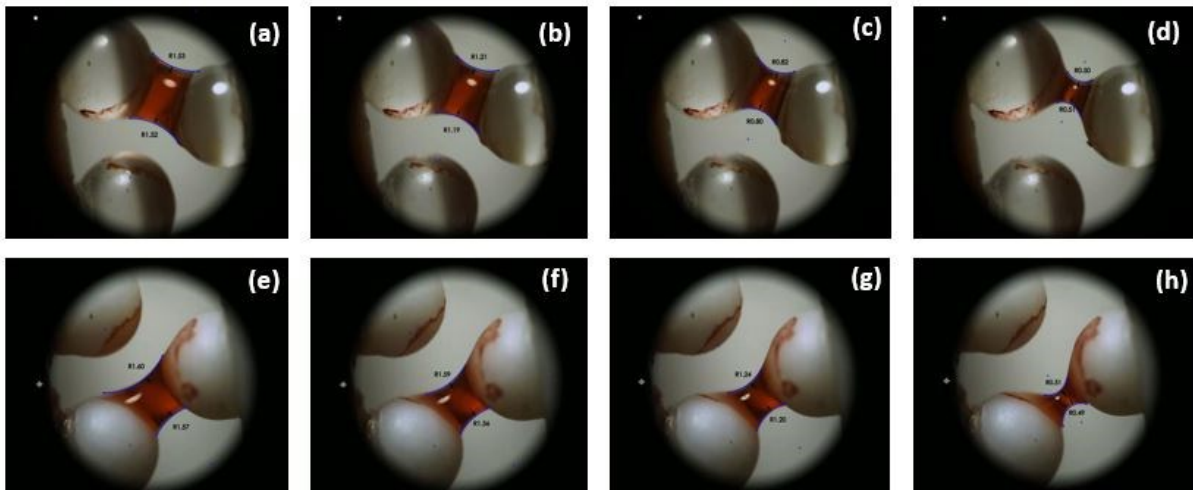
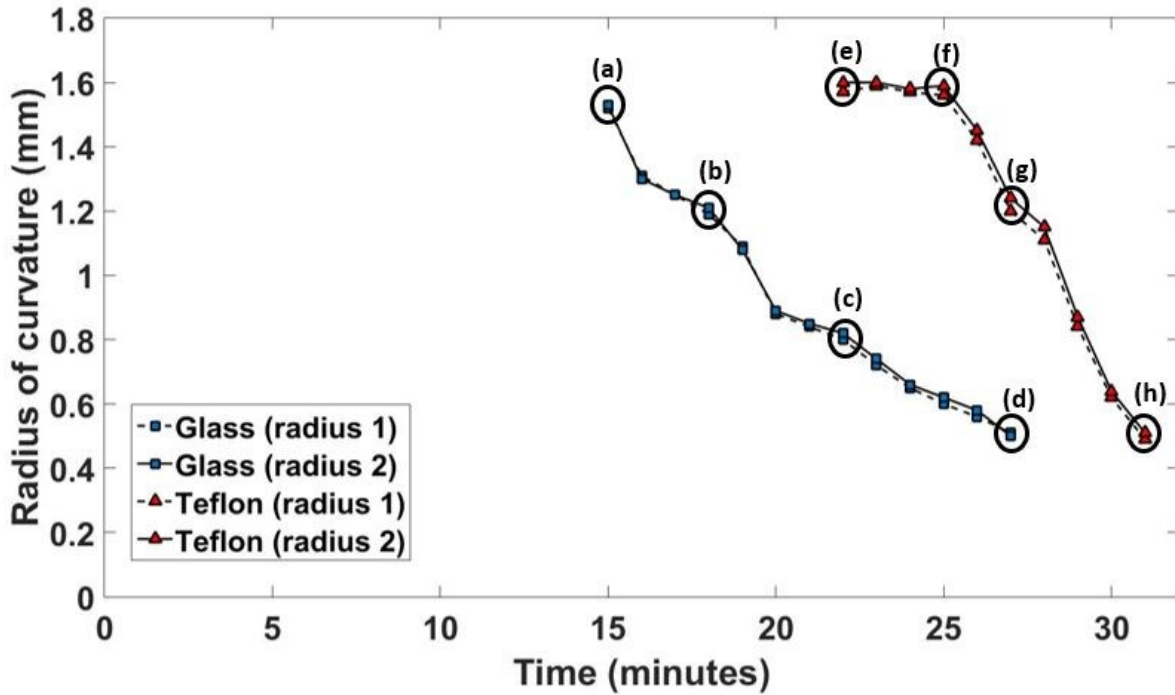


Figure 4.4: Change of radius of curvature of the liquid island at 45% RH for glass (a-d) and Teflon (e-h). The radius was measured on both sides (radius 1 and 2) and plotted on the same graph to demonstrate the gradual decrease of radius due to evaporation on both sides [31]

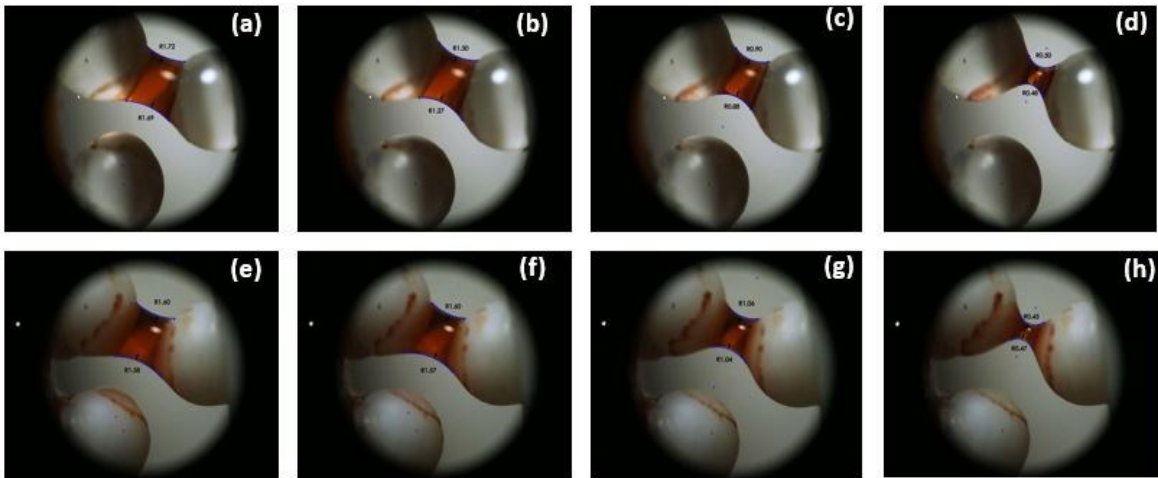
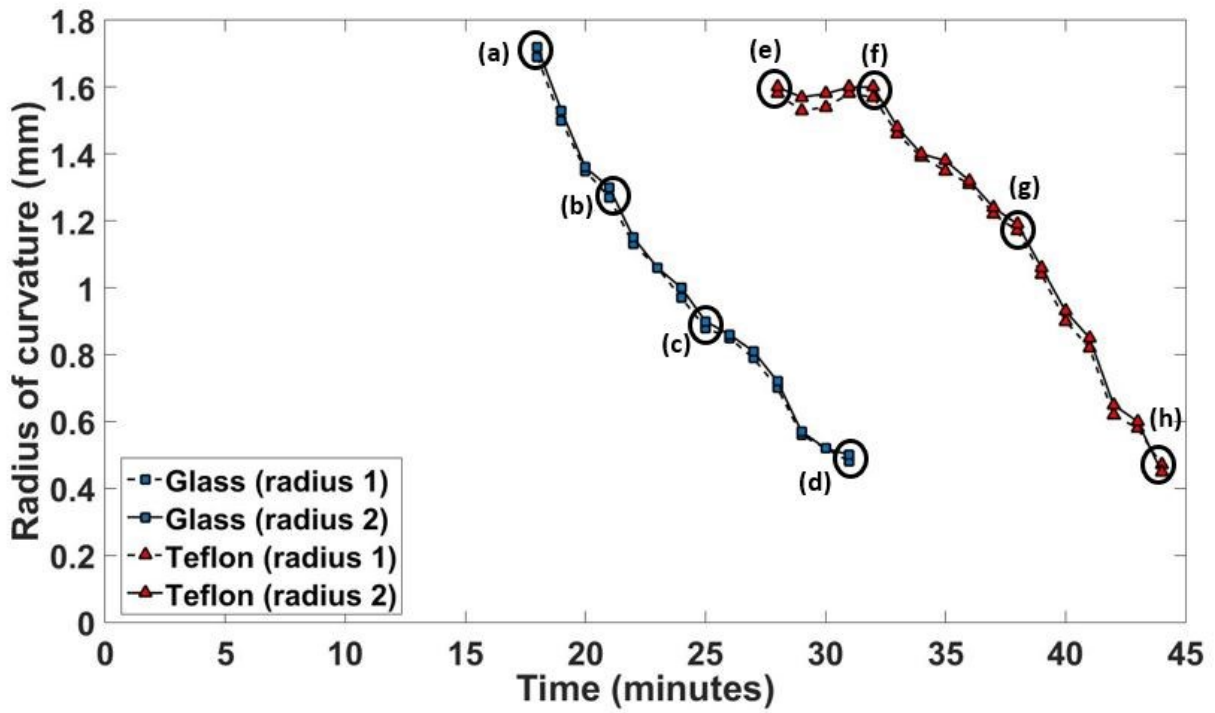


Figure 4.5: Change of radius of curvature of the liquid island at 60% RH for glass (a-d) and Teflon (e-h). The radius was measured on both sides (radius 1 and 2) and plotted on the same graph to demonstrate the gradual decrease of radius due to evaporation on both sides [31]

4.2 Experiment 2 – Effects of wettability, liquid island, and breakup on evaporation from simulated soil pores⁷

In this experiment, 4- μ L water droplets were evaporated from a simulated soil pore made with three glass or Teflon spheres (2.38-mm-diameter) and two different combinations of pore sizes (isosceles and equilateral) was used to understand the effect of pore size on evaporation. During evaporation, the whole droplet breaks up and creates a liquid island between two spheres and the formation of liquid island has been evaluated in this study. Then other droplet properties such as projected areas, contact angle dynamics of liquid island, change in volume, and analysis of rupture strength of the liquid island have also been analyzed in this study. The atmospheric conditions ($T = 22^\circ \text{C}$, 60% RH) were similar for all replications.

4.2.1 Evaporation time and projected area

The evaporation phenomena were recorded and captured with a high-speed camera for glass and Teflon pores for both configurations (i.e., equilateral/ symmetric, and isosceles/ asymmetric); each experiment was repeated four times. The pore geometry was showed in Figure 3.2 (b and c). Table 4.2 represents the evaporation time for all replications. For both combinations, evaporation rate was faster in glass (i.e., 34 minutes for the isosceles configuration [Figure 3.2 (c)] and 42 minutes in equilateral [Figure 3.2 (b)]) than Teflon (i.e., 42 minutes in isosceles [Figure 3.2 (c)] and 55 minutes in equilateral [Figure 3.2 (b)]). Based on evaporation time, evaporation was 1.23 times and 1.3 times faster in hydrophilic (i.e., glass) pores than hydrophobic (i.e., Teflon) pores. The pore size also contributed to the evaporation; in the smaller pore (i.e., equilateral), the evaporation rate was slower than the larger (i.e., isosceles) pore for both glass and Teflon (Table

⁷ Figures and parts of section originally published in “Chakraborty, P. P., Huber, R., Chen, X., & Derby, M. M. (2018). Evaporation from simulated soil pores: Effects of wettability, liquid islands, and breakup. *Interfacial Phenomena and Heat Transfer*, 6(4).”

4.2). As the center-to-center spacing was larger in the equilateral configuration, the droplet created more solid-liquid contact area and the increased evaporative surface area contributed to faster evaporation than isosceles/asymmetric combination.

Table 4.2: Evaporation time for 4- μ L water droplet from hydrophilic and hydrophobic pores for both equilateral and isosceles combination at 60% RH

Glass (equilateral) a = 3.1 mm		Teflon (equilateral) a = 3.1 mm		Glass (isosceles) a = 2.7 mm, b = 2.8 mm		Teflon (isosceles) a = 2.7 mm, b = 2.8 mm	
Replicati on Number	Evaporati on Time (Minutes)	Replicati on Number	Evaporati on Time (Minutes)	Replicati on Number	Evaporati on Time (Minutes)	Replicati on Number	Evaporati on Time (Minutes)
1	32	1	38	1	42	1	55
2	33	2	44	2	43	2	56
3	35	3	43	3	39	3	53
4	34	4	41	4	41	4	54
Average Time: 34 minutes		Average Time: 42 minutes		Average Time: 42 minutes		Average time: 55 minutes	

During evaporation, the droplet changed its shape and reduced its size due to evaporative mass loss. Eventually, the whole droplet broke up and created a liquid island between two of the three spheres. The projected areas were measured for the whole droplet and liquid islands from the beginning until just before rupture at two minute's interval and plotted against time [Figure 4.6 (whole droplet) and Figure 4.7 (liquid island)]. The evaporation phenomena were captured with a high-speed camera with a vertical projection of the droplet from top, the projected areas was measured based on the top-view projection with SolidWorks 2018. Though the top-view projection does not imply the proper surface area of whole droplet, as droplet can be stretched towards the bottom part of the spheres, the plots of change in projected areas helped to understand how the droplet size reduced gradually for both whole droplet and liquid islands.

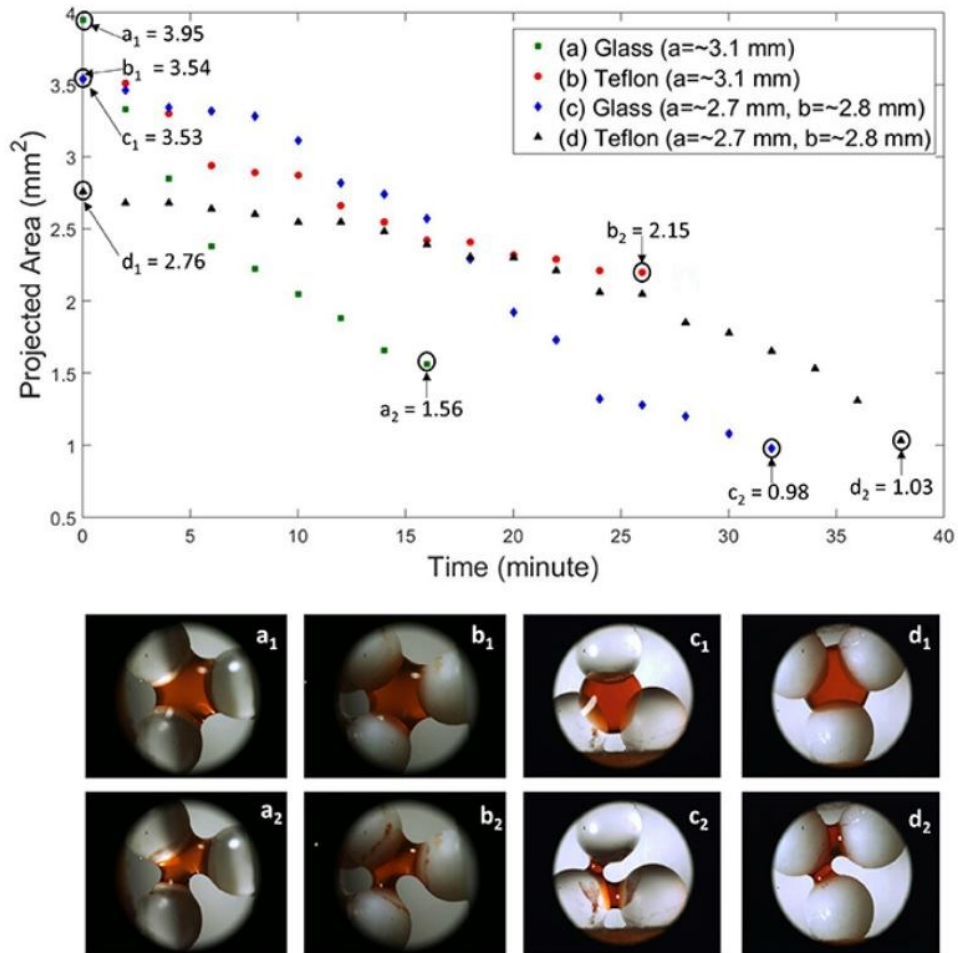


Figure 4.6: Projected areas of whole droplet during evaporation. The plot represents the change in projected area during evaporation and figures a_1, b_1, c_1, d_1 are the initial and a_2, b_2, c_2, d_2 are the final projected areas in glass and Teflon for symmetric (i.e., equilateral) and asymmetric (i.e., isosceles) combination respectively [59]

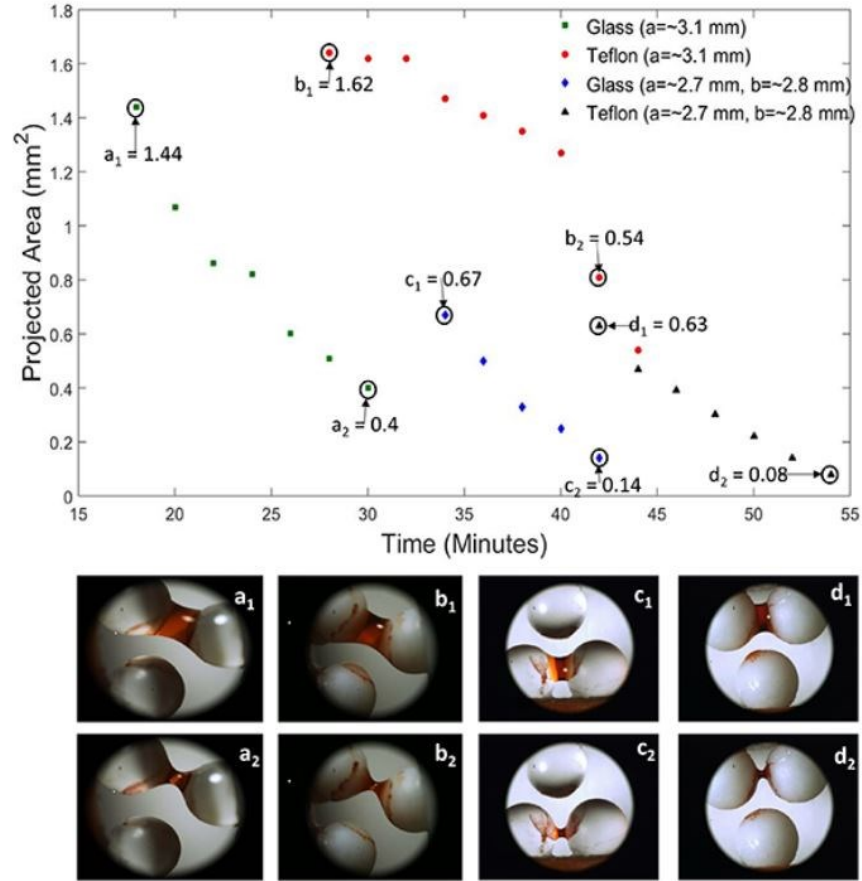


Figure 4.7: Projected areas of liquid island during evaporation. The plot represents the change in projected area during evaporation and figures a_1, b_1, c_1, d_1 are the initial and a_2, b_2, c_2, d_2 are the final projected areas just before rupture in glass and Teflon for symmetric (i.e., equilateral) and asymmetric (i.e., isosceles) combination respectively [59]

4.2.2 Liquid island formation and change in radius of curvature

Similar to previous experiments [experiment 1 (Section 3.1)], the whole droplet broke up and formed a liquid island between two spheres for both glass and Teflon configurations. The process and significance of forming liquid island was discussed in the previous experiment [Section (4.1.2)]. The average time to form liquid islands in glass and Teflon for both combinations are presented in Table 4.3. For both combinations, liquid island formed earlier in glass than Teflon, thereby representing the faster evaporation process in the hydrophilic material. The rupture of

whole droplet and formation of liquid island represents the termination of constant rate of evaporation and beginning of slower rate period.

Table 4.3: Average time to form liquid islands in glass and Teflon pores for both combination

Combination	Liquid Island Formation time (minutes)
Glass (a \approx 3.1 mm), equilateral	19 minutes
Teflon (a \approx 3.1 mm), equilateral	28 minutes
Glass (a \approx 2.8 mm, b \approx 2.7 mm), isosceles	35 minutes
Teflon (a \approx 2.8 mm, b \approx 2.7 mm), isosceles	43 minutes

In previous studies [21, 22], the liquid island deformation was studied under the influence of an imposed thermal gradient, resulting in evaporation in one side and condensation in other, which increased the radius of curvature in one side and decreased it in the other side. However, in an isothermal situation like this study, both sides experience reduction in radius of curvature due to evaporation (Figure 4.3). In this experiment, the radius of curvature of the liquid island was measured and plotted against from the beginning of formation until the rupture. Figure 4.8 represents the change in radius of curvature of the liquid island with time for glass and Teflon for both combinations (equilateral and isosceles). Similar to the previous experiment, both sides of the liquid island experienced reduction in curvature. For the equilateral spacing, the radius decreased at a faster rate in glass than Teflon, whereas in Teflon, the island retained its initial shape for a certain period of time (e.g., \sim 4 minutes) and then it started to decrease. However, in isosceles combination, the radius decreased similarly for both glass and Teflon pores. It took more time (e.g., on average 35 min in glass and 43 min Teflon) to form a liquid island in the isosceles combination and the liquid island lifespan was briefer. The liquid island snapped off or ruptured immediately after 30 minutes in glass and 44 minutes in Teflon for equilateral combination and

for the isosceles configuration, the liquid island snapped off after 42 minutes and 54 minutes for glass and Teflon respectively.

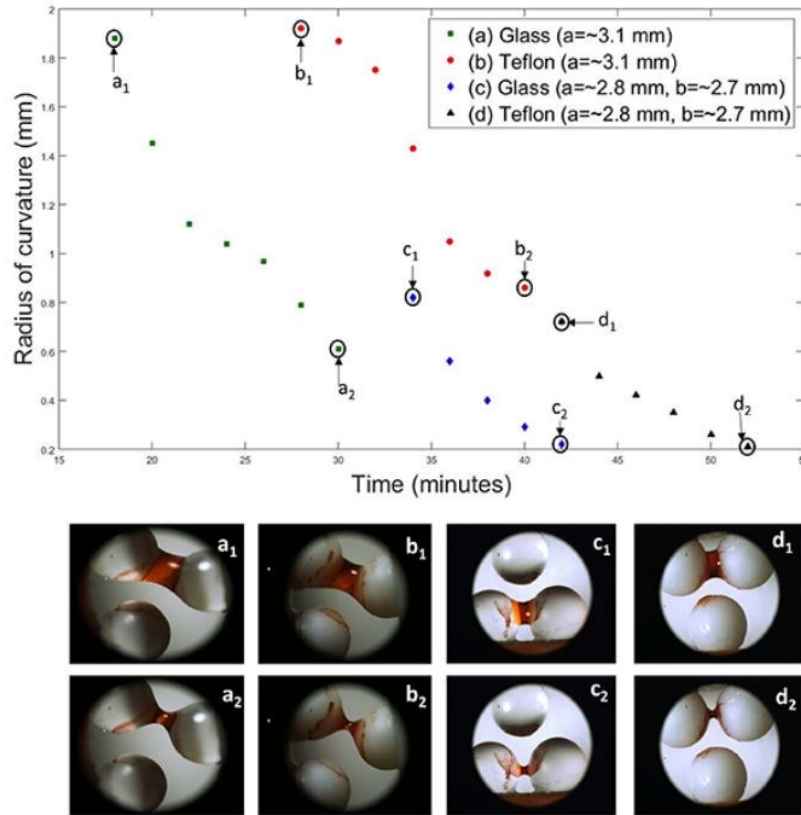


Figure 4.8: Change in radius of curvature of liquid island with time. Glass spheres at (a₁) $t = 18$ min and (a₂) $t = 30$ min and in Teflon (b₁) $t = 28$ min and (b₂) $t = 43$ min (equilateral/symmetric combination). Glass spheres at (c₁) $t = 34$ min and (c₂) $t = 42$ min and Teflon spheres at (d₁) $t = 42$ min and (d₂) $t = 52$ min (isosceles/ asymmetric combination) [59]

4.2.3 Volume and contact angles of liquid island

The contact angle dynamics during evaporation and subsequent changes in the volumes of water held in liquid islands between two spheres were analyzed. The liquid islands' profiles were approximated as circular arcs and imperfect wetting phenomenon (i.e., contact angle is greater than zero) was assumed. The contact angle was estimated from the top view projection of the

whole droplet and Figure 4.9 shows liquid islands formed between two spheres. For imperfect wetting, Pietsch and Rumph [155] derived the following expression for volume calculation:

$$\frac{V}{2\pi} = (R_1^2 + b^2)R_1 \cos(\beta + \delta) - \frac{R_1^3 \cos^3(\beta + \delta)}{3} \quad (4.2)$$

$$- b \left[R_1^2 \cos(\beta + \delta) \sin(\beta + \delta) + R_1^2 \left(\frac{\pi}{2} - \beta - \delta \right) \right]$$

$$- \frac{1}{24} d_p^3 (2 + \cos\beta)(1 - \cos\beta)^2$$

$$R_1 = \frac{d_p(1 - \cos\beta) + a}{2 \cos(\beta + \delta)} \quad (4.3)$$

$$R_2 = \frac{d_p}{2} \sin\beta + R_1 [\sin(\beta + \delta) - 1] \quad (4.4)$$

$$b = R_1 + R_2 \quad (4.5)$$

where, the sphere's diameter is d_p , sphere's separation distance is a , the principal radii of curvature R_1 and R_2 , half filling angle β , contact angle δ and b is the summation of two principal radii of curvature R_1 and R_2 . The volumes of liquid islands were calculated using this model and the contact angles measured in Solidworks 2018. After the rupture of whole droplet, two minutes was spent to the liquid island to stabilize and then contact angles and volume were measured at two minutes' interval.

The change or reduction of liquid islands' volumes with time is presented in Figure 4.10. The estimated initial volumes of liquid island in the glass pores [i.e., 1.71 μL (equilateral) and 0.43 μL (isosceles)] were larger than Teflon [i.e., 1.54 μL (equilateral) and 0.41 μL (isosceles)], and it decreased gradually until the final breakup happened. The glass pores experienced faster decreases in volumes compared to Teflon due to hydrophilic properties and wetting phenomena of glass. Figure 4.11 represents variation of liquid contact angles with liquid island's volumes. For all four

configurations, the contact angle decreased with decreasing volumes. Initial contact angles were slightly higher in Teflon [i.e., 15.91° (equilateral) and 22.08° (isosceles)] than glass [i.e., 15.23° (equilateral) and 15.47° (isosceles)], though the differences were small. Due to equilateral and isosceles center-to-center combinations, the droplets were stretched in both glass and Teflon resulting in lower values of contact angles, δ (Figure 4.9). In the configuration where the particle-to-particle distance was lower (i.e., isosceles), the contact angles were greater due to reduced stretching of the liquid island. For both glass and Teflon, the contact angles decreased gradually with decreasing volumes (Figure 4.11).

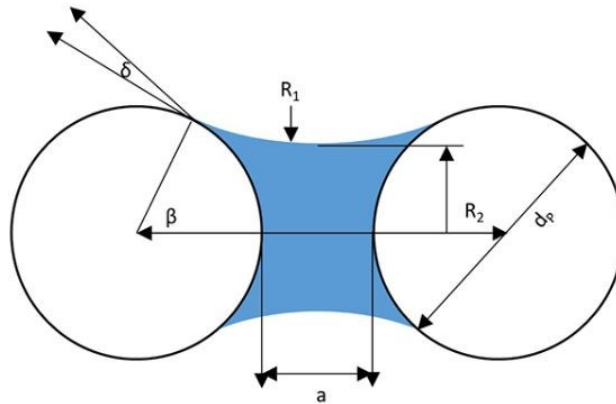


Figure 4.9: Formation of liquid island between two spheres [59]

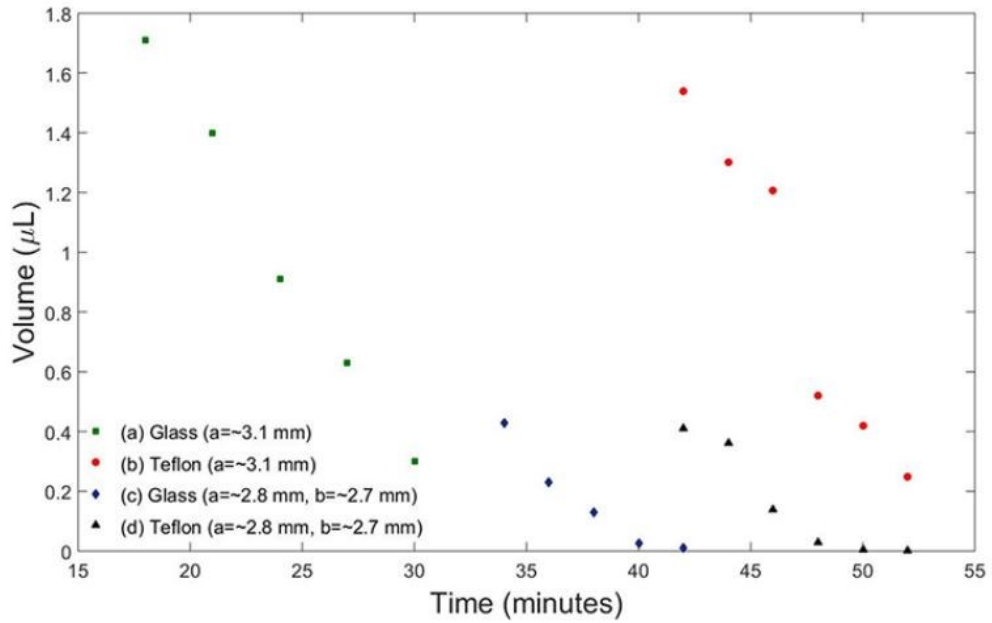


Figure 4.10: Change of volume of liquid island with time from beginning until rupture [59]

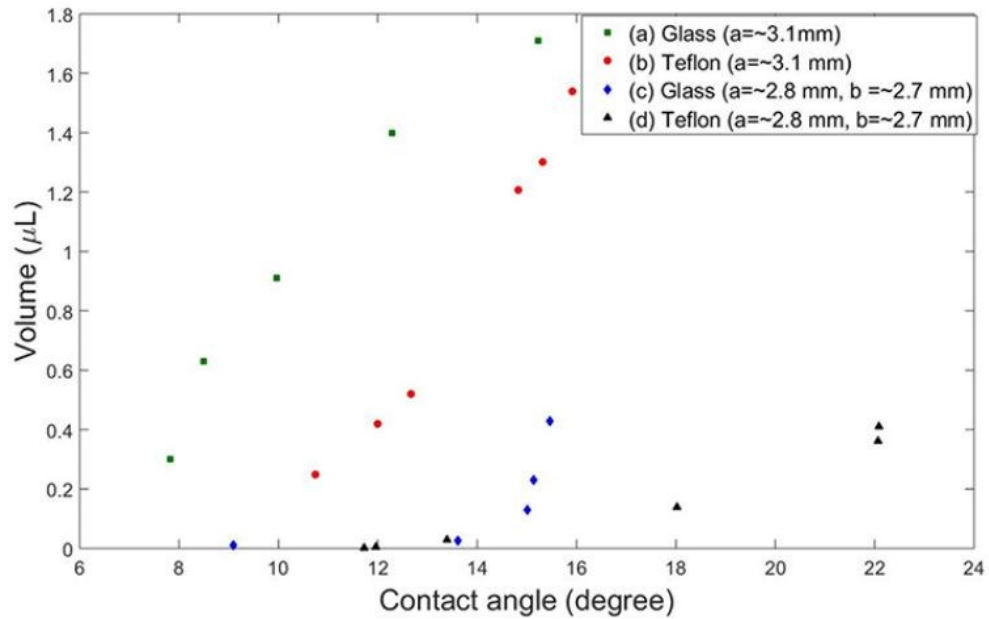


Figure 4.11: Variation of contact angle of liquid island with reduction of volume [59]

4.2.4 Capillary force and rupture of liquid islands

During evaporation, the liquid island deforms its shape and rupture occurs due to evaporative mass loss. Zhu et al., [156] determined the rupture force of liquid island as capillary bridge model (CBM) and evaluated the bridge volume on the basis of separation distance. Lian et al [157] postulated that the total capillary attractive force between two spheres is caused by surface tension and the hydrostatic pressure of the bulk liquid. Pitois et al., [105] used a circular approximation of the bridge profile, determined a simplified expression for the capillary force, and converted it into dimensionless surface energy:

$$\tilde{W} = 2\pi \cos\delta \left[\left(1 + \frac{\delta}{2}\right) (1 - A)\tilde{V}^{\frac{1}{3}} + \sqrt{\frac{2\tilde{V}}{n}} \right] \quad (4.6)$$

where, $A = \sqrt{(1 + 2\tilde{V})^{\frac{1}{3}}/\pi(1 + \delta/2)^2}$, δ is the contact angle in radians, \tilde{W} is rupture energy, $\tilde{V} = \frac{V}{R^3}$, is the dimensionless liquid island's volume. The rupture energy model by Simons et al., [107] was derived by the integration of total liquid island force:

$$F = \pi\gamma R (1 + X\tan\beta - X\sec\beta) \frac{X\tan\beta}{X\sec\beta - 1} \quad (4.7)$$

where, R is sphere's radius, γ is liquid surface tension, $X = 1 + a^*$, where a^* is half separation distance and β is half filling angle. Willet et al., [110] derived a less complex CBM (Capillary Bridge Model) for equal sized particles expressed by the following equation:

$$F_{cap} = \frac{2\pi R\gamma\cos\delta}{1 + 2.1(S^+) + 10(S^+)^2} \quad (4.8)$$

where

$$S^+ = \frac{a}{2\sqrt{\frac{V}{R}}} \quad (4.9)$$

where, S^+ is dimensionless half separation distance, a is distance between the spheres, V is liquid island's volume and R is radius of the sphere.

Rabinovich et al., [106] proposed the following expression which is based on combined experimental and numerical analysis. First, the “embracing angle”, α is evaluated:

$$\alpha = \sqrt{\frac{a}{R} \cdot (-1 + \sqrt{1 + \frac{2V}{\pi R a^2}})} \quad (4.10)$$

then the immersion distance $d_{sp/sp}$ was evaluated using the following expression:

$$d_{sp/sp} = \frac{a}{2} [-1 + \sqrt{1 + \frac{2V}{\pi R a^2}}]. \quad (4.11)$$

finally, F_{cap} was predicted with:

$$F_{cap} = -\frac{2\pi R \gamma \cos \delta}{1 + \left[\frac{a}{2d_{sp}} \right]} - 2\pi \gamma R \sin \alpha \sin (\delta + \alpha) \quad (4.12)$$

Lambert et al., [116] modified the Rabinovich et al., [106] model and deduced the following expression:

$$F_{cap} = -\frac{2\pi R \gamma \cos \delta}{1 + \left[\frac{a}{2d_{sp}} \right]} \quad (4.13)$$

In this dissertation, the models of Willet et al., [110] , Rabinovich et al., [106] and Lambert et al., [116] were used to determine the capillary/rupture strengths of the liquid islands. The sphere's diameter was $d_p = 2.38$ mm, surface tension of water, $\gamma = 72.75$ mN/m (at 22° C), principal radii of curvature R_1 and R_2 were in mm, half filling angle β and contact angle δ were in degree and volumes, v , were in μL . For first combination (i.e., equilateral), the rupture strength was measured at three minutes' and for the second combination (i.e., isosceles), it was calculated

at two minutes' interval after formation of liquid island. Principle radii of curvature R_1 and R_2 , half filling angle β and contact angle δ were measured continuously using SolidWorks 2018 from the processed images. Volume v was derived using equation (4.2) at two minute's time interval and equations [(4.8), (4.12), (4.13)] were used to measure rupture strength/ capillary force according to Willet et al., [110], Rabinovich et al., [106] and Lambert's [116] models, respectively.

Figure 4.12 represents the change and reduction in rupture strength with time for all four combinations. The calculated rupture strengths are almost similar for all three models. There was slight difference between the Willet [110] and other two models, but the Rabinovich [106] and Lambert [116] models overlapped in every single data point. The initial rupture strength of liquid island in Teflon pores [i.e., $\sim 177 \mu\text{N}$ (equilateral) and $\sim 215 \mu\text{N}$ (isosceles)] were slightly larger than glass [i.e., $\sim 170 \mu\text{N}$ (equilateral) and $\sim 212 \mu\text{N}$ (isosceles)] and the rupture strength decreased slowly with time. For both combinations, the initial rupture strength was larger with smaller pore size (i.e., isosceles/asymmetric combination). This phenomenon was explained in the research of Gladky and Schwarze [102] where the rupture strength of a liquid island continuously decreased with increasing particle distance i.e., larger rupture strength for smaller distance. In that research, rupture strength of the liquid island was evaluated using Willet [110], Rabinovich [106] and Lambert [116] models and the distances between the spheres were changed continuously to evaluate the effect of spheres' distance on liquid island rupture strength.

The final rupture strengths – just before rupture – were similar for glass and Teflon for all four combinations. During evaporation, water tends to move from higher energy position to lower energy, and that phenomena were observed in the plot (Figure 4.12). The rupture strength for all four combinations decreased gradually with time and the strength reached its lowest value just before breakup of the liquid island.

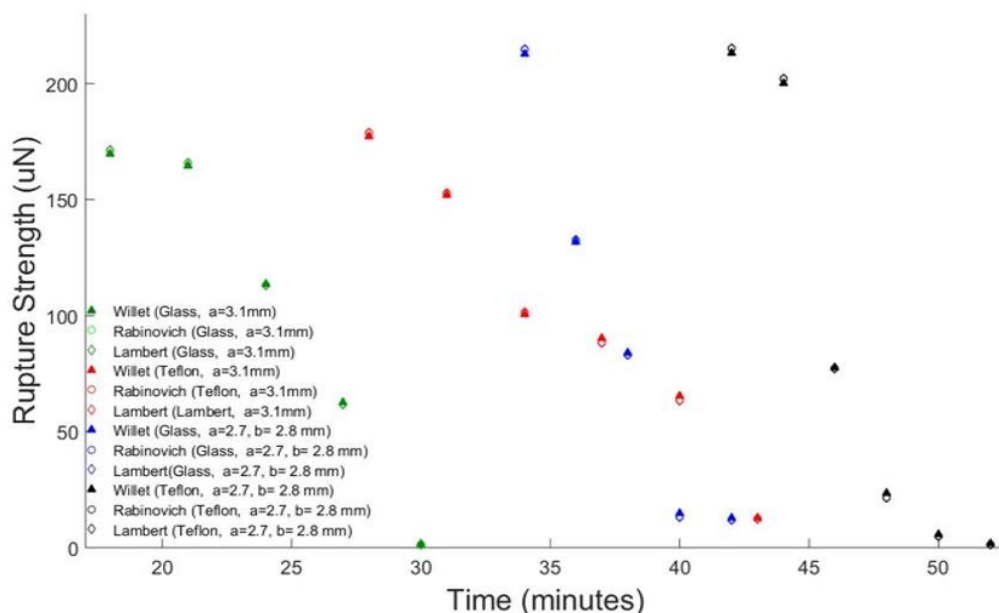


Figure 4.12: Variation of rupture strength of liquid island formed between glass or Teflon spheres for both combinations with time. Willet et al., [110] , Rabinovich et al., [106] and Lambert et al., [116] models were used to calculate the rupture strength [59]

4.3 Experiment 3 – Contact line pinning and depinning prior to rupture of an evaporating droplet⁸

In this experiment, 4- μ L water droplets were evaporated from a simulated soil pore constructed from three hydrophilic glass or hydrophobic Teflon spheres of same sizes (i.e., 2.38 mm). The center-to-center distances of the spheres were kept constant at 3.1 mm. Two different relative humidities were included in this study (i.e., 30% RH and 75% RH) while the temperature was consistent at 20 °C (section 3.1). In this study, the evaporation time, contact line pinning and

⁸ Figures and parts of section originally published in “Chakraborty, P. P., & Derby, M. M. (2020, July). Contact Line Pinning and Depinning Prior to Rupture of an Evaporating Droplet in a Simulated Soil Pore. In *International Conference on Nanochannels, Microchannels, and Minichannels* (Vol. 83693, p. V001T06A003). American Society of Mechanical Engineers.”

depinning, evaporating projected area and deformation of radius of curvature of the liquid-vapor interface prior to rupture were analyzed.

4.3.1 Evaporation time

Table 4.4 represents the evaporation time of 4- μ L water droplets at 20° C, 30% and 75% RH from both glass and Teflon pores. Each experiment was replicated three times. The evaporation rate was faster in glass than Teflon at both relative humidities. Evaporation continued until approximately 19 and 49 minutes from glass pores at 30% and 75% RH, compared to approximately 24 and 52 from Teflon pores at 30% and 75% RH, respectively.

While evaporating from glass and Teflon pores, the droplets size reduced due to evaporative mass loss and the droplet broke up and created a liquid island between two spheres to achieve minimum surface energy. According to Philip and De Vries [21, 22], liquid island formation between two particles is an important phenomenon in soil-water dynamics. Similar phenomena were also noticed in experiment 1 and experiment 2 where the whole droplet ruptured and formed a liquid island between two spheres. Figure 4.13 represents the formation and propagation of liquid island in glass and Teflon pore at 75% RH. Figure 4.13 (a and e) exhibit the final state of the whole droplet just before rupture. Eventually, the liquid island also decreased its size by reducing the radius of curvature from both sides due to evaporation and rupture of the liquid island denoted the end of the droplet evaporation process.

Table 4.4: Evaporation time for 4 μ L water droplet at 30% and 75% RH from hydrophilic (glass) and hydrophobic (Teflon) pores

	Evaporation time (minutes)			
	RH = 30%, T = 20° C		RH = 75%, T = 20° C	
Replication number	Glass	Teflon	Glass	Teflon
1	18	24	49	51

2	18	24	49	53
3	20	24	49	52
Average time	19	24	49	52

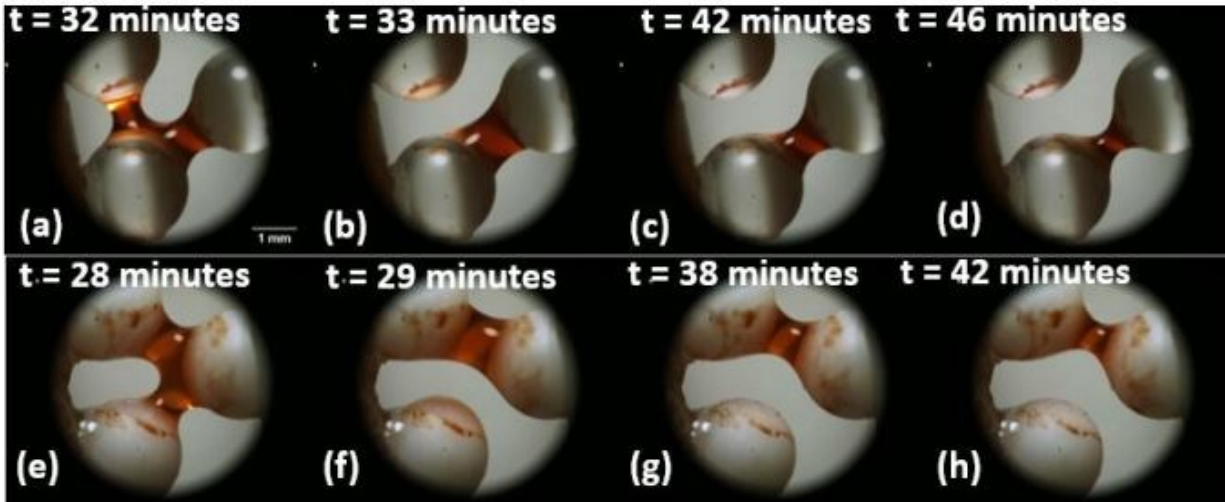


Figure 4.13: Liquid island formation in two spheres. (a-d) and (e-h) represent liquid island formation and propagation from glass and Teflon respectively at 75% RH. (a) and (e) represent the final state of whole droplet just before rupture [30]

4.3.2 Contact line pinning and depinning

During evaporation, the water droplets created three solid-liquid-vapor contact lines with the glass and Teflon spheres, and the contact areas changed in size and shape along with contact lines. The contact lengths were estimated using SolidWorks 2018. Since the pinned and depinned contact lines were not similar for all three replications, they were specified for all three replications visually. At first, the pinned contact lines were determined and then the depinned ones were pointed out in a clockwise manner.

Figure 4.14 and Figure 4.15 represent the change in contact lengths for glass and Teflon pores at 30% and 75% RH, respectively. The solid-liquid-vapor contact lines were measured at two minutes' time interval from the beginning of evaporation until the breakup of whole droplet

for both glass and Teflon. In glass pores, solid-liquid-vapor contact lines were found pinned (i.e., the length did not change significantly) in one sphere which was marked as 'P' and were depinned (i.e., the contact length decreased gradually from its initial state) in the rest two spheres for all three replications and they were marked as 'D1' and 'D2'. The pinned sphere was specified and then the two depinned spheres were determined clockwise.

In Teflon pores, all the three solid-liquid-vapor contact lines were found moving or depinned (i.e., the contact lengths gradually decreased from the beginning until the breakup of whole droplet). The sphere that experienced the sharpest decrease in contact length were specified as 'D1' and then the rest of the spheres were marked as 'D2' and 'D3' in a clockwise manner. Rupture occurred in that sphere where the solid-liquid-vapor contact length was lowest before breakup.

In glass pores, at 30% RH (Figure 4.14) and 75% RH (Figure 4.15), the pinned contact lengths did not change from the beginning of evaporation until the breakup (i.e., ~2 mm for 30% RH and ~ 2.1 mm for 75% RH) and the remaining two contact lengths decreased gradually for all three replications. In Teflon pores, at both relative humidities (i.e., 30% and 75% RH), all the three solid-liquid-vapor contact lengths (D1, D2 and D3) decreased gradually from the beginning until the rupture of whole droplet. These phenomena are consistent with the findings of study of sessile droplet on flat hydrophilic or hydrophobic flat surface, wherein on hydrophilic surfaces the droplets experienced a constant contact radius (CCR) evaporation mode with no change in solid-liquid-vapor contact length (i.e., pinned [35, 38, 39, 57, 89]) and on hydrophobic surfaces, the contact lengths decreased but the contact angle remained same (i.e., constant contact angle (CCA) mode or depinned phenomenon [40, 82, 90-93]).

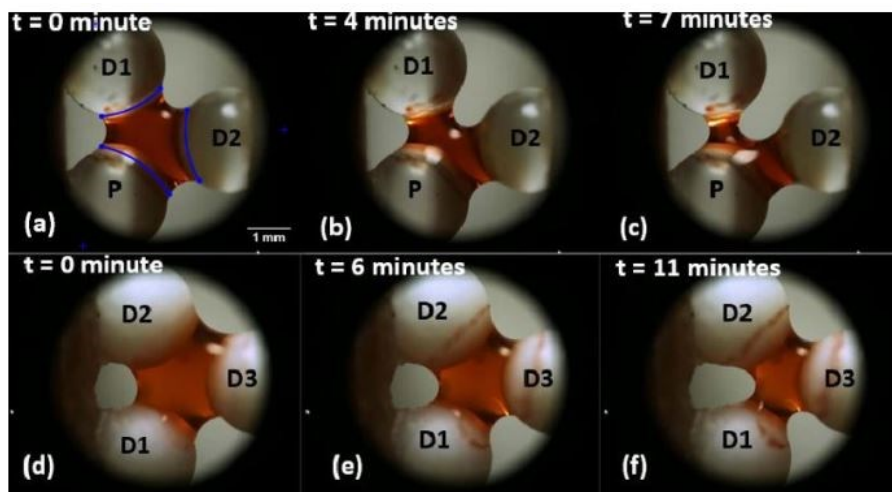
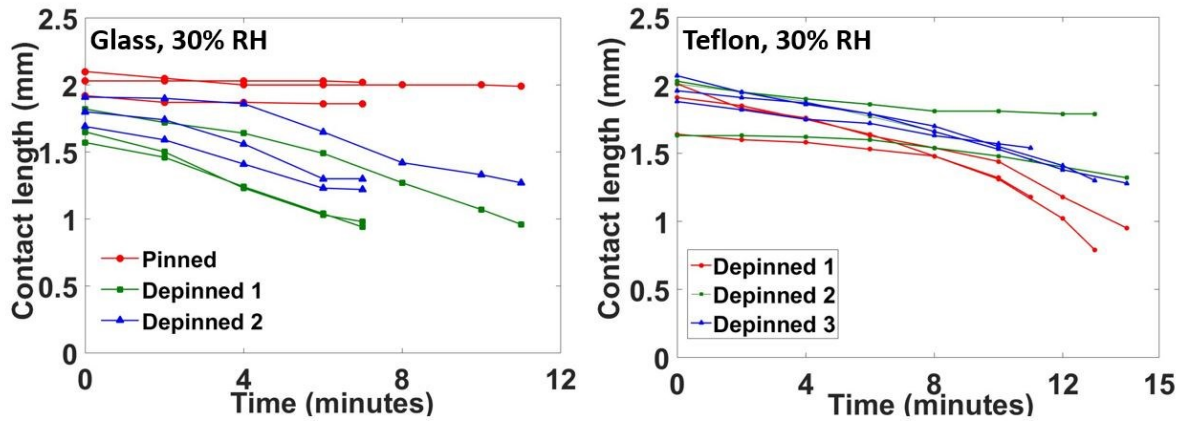
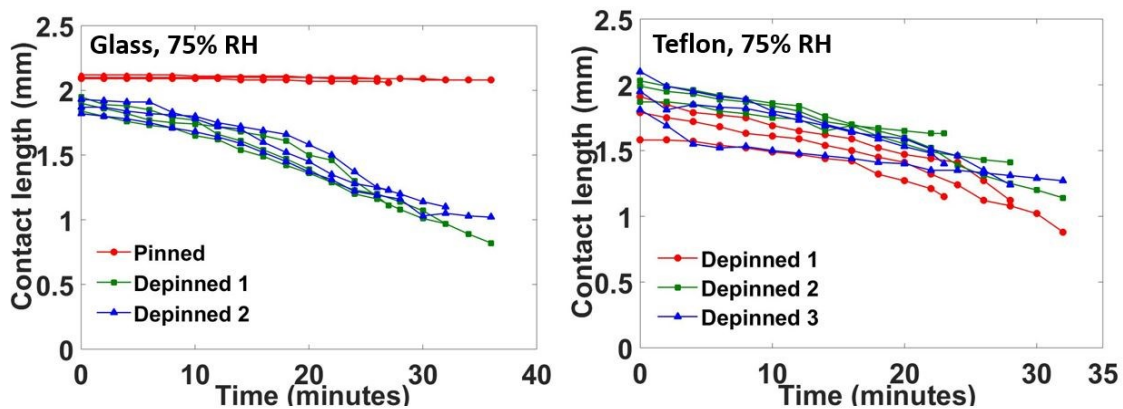


Figure 4.14: Contact line pinning and depinning of glass and Teflon at 30% RH. The plots represent the change in contact length in glass and Teflon for three spheres. a, b, c and d, e, f represent the contact line pinning and depinning in glass and Teflon pores respectively. P, D1, D2 and D2 represent pinned, depinned 1, depinned 2 and depinned 3 contact lines [30]



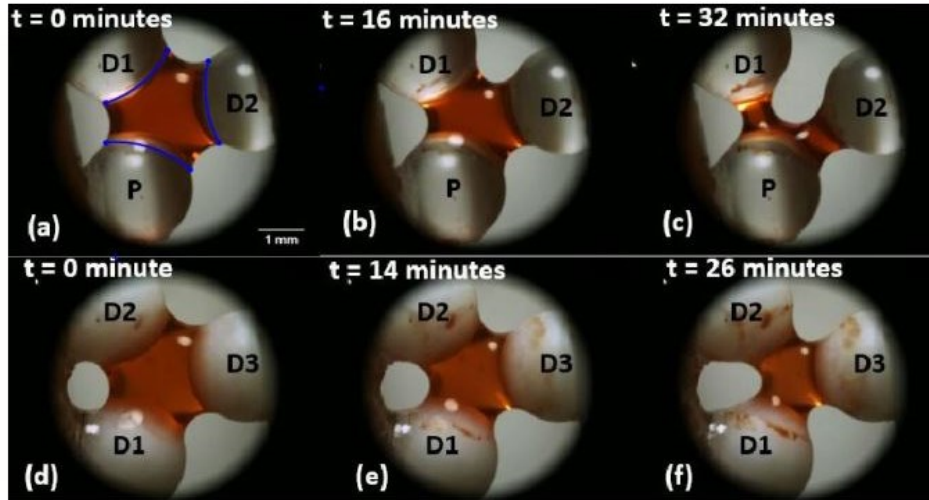


Figure 4.15: Contact line pinning and depinning of glass and Teflon at 75% RH. The plots represent the change in contact length in glass and Teflon for three spheres. a, b, c and d, e, f represent the contact line pinning and depinning in glass and Teflon pores respectively. P, D1, D2 and D2 represent pinned, depinned 1, depinned 2 and depinned 3 contact lines [30]

4.3.3 Change in projected areas

The evaporation phenomena were captured with a high-speed camera which was located vertically and captured the top-view projection of the droplet evaporation (Figure 3.1). The projected areas were measured based on the areas of whole droplet from the top-view images. Figure 4.16 (a and c) represent the actual projected areas of whole droplets from the top projection. SolidWorks 2018 was used to redraw the droplet in actual pixel size and the “area measurement” tool was used to measure the projected areas of the droplet at two minutes’ interval. The plot (Figure 4.16) represents the change in projected areas of the evaporating droplet from the beginning until the rupture of whole droplet from glass and Teflon pores at 30% and 75% RH. The initial projected areas were bit larger in Teflon pore than glass for all three replications, and the projected areas decreased gradually with time for both glass and Teflon. Though the rates of decrease in projected areas are almost similar for glass and Teflon, at 30% RH, the projected areas decreased more sharply than at 75% RH.

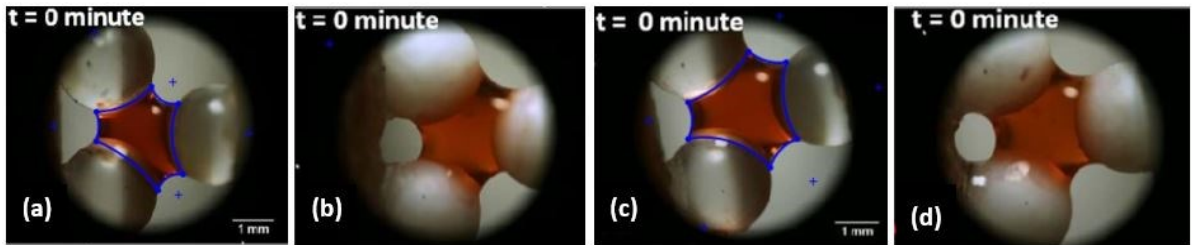
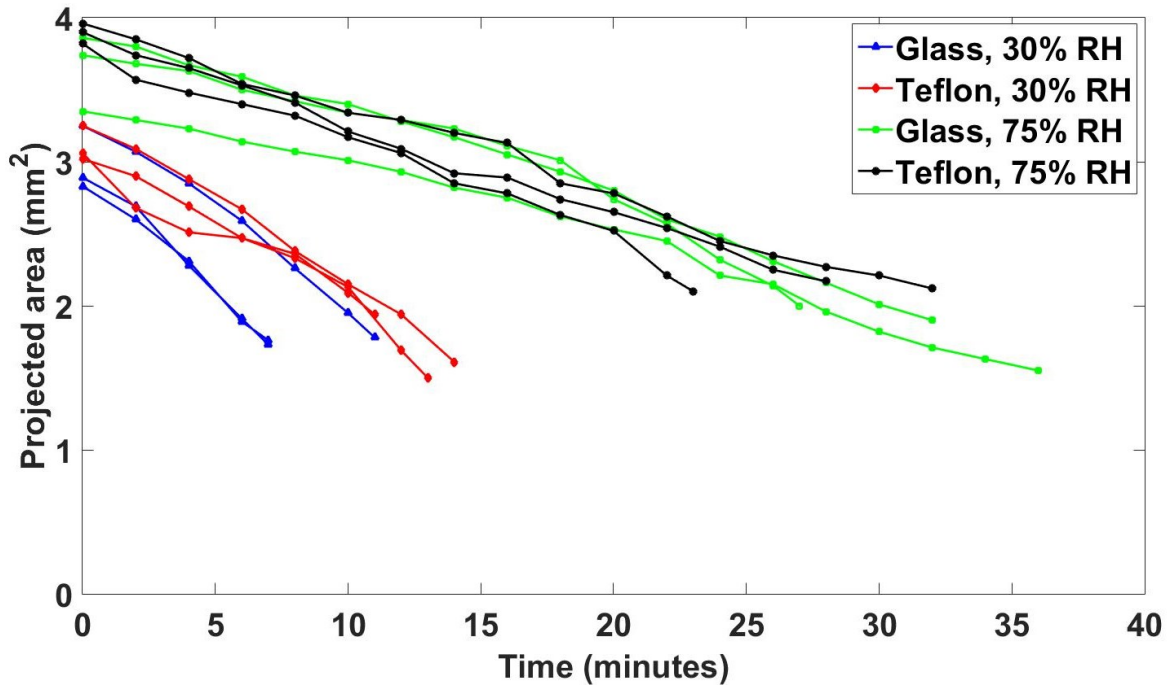


Figure 4.16: Change in projected area for glass and Teflon during evaporation at 30% and 75% RH. (a) and (c) represent the initial projected areas in glass at 30% and 75% RH. (b) and (d) represent the initial projected areas in Teflon at 30% and 75% RH respectively [30]

4.3.4 Change in radius of curvature of the liquid-vapor interface

During evaporation, along with the solid-liquid-vapor contact lines, the droplet created three liquid-vapor interfaces and the rupture of whole droplets were associated with the pressure difference across those interfaces. Contact line pinning and depinning phenomena resulted in significant changes in liquid-vapor interfaces during evaporation. Urso et al. [114] postulated that the pressure difference across liquid-vapor interface in a capillary liquid bridge is governed by

Laplace-Young equation, when the gravitational force is negligible and can be expressed as following:

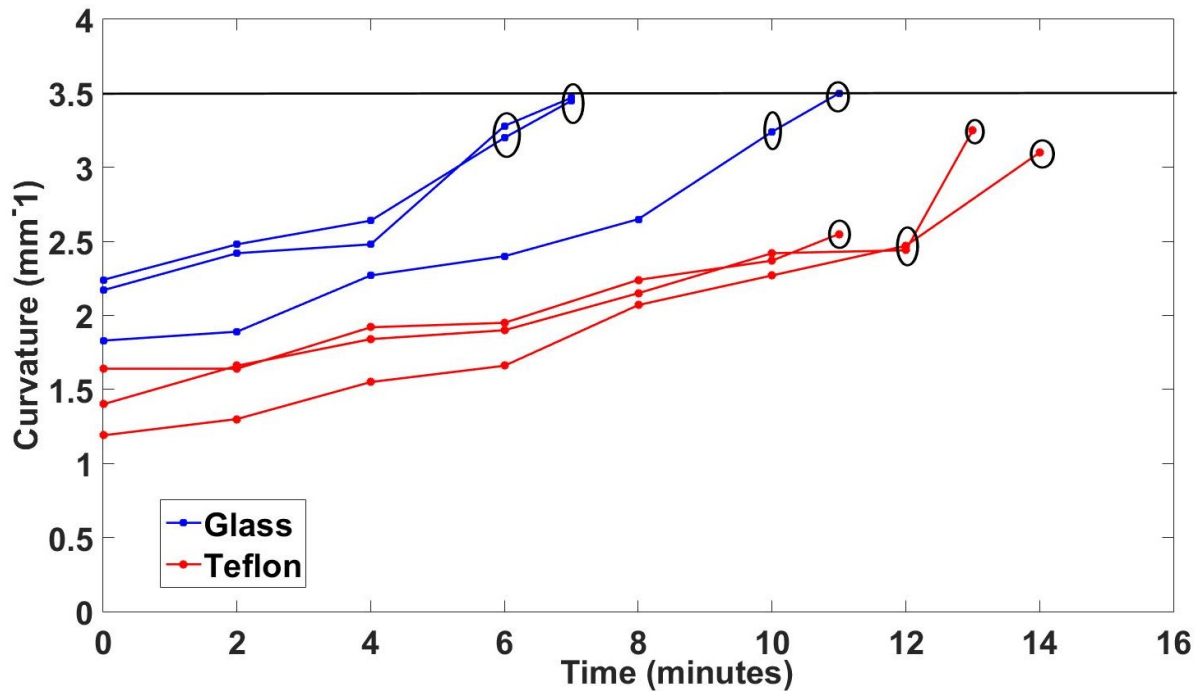
$$\kappa = \frac{\Delta p}{\gamma} \quad (4.14)$$

where κ is the curvature of the meniscus profile, γ is interfacial surface tension and Δp is pressure difference across liquid-vapor interface. The equation implies a proportional relationship between curvature and pressure difference across the liquid-vapor interface.

The stretched droplets among three glass or Teflon spheres created three liquid-vapor interfaces and, upon observation, one interface changed significantly than the other two, resulting in rupture of whole droplet across that interface. The particular liquid-vapor interface that deformed most was identified for all three replications for both glass and Teflon pores. Subsequently, the curvature of that liquid-vapor interface was measured at two minutes' interval from the beginning until the rupture of whole droplets with the SolidWorks 2018 curvature tool. Initially for both glass and Teflon pores, the liquid-vapor interface looked like an arc with constant curvature, but it transformed into elliptical or parabolic shape approximately 4-6 minutes prior to rupture. For elliptical or parabolic shapes, the maximum curvature was measured, and all the curvatures were plotted against time at two minutes' interval from the beginning until the rupture of whole droplet (Figure 4.17 and Figure 4.18).

Figure 4.17 and Figure 4.18 show that the curvature of the liquid vapor interfaces increased from the beginning until the breakup of whole droplet at both 30% and 75% RH for both glass and Teflon pores. Initially, the interface looked like an arc with constant curvature [Figure 4.17 and Figure 4.18 (a, b, d, e)] but it transformed into elliptical or parabolic shape just before rupture [Figure 4.17 and Figure 4.18 (c, f)], and the maximum curvature was measured in that case. The black elliptical marks on the plot represent the time frame where the interface started to transform

into ellipse or parabola from a regular arc approximately 4-6 minutes prior to rupture of whole droplet. The maximum curvature was approximately 3.5 mm^{-1} and $3.2\text{-}4 \text{ mm}^{-1}$ for glass and 3 mm^{-1} and $2.7\text{-}3.1 \text{ mm}^{-1}$ for Teflon pores at 30% and 75% RH, respectively, just before rupture. For both relative humidities, the ultimate curvature immediately before rupture was found to be larger in glass than Teflon pores. As the pressure difference across the liquid-vapor interface is directly proportional to the curvature, greater pressure differences were required to initiate rupture of whole droplet in glass than Teflon across liquid-vapor interface.



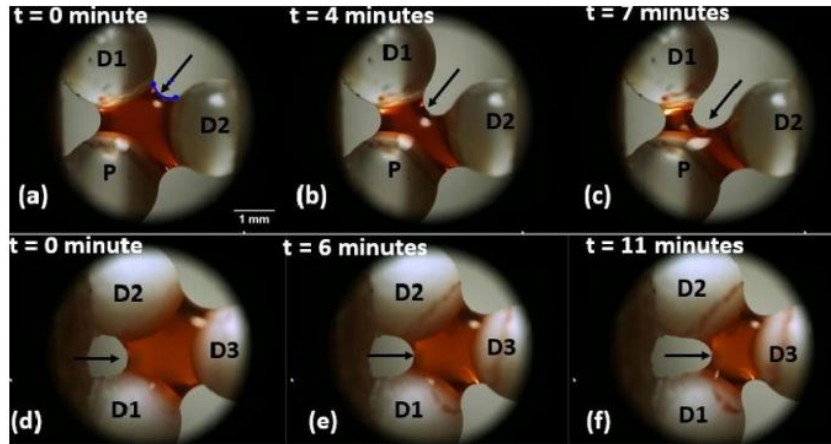
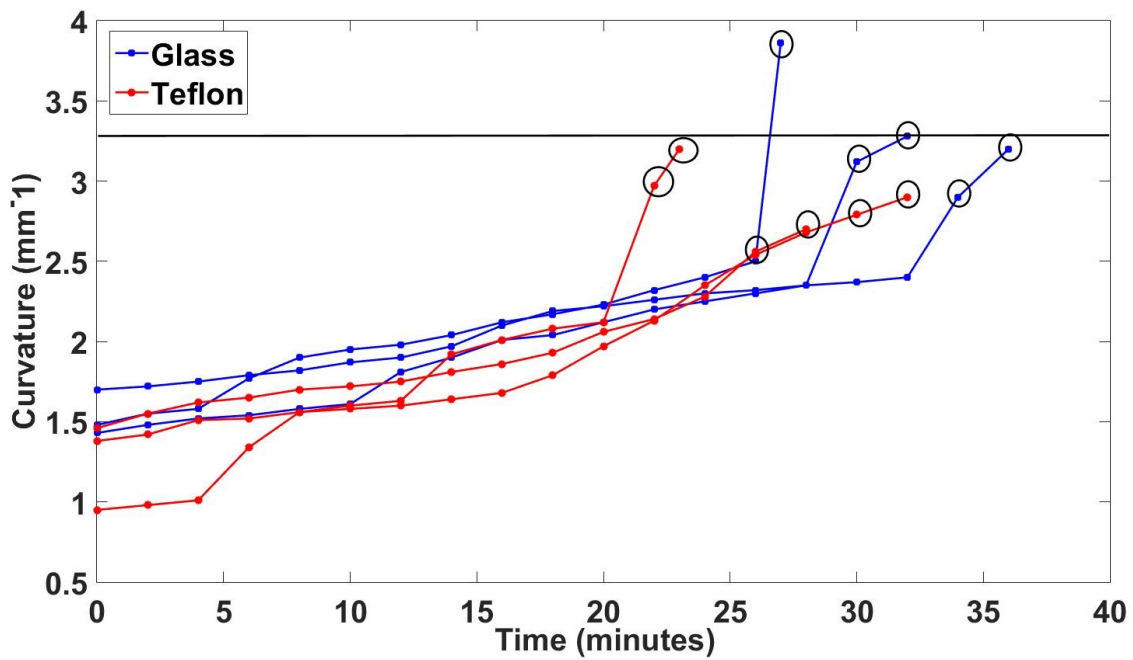
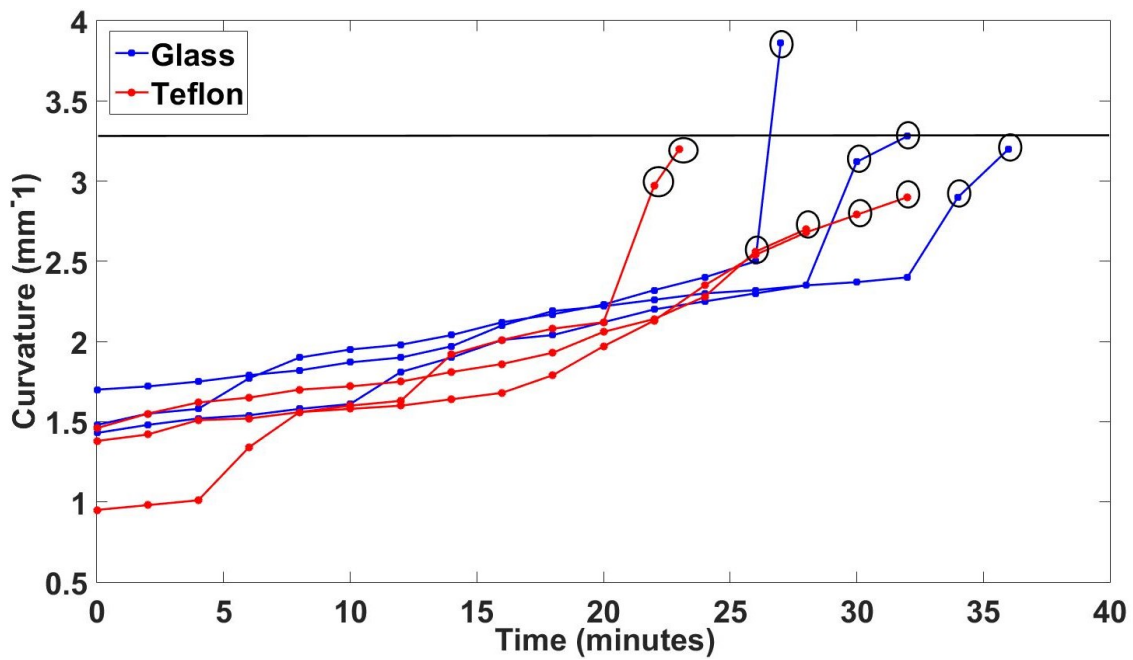
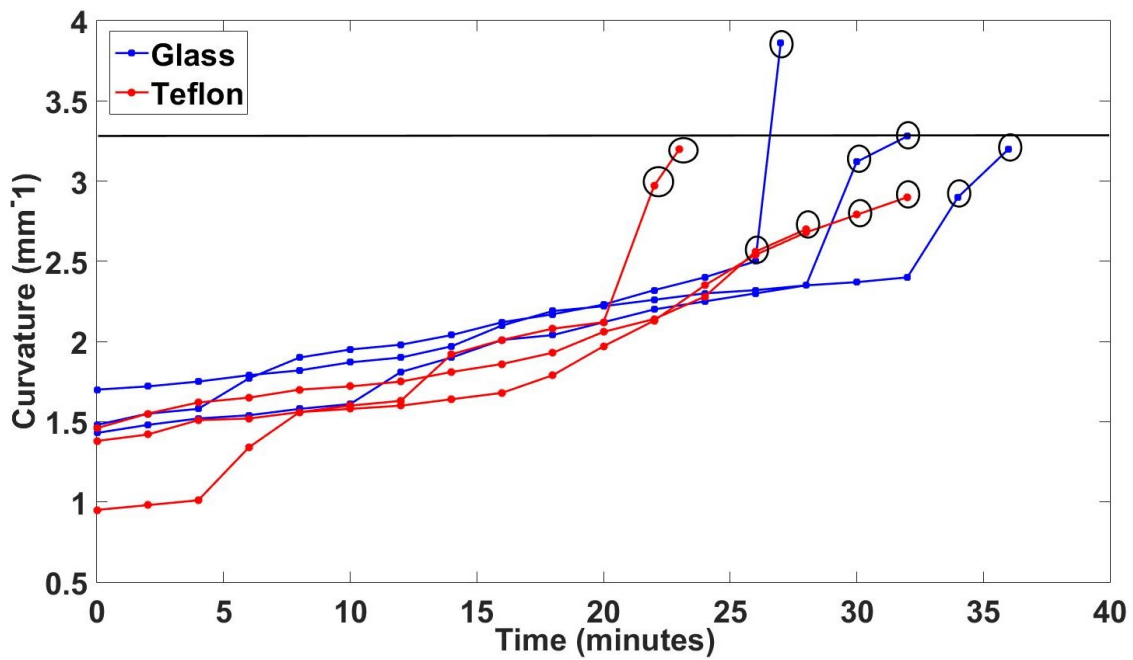
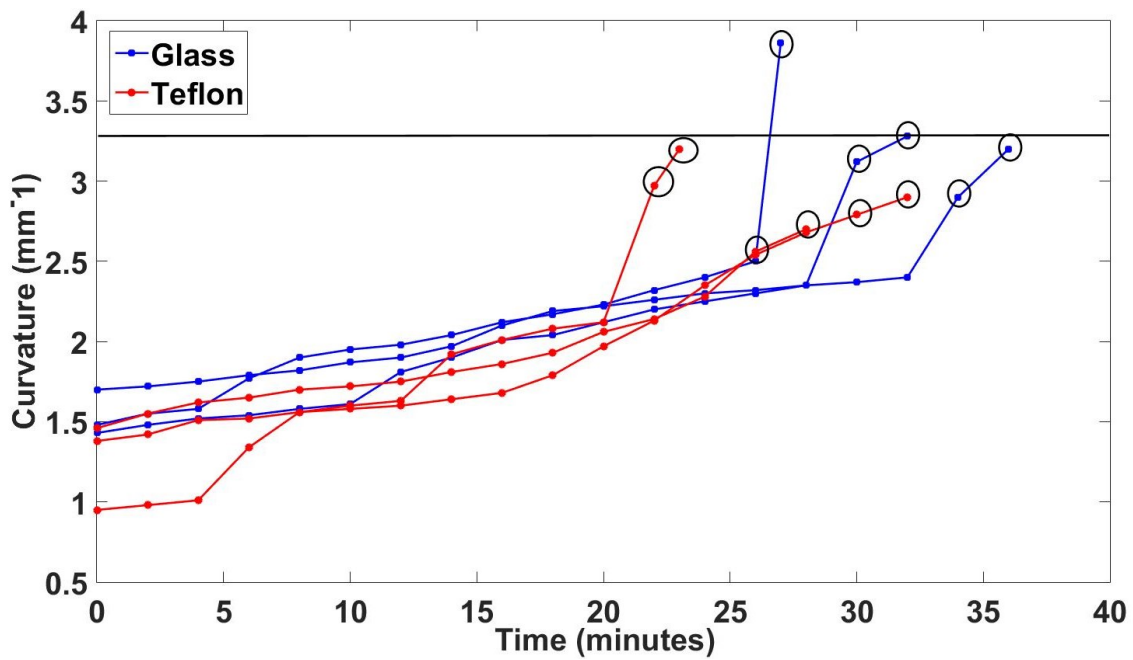


Figure 4.17: Change of curvature in liquid-vapor interface at 30% RH. (a), (b), (c) and (d), (e), (f) represent the curvature change (arrow sign) in glass and Teflon pores respectively. The black elliptical marks on the plot represent the transformation of liquid-vapor interface from arc to parabolic shape [30]



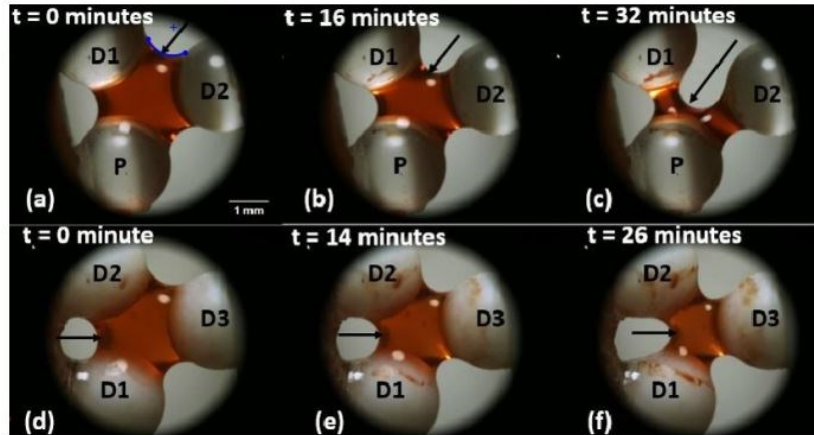


Figure 4.18: Change of curvature in liquid-vapor interface at 75% RH. (a), (b), (c) and (d), (e), (f) represent the curvature change (arrow sign) in glass and Teflon pores respectively. The black elliptical marks on the plot represent the transformation of liquid-vapor interface from arc to parabolic shape [30]

4.4 Uncertainty analysis

In the experiments of evaporation from single pores (experiment 1, 2 and 3), significant droplet parameters including the radius of curvature, projected areas, contact angle, principal radius of curvature were measured using SolidWorks 2018. Initially, the images were extracted with PFV (Photron FastCAM Viewer), and then were exported to SolidWorks with actual pixel size (Height by width ratio). Subsequently, the respective parameters were measured four times per experiment to evaluate uncertainties and standard deviation. Table 4.5, Table 4.6, and Table 4.7 represent the calculations of standard deviation while measuring different droplet parameters with SolidWorks 2018 for experiments 1, 2, and 3. The standard deviation ranged from ± 0.005 to ± 0.075 while measuring certain parameters.

Table 4.5: Measuring radii of curvature at 45% RH for glass and Teflon in experiment 1

Measurement	Glass		Teflon	
	Radius of curvature 1, (mm)	Radius of curvature 2, (mm)	Radius of curvature 1, (mm)	Radius of curvature 2, (mm)
1	1.52	1.53	1.57	1.6
2	1.51	1.52	1.58	1.61

3	1.51	1.5	1.57	1.62
4	1.52	1.52	1.58	1.6
Standard deviation	±0.005	±0.01	±0.005	±0.009

Table 4.6: Standard deviation in measuring contact angle and principal radius of curvature for glass at equilateral combination in experiment 2

	Contact Angle, δ (degree)				Principal Radius of Curvature, R_l (mm)			
1	15.23	12.28	9.97	8.5	1.88	1.3	1.04	0.83
2	15.3	12.4	9.9	8.33	1.85	1.33	1.02	0.82
3	15.28	12.36	9.85	8.36	1.88	1.35	1.03	0.82
4	15.32	12.44	9.92	8.42	1.87	1.33	1.04	0.81
Standard Deviation	±0.03	±0.06	±0.05	±0.075	±0.01	±0.02	±0.01	±0.008

Table 4.7: Standard deviation in measuring the solid-liquid-vapor contact lengths (pinned, depinned 1 and depinned 2) and projected areas for glass at 30% RH

	Pinned, (mm)	Depinned 1 (mm)	Depinned 2 (mm)	Projected area (mm ²)
1	2.09	1.9	1.87	3.74
2	2.08	1.88	1.86	3.79
3	2.06	1.91	1.88	3.76
4	2.08	1.9	1.9	3.8
Standard Deviation	±0.012	±0.012	±0.017	±0.027

Chapter 5 - Evaporation from porous columns

This experiment was divided into two parts. In first part, evaporation of water was studied from a small hydrophilic porous column made with glass sphere. In the second part, water was evaporated from two hydrophilic and hydrophobic porous column to compare the effect of wettability on evaporation.

5.1 Liquid transport during evaporation from small hydrophilic soil columns⁹

In this study, 5.5 mL of deionized water was evaporated from a hydrophilic soil column created with ~1720 borosilicate glass spheres (2-mm-diameter) with the action of 1500 W/m² heat flux from top with a solar simulator to mimic the effects of sun on evaporation (Figure 3.4). The experiment was replicated three times and x-ray images were captured to observe liquid transport and drying front propagation during evaporation. The evaporative mass loss was recorded at five minutes' interval to differentiate evaporation progressions. The results of evaporation time, transient mass measurements, drying front propagation and evaporation stages will discussed in the following sections.

5.1.1 Evaporation time

A total of 5.5 mL of water was evaporated from the simulated hydrophilic soil column at $T = 22^{\circ} \text{C}$ and $\text{RH} = 35 \pm 2\%$ with constant heat flux of 1500 W/m² from the top. The experiment was replicated three times and each time 5 mL (i.e., 91% of total water) was evaporated from the soil column. Table 5.1 represents the time to evaporate 5 mL water from hydrophilic soil column for each replication. The average evaporation time was 2840 minutes (i.e., 47.3 hours).

⁹ Figures and parts of section originally published in “Chakraborty, P. P., Ross, M., Bindra, H., & Derby, M. M. (2019, July). Liquid Transport During Evaporation of Water From a Small Simulated Soil Column. In *Heat Transfer Summer Conference* (Vol. 59315). American Society of Mechanical Engineers”

Table 5.1: Time to evaporate 5 mL of water from a simulated hydrophilic soil column

Replication number	Evaporation time (minutes)
1	2850
2	2790
3	2880
Average	2840

5.1.2 Transient mass measurement and evaporation stages

In this experiment, 5 mL of water was evaporated from the 2-cm-diameter, 3-cm-tall beaker filled with borosilicate glass spheres (2-mm-diameter). Initially, the level of water was slightly above (1 mm) the level of spheres. Due to applied heat flux (1500 W/m²), the evaporation was accelerated compared to field situations. The evaporative loss was recorded at five minutes' time interval for all three replications and were plotted against time. Figure 5.1 represents the evaporative mass loss of water for all three replications and good repeatability was observed.

Figure 5.2 shows the averaged slope of mass during evaporation. The average slopes (dm/dt) were calculated at each time using seven mass/time data points (i.e., averaged over a time interval of 30 minutes):

$$\frac{\overline{dm}}{dt} = \frac{\sum_{i=-3}^{i=3} (t_i - \bar{t})(m_i - \bar{m})}{(t_i - \bar{t})^2} \quad (5.1)$$

where, m and t are mass of water and time, \bar{m} and \bar{t} are the averaged quantities over the half-hour interval, and i is the index. The evaporation process was slow and the maximum mass loss over a 30 minutes' period was 0.2 g. According to Figure 5.2, the steepest slope was observed from the beginning until 480-625 minutes for all three replications, with average of -0.005 g/min of mass

loss. Then the evaporation rate was stabilized until 1300th minute with -0.002 g/min mass loss. A transition occurred after that time period and after 1800th minute the evaporation rate was slower with -0.0004 g/min mass loss.

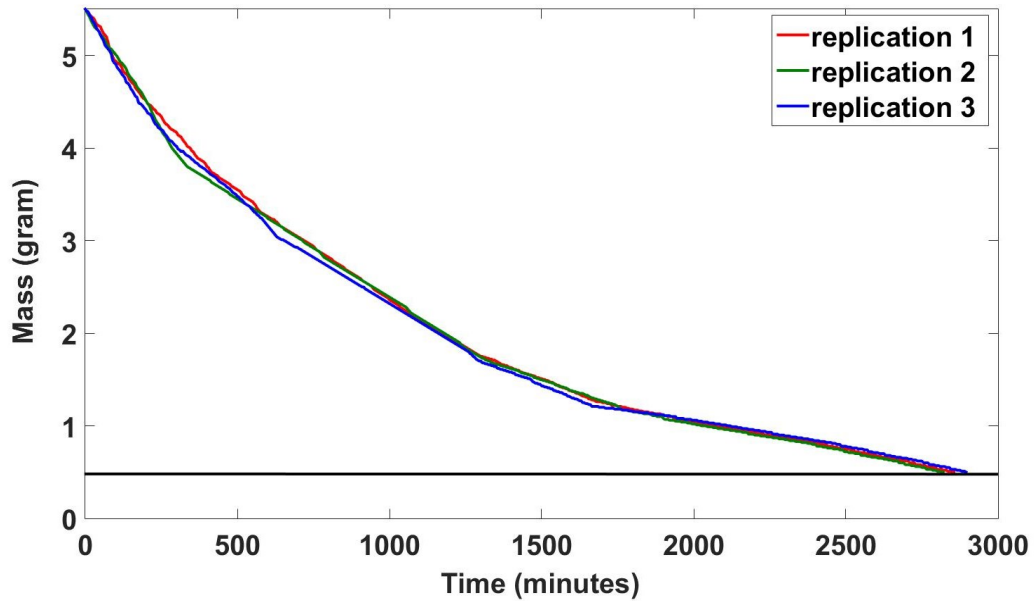


Figure 5.1: Transient mass decrease due to evaporation from hydrophilic soil column. The evaporative mass loss trend for three replications is similar [158]

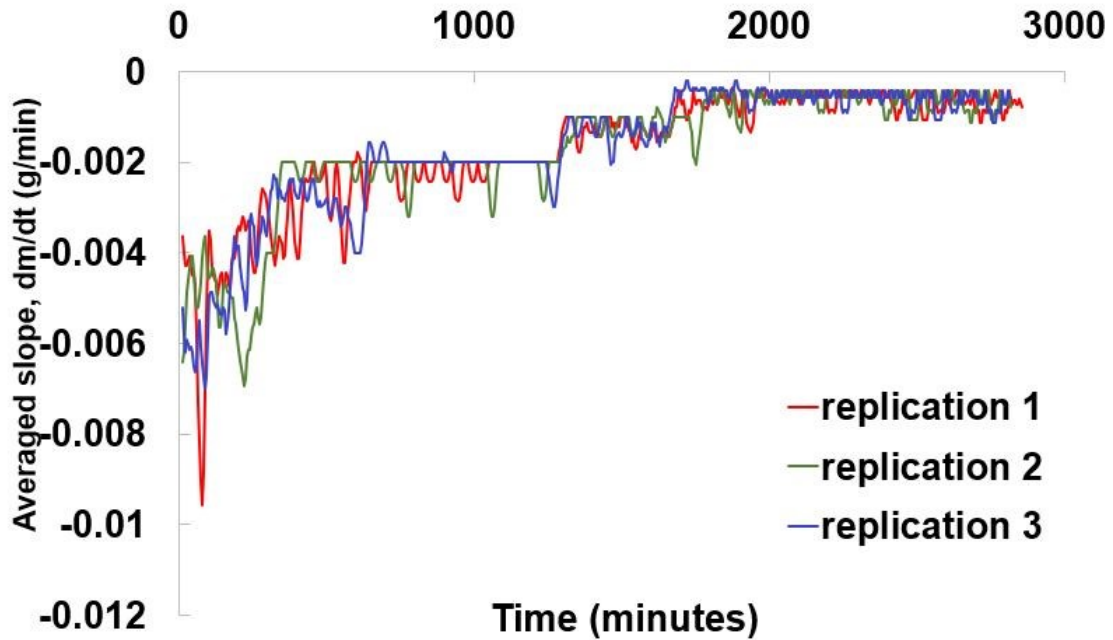


Figure 5.2: Average evaporation time or dm/dt for all three replications. The dm/dt has been calculated at 30 minutes' averaged value [158]

With the mass loss data and time rate of change of mass, the stages of evaporation were determined (Figure 5.3). The evaporation rate was calculated using the following equation and expressed as mm/min:

$$E = \left(\frac{1}{\rho_w A} \right) \frac{dm}{dt} \quad (5.2)$$

where, E is evaporation rate, ρ_w is density of water, A is cross-sectional area of the test section, $\frac{dm}{dt}$ is rate of mass loss. Typically, evaporation is divided into three stages: the constant rate period, the falling rate period and the slower rate period (Figure 2.3) [13, 119]. Due to uniformity of the porous sample (i.e., similar sized spheres), the constant rate period was insignificant or absent. The evaporation rate decreased from maximum of 0.03 mm/min to 0.0064 mm/min until 625th minutes where the evaporation rate was stabilized until 1300th minute. Therefore, from the beginning of the experiments until the 1300th minute, evaporation was in the falling rate period. Then, the

evaporation rate decreased further until 1800th minute and reached to 0.0032 mm/min. After that transition (i.e., after 1800th minute), the evaporation rate was stabilized with an average of 0.0013 mm/min and it continued until the end of each replication. After 1800th minute, the evaporation entered slower rate period and continued until the end.

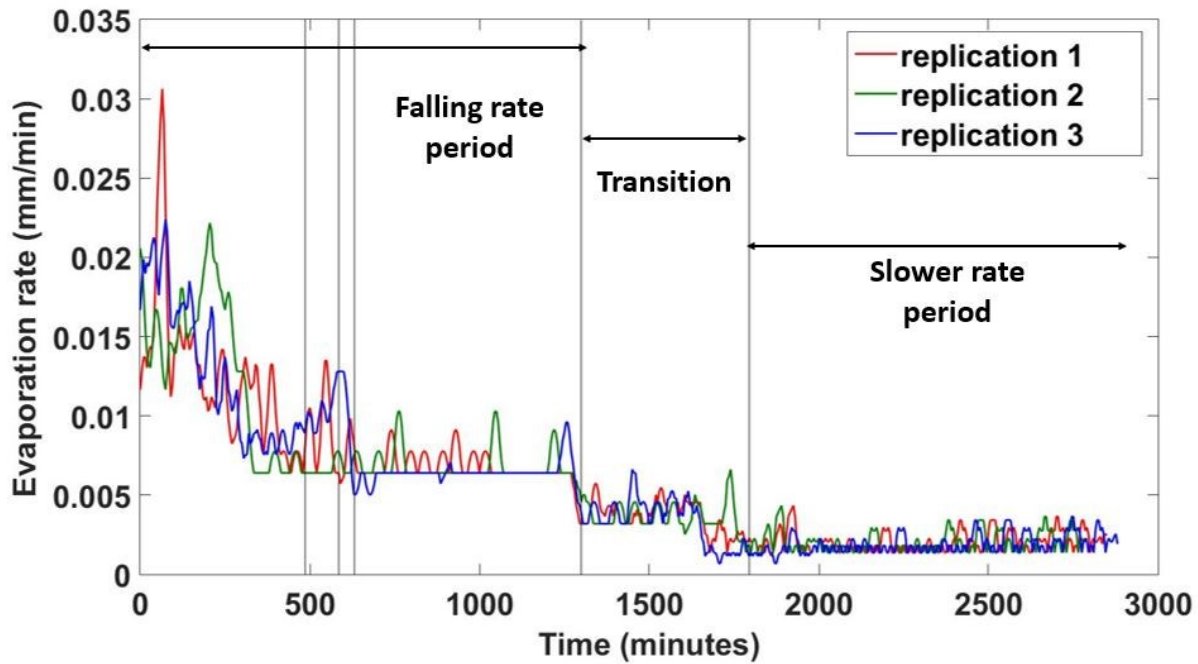


Figure 5.3: Evaporation rate at mm/min for all three replications. The evaporation stages were divided into falling rate period, transition, and slower rate period [158]

5.1.3 Drying front imaging captured with 2D x-rays

X-ray images were captured to observe the propagation of drying front throughout the experiments. During evaporation, the porous sample experiences a reduction in saturation due to evaporative mass loss and drying front propagates throughout the entire sample. Drying front is defined as the vertical height from the top surface of the porous media until the saturated zone. Initially, an image of the test sample (i.e., beaker with spheres) was captured. Subsequently, water was added to the sample and evaporation was started by the application of the solar simulator. X-ray images were captured from the beginning until the 3rd hour, at 30 minutes' interval. Then from

the 4th hour, images were captured at every 8 hours. The images were post-processed in MATLAB where the initial image was subtracted from all the images to visualize the drying front propagation. A log transform of the image was performed to account for the exponential attenuation of x-ray.

Figure 5.4 demonstrates the drying front propagation due to evaporative mass loss from the test sample. Here, the light blue color represents the presence of water and dark blue represents the absence of water (i.e., the evaporative drying front). The evaporation stages were determined from Figure 5.1, Figure 5.2, and Figure 5.3. At the 720th minute, the mass of water was 2.96 g, which means 2.54 g of water were evaporated. The falling rate of evaporation continued until 1300th minute, when 3.84 g of water (e.g., 70% of total mass) was evaporated. The drying front images at 1200th and 1440th minutes represent how the drying front encapsulated the maximum portion of the test sample (Figure 5.4). The evaporation then experienced a stabilized transition from 1300th to 1800th minutes and only 0.52 g of water evaporated in that time. After 1800th minute until the end of the experiments, the evaporation was dominated by slower rate period and within these 16.6 hour, only 0.6 g of water were evaporated and the drying front images at the 2280th, 2640th and 2810th minutes exhibit the slow propagation of drying front. Within this time frame, the drying front captured 90% of the test sample and most of the portion of test sample became unsaturated.

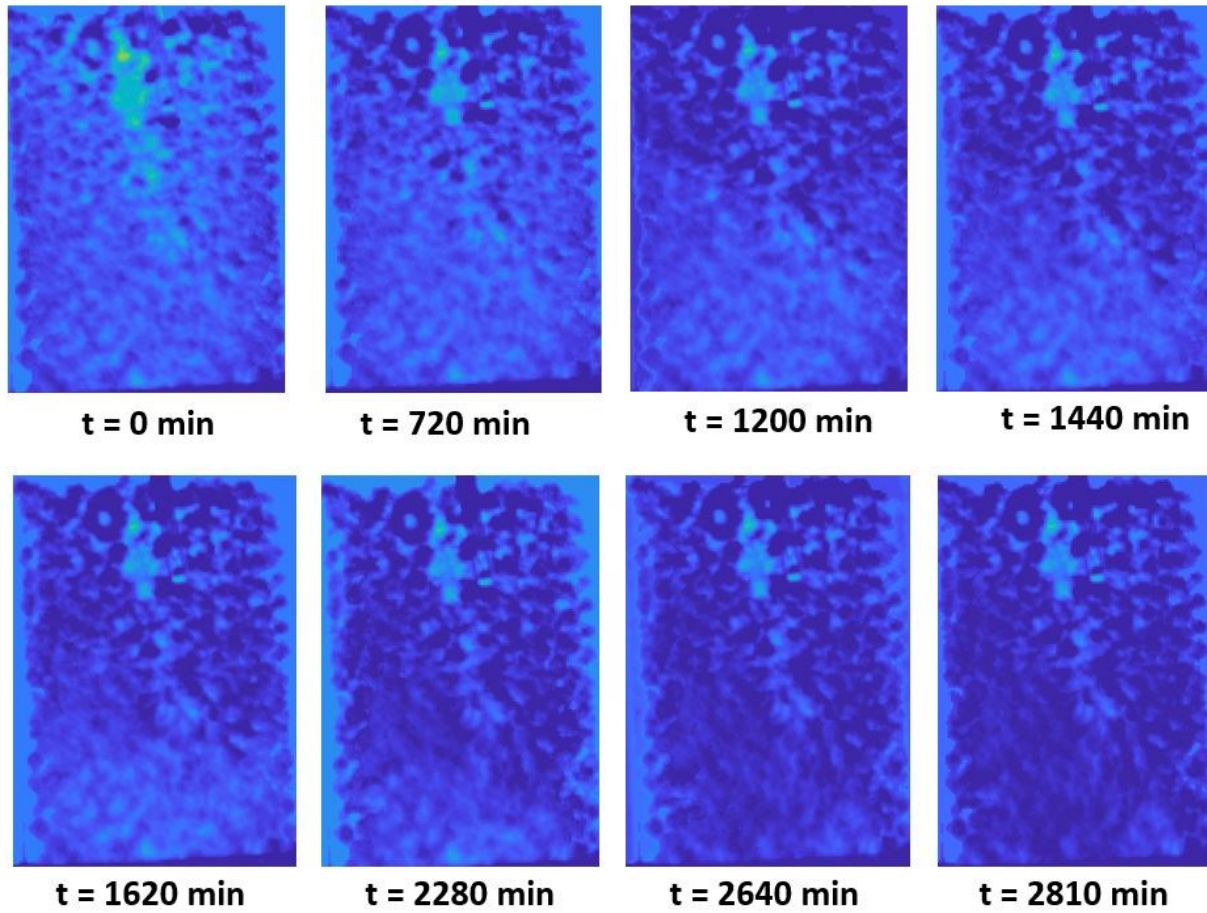


Figure 5.4: Drying front propagation during evaporation from beginning until the end. The light blue color represents presence and deep blue color represents absence of water [158]

5.2 Evaporative drying from hydrophilic and hydrophobic porous columns: consequences of wettability, porous structure, and hydraulic connectivity ¹⁰

In this experiment, evaporation of water has been studied and analyzed from two porous columns made with ~1165 hydrophilic glass and hydrophobic Teflon spheres of same sizes (2.38 mm diameter) filled in two 6-cm-height and 1.88-cm-inner diameter glass cylinders. The evaporative mass loss were recorded at five minutes' interval with a sensitive scale and high resolution x-ray was used to capture images of the drying front propagation. Hydrophilic and hydrophobic columns were compared based on evaporation rate, evaporation stages, propagation of drying front, transient saturation, hydraulic connectivity, and non-dimensional numbers (e.g., Bond number, Capillary number).

5.2.1 Evaporation Phenomena

Evaporation was observed and studied from glass and Teflon columns with the effect of 1000 W/m² heat flux on top with a solar simulator. The experiments were conducted for seven days, and each experiment was repeated five times. The evaporative mass loss was recorded with a sensitive scale (0.01 g of sensitivity) and the mass loss data, and the cumulative mass loss were plotted against time for both glass and Teflon (Figure 5.5). The initial mass of water was 5.8 g and it decreased gradually with time for both glass and Teflon. To compare between the evaporative mass loss, the cumulative mass loss from the beginning of evaporation until seventh day was plotted in the same graph (Figure 5.5). The cumulative mass loss was found greater in glass (i.e., ~ 3 g) in glass than Teflon (i.e., ~2.4 g) after seven days of experiment.

¹⁰ Figures and parts of section Reproduced with permission from Springer Nature“Chakraborty, P. P., Ross, M., Bindra, H., & Derby, M. M. (2022). Evaporative Drying from Hydrophilic or Hydrophobic Homogeneous Porous Columns: Consequences of Wettability, Porous Structure and Hydraulic Connectivity. *Transport in Porous Media*, 1-28”, in press.”

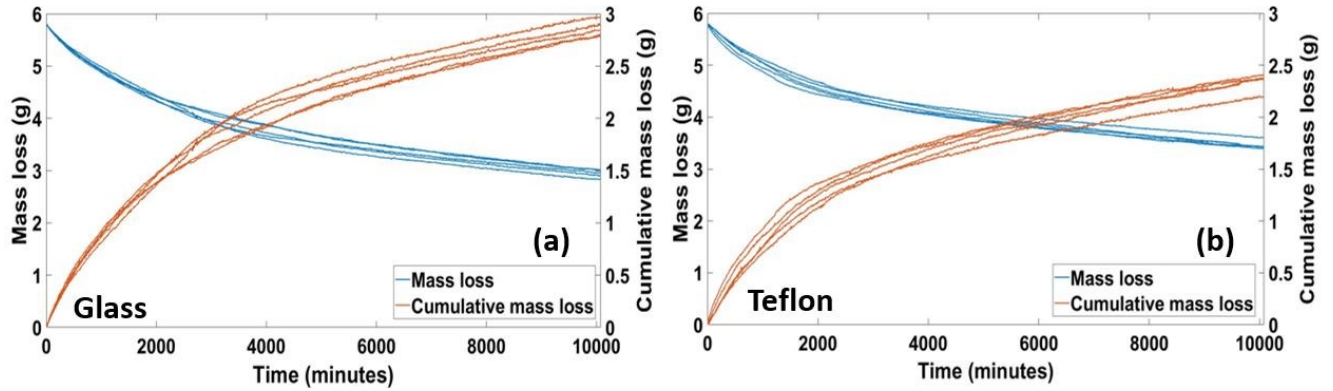


Figure 5.5: Mass loss and cumulative mass loss of water from (a) glass and (b) Teflon columns vs. time. The cumulative mass of glass (i.e., 3 g) is greater than Teflon sample (i.e., 2.4 g) after seven days of experiment [151]

The evaporation rates were determined from evaporative mass loss to differentiate among evaporation stages. Total time for each experiment was 168 hours i.e., seven days and averaged mass at 1 hour increment was used to calculate evaporation rate and change of mass with time (dm/dt). The following equation was used to calculate the evaporation rate:

$$E = \left(\frac{1}{\rho_w A} \right) \frac{dm}{dt} \quad (5.3)$$

Where, E is evaporation rate, ρ_w is density of water, A is cross-sectional area of the test section, $\frac{dm}{dt}$ is rate of mass loss.

The initial evaporation rate was found higher in glass [Figure 5.6 (a and c)] with ~ 7.5 mm/day and maximum of 0.086 g/hour mass loss rate compared to Teflon (~ 5 mm day with 0.06 g/ hour mass loss rate) [Figure 5.6 (b and d)]. Comparing both samples, the initial evaporation rate was 1.5 times higher in glass than Teflon sample. Typically, constant period of evaporation depends on pore size distribution and heterogeneity. For homogeneous porous media and larger pore size distribution, constant rate of evaporation was insignificant in previous studies [60, 146].

The presence of free liquid on top surface and the capillary action related to pore size distribution are associated with significant constant evaporation stage. The characteristic length defined as the hydraulic length connecting the saturated and unsaturated portion of the porous sample until the point where capillary action is dominant can be expressed by the following equation:

$$L_c = \frac{2\sigma}{\rho_w g} \left(\frac{1}{r_1} - \frac{1}{r_2} \right) \quad (5.4)$$

Where, L_c is the characteristic length, σ is the interfacial surface tension, ρ_w is water density, g is acceleration due to gravity, r_1 and r_2 are the smallest and largest drainable pores. The characteristic length determining the constant rate period is directly dependent on the pore size distribution i.e., r_1 and r_2 . For homogeneous porous media with uniform pore size distribution ($r_1 / r_2 = 1$), the characteristic length approaches to zero leading towards absence or insignificant constant rate of evaporation. The uniform spheres' size (2.38 mm) led to a uniform porous distribution in the overall column and resulted in absence of constant period of evaporation.

Due to more wettability, the free water and subsequent layers dried out quickly in glass than Teflon resulting in a sharp decrease in evaporation rate. Due to applied heat flux, each sample experienced a sharp decrease in evaporation rate from the very beginning which is denoted as falling rate period [119] where liquid islands are expected to generate among multiple spheres [13, 21, 22]. The falling rate period lasted longer in glass (until 90th hour) than Teflon (until 70th hour) with a decrease from 5mm/day and 3 mm/day to 1 mm/day for glass and Teflon respectively. After falling rate period, both glass and Teflon sample experienced vapor-diffusion controlled slower rate period (0-1 mm/day) which lasted until the end of each replication. The evaporation rates observed in slower rate period were consistent with the previous literature (Table 5.2).

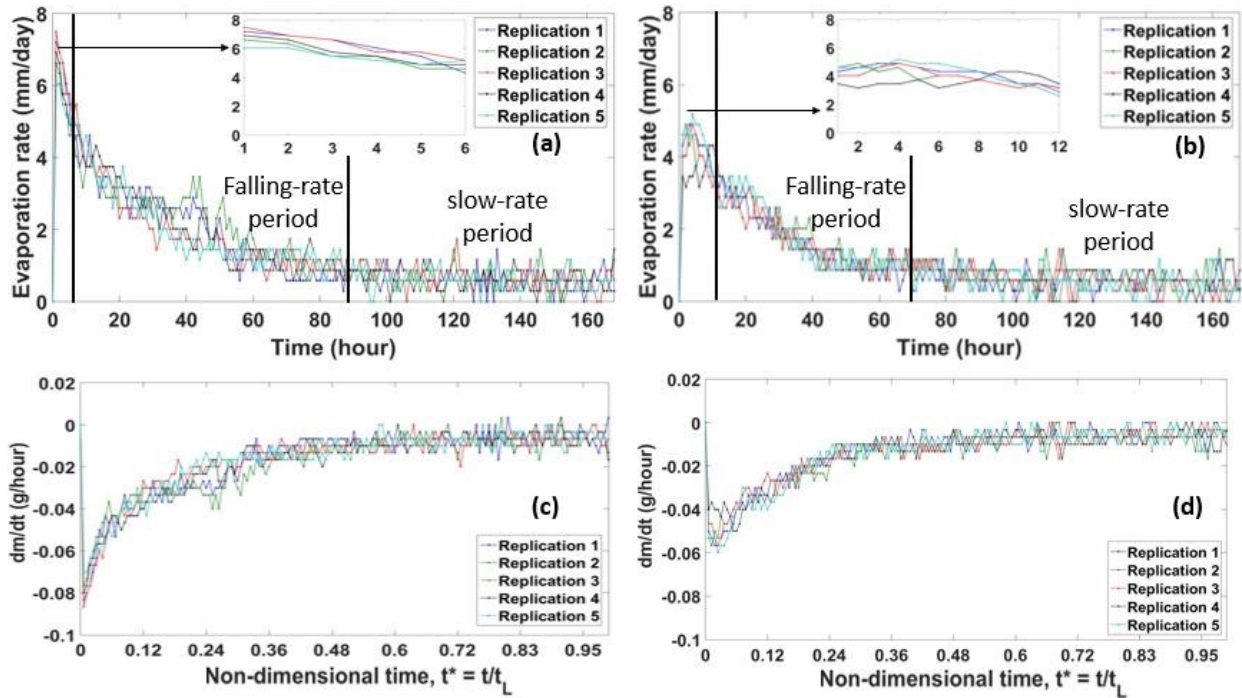


Figure 5.6: Evaporation rate and dm/dt vs time for glass [(a) and (c)] and Teflon [(b) and (d)] columns. Evaporation rates are categorized as falling rate period and slower rate period based on the evaporative mass loss. Transient time has been divided by total time, $t_L = 168$ hours and presented as non-dimensional time, t^* [(c) and (d)] [151]

Table 5.2: Rate of evaporation at slower rate period in previous studies

Reference	Material	grain diameter (mm)	Sample size (mm) Length, Thickness, width	Evaporation rate at slower rate period (mm/day)
Shokri et al. (2008) [16]	Sand	0.3-0.9	$260 \times 75 \times 11$	0-1
Shokri et al. (2009) [12]	Hydrophilic sand	0.3-0.9	$260 \times 75 \times 11$	0-1
	Hydrophobic sand	0.3-0.9	$260 \times 75 \times 11$	0-1
Shokri et al. (2009) [13]	Sand	0.1-0.5	$260 \times 75 \times 11$	0-1
	Sand	0.2-0.3	$260 \times 75 \times 11$	0-0.6

Shokri and Or (2011) [28]	Quartz sand	0.016-0.717	250 × 75 × 10	0-1
	Glass beads	0.063	250 × 75 × 10	0-1
Lehmann et al. (2008) [29]	Fine sand	0.1-0.5	260 × 75 × 10	0-1.5
	Coarse sand	0.3-0.9	260 × 75 × 10	0-1.5

5.2.2 Propagation of drying front

The evaporative drying front propagates as evaporation continues and gradually the portion of unsaturated area increases. Since drying front is a function of saturation and the evaporation experienced a sharp decrease from the beginning, the transient saturation is a critical phenomenon to be determined. The transient saturation was determined using the following formula:

$$S = \frac{V_t}{V_i} \quad (5.5)$$

where, V_i is initial water volume and V_t is transient volume of water.

At the end of each replication (i.e., after seven days), the average saturation of glass sample was less than 50% which means more than 50% of water was evaporated. On the contrary, the Teflon sample experienced on average of 40% of evaporation i.e., 60% of saturation at the end of seven day's experiment [Figure 5.7 (a and b)]. Since the time point for entering slower evaporation rate was determined (i.e., ~90 hours for glass and ~70 hours for Teflon) from Figure 5.6 (a and b), the subsequent transient saturation at those time frame was also determined. From Figure 5.7, the glass sample experienced nearly 60% of saturation while Teflon sample maintained 70% of saturation just before entering slower rate period of evaporation.

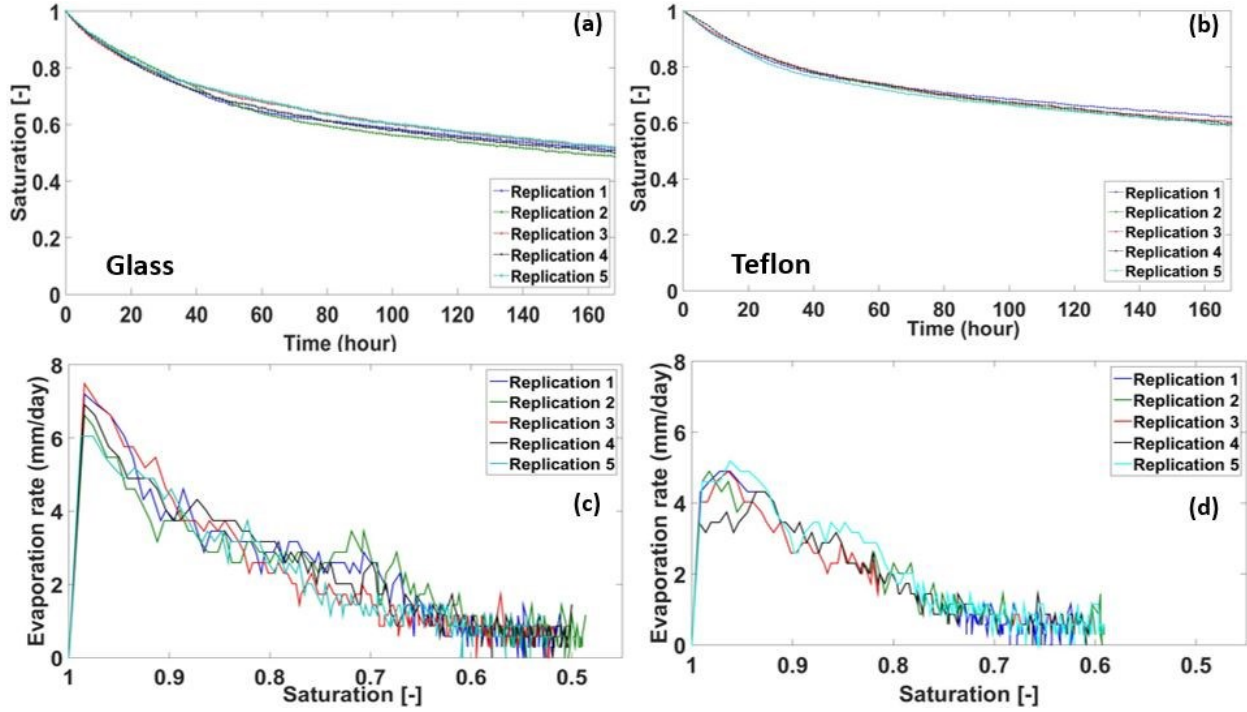


Figure 5.7: Saturation vs. time and evaporation rate vs. transient saturation for glass (a and c) and Teflon (b and d) sample. Approximately, 40% and 30% of total evaporation occurred before slower rate period in glass and Teflon column respectively [151]

As the evaporation continued, the drying front propagated throughout the sample and the portion of unsaturated i.e., dry area increased gradually. Drying front depth is defined as the vertical distance from the top surface of the sample until the final edge of the unsaturated part. As the drying front depth increased, the hydraulic linkage between the saturated and unsaturated parts got disrupted and the evaporation transformed into slower rate period. The drying front depth was calculated using the following equation:

$$L_D = H(1 - S) \quad (5.6)$$

where L_D is drying front depth measured from top surface, H is the beaker height i.e., 60 mm and S is transient saturation. The calculated drying front data were plotted against time for both glass and Teflon [Figure 5.8 (a) and Figure 5.9 (a)] wherein glass the drying front depth was ~30 mm

and in Teflon it was ~24 mm at the end of experiment (i.e., seven days). For each replication, the drying front propagated slowly in Teflon than glass sample.

The propagation of drying fronts was captured with 2D high resolution x-ray for both glass [Figure 5.8 (c)] and Teflon [Figure 5.9 (c)] sample from third day until the end of experiment at 24 hours' time interval. The captured images were post-processed in MATLAB and ImageJ was used to quantify the drying front depths for both sample and they were plotted against time along with the data from equation (5.6) [Figure 5.8 (a)] and [Figure 5.9 (a), red circle]. To minimize the limitations of 2D x-ray and to clearly visualize the drying front propagation, the images were captured from third day until seventh day. In the drying front images, the red color represents the presence of water (i.e., 100% saturation) and deep blue represents the absence of water (i.e., 0% saturation) and the color bar indicates the range of water saturation (i.e., 0-1). Drying front depths were measured using ImageJ from the x-ray images; the drying fronts (marked with black line) were determined where the partially saturated portion meets the unsaturated zone, and the lengths were measured from the bottom to fourteen different points of the drying front for each time frame. Then subtracting those lengths from sample height (i.e., 60 mm), the drying front depths were determined, and the weighted average was plotted against for each time frame [Figure 5.8 (a)] and [Figure 5.9 (a)].

To relate the drying front depth with mass loss of water, the log transform was used, and the fractional mass loss data were plotted against time [Figure 5.8 (b)] and [Figure 5.9 (b)]. The analytical and experimental data coincided well for both glass and Teflon. The fractional mass loss calculated from x-ray was found higher for glass for the last three time frames (i.e., 5th, 6th and 7th day) than the measured mass loss value from the scale which can be due to presence of partial saturation near the drying front. In previous studies, water in hydrophilic porous sample created

hydraulic linkages by forming liquid islands and led to more partial saturation near the drying front than Teflon sample [14, 16, 17, 29]. On contrary, in Teflon sample, the fractional mass loss both from x-ray and scale matched well which represents the uniformity and lack of liquid networks in the hydrophobic Teflon sample.

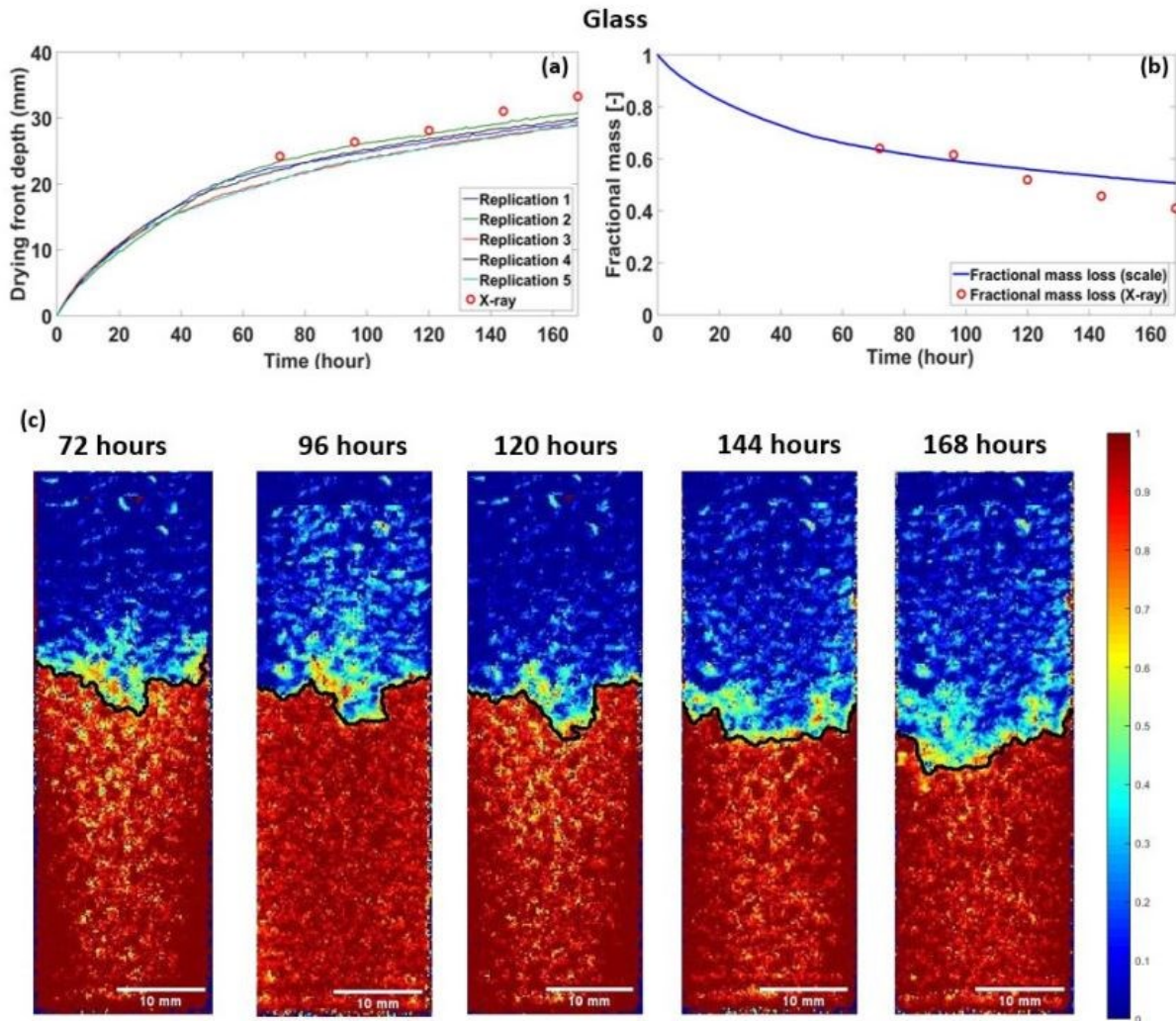


Figure 5.8: (a) Drying front depth vs. time and (b) fractional mass loss calculated from scale and x-ray (log transformed) for glass sample. The bottom pictures (c) show the X-ray imaging of drying front propagation where red and deep blue represents presence (100% water saturation) and absence (0% water saturation) of water respectively. Drying front propagated from ~19 mm to ~34 mm from 3rd day until 7th day. The color bar represents the range of saturation [0-1] and significant partial saturation is observed near the drying front [151]

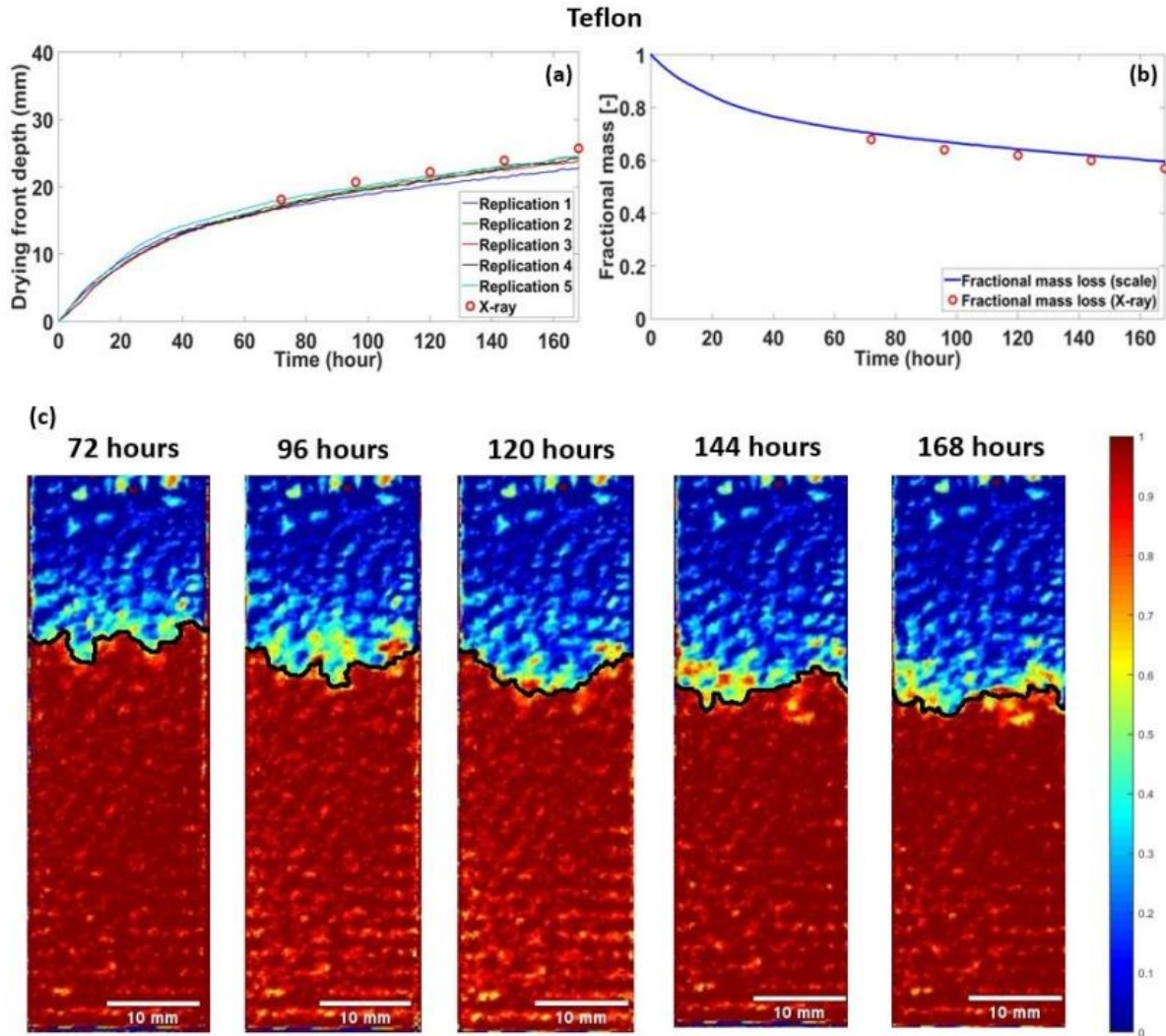


Figure 5.9: (a) Drying front depth vs. time and (b) fractional mass loss calculated from scale and x-ray (log-transformed) for Teflon sample. The bottom pictures (c) show the X-ray imaging of drying front propagation where red and deep blue represents presence (100% water saturation) and absence (0% water saturation) of water respectively. The color bar represents the range of saturation [0-1] and some partial saturation is observed near the drying front [151]

When evaporation from a porous sample enters into slower rate period, the hydraulic connection between the saturated and unsaturated part breaks down and the evaporation is fully dominated by diffusion [11, 12, 14, 17, 29]. The diffusion equation according to Fick's law is expressed as following:

$$J = \frac{\theta_a^{2.5}}{\phi} D \frac{C_{sat} - C_\infty}{L_D} \quad (5.7)$$

$$\phi = 1 - \frac{V_{beads}}{V_{beaker}} \quad (5.8)$$

Where J is diffusive flux, θ_a is volumetric air content, ϕ is porosity, D is water-vapor diffusion coefficient, C_{sat} water-vapor density at evaporating interface, C_∞ is water-vapor density at atmosphere, L_D is drying front depth, V_{beads} is the total volume of all spheres and V_{beaker} is the volume of beaker. For a specific atmospheric condition (temperature, pressure and relative humidity), all the variables except the drying front depth remain constant and during the slower rate period, the diffusion-based evaporation is dependent on the drying front propagation. Following assumptions were made to apply the equation (5.7) by previous researchers [12, 14, 28]:

- (a) Water evaporates from the interface of saturated and unsaturated area i.e., the drying front
- (b) Vapor-diffusion coefficient was computed by the expression of Moldrup et al. [150]
- (c) In the area with no water, volumetric air content is equal to the porosity

In the experimental condition, the $RH = 60\%$, $T_\infty = 22.2^\circ\text{C}$, $T_{surface} = 27^\circ\text{C}$, porosity, $\phi = 0.49$. For calculating the evaporation rate, the diffusive heat flux was divided with the density of water and the unit was converted to mm/day. Calculated diffusive fluxes were plotted against time along with evaporation rate for both glass and Teflon sample (Figure 5.10). In this study, slower evaporation rate starts from ~90 hours and ~70 hours for glass and Teflon and the diffusive flux matched well the evaporation rate from that point. Due to breakup in hydraulic connectivity, evaporation becomes fully dominated by vapor diffusion and the current result shows validation of the model predicted by previous research [12, 28].

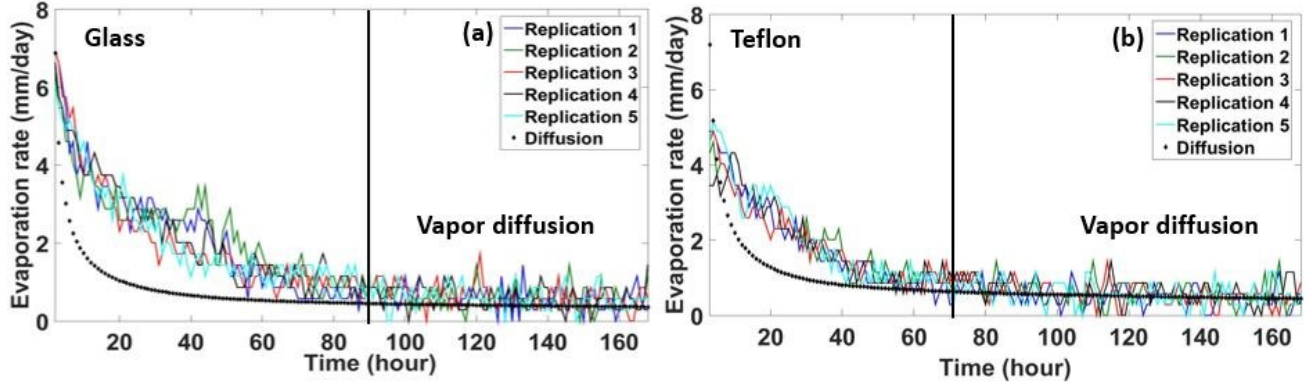


Figure 5.10: Diffusive flux and evaporation rate for glass and Teflon. Diffusive flux matched well with the evaporation rate when it entered into slower rate period for both glass (after 90 hours) and Teflon (after 70 hours) sample [151]

5.2.3 Rayleigh-Nusselt correlation and calculation (fully saturated state)

Natural evaporation of water from porous media has been analyzed and quantified by previous researchers both theoretically [159-163] and experimentally [121, 164]. Boelter et al. [159] investigated natural evaporation of water from a free horizontal space and validated the correlation of Nusselt and Grashof number. In another study, Lloyd and Moran [162] established the correlation for Sherwood and Rayleigh numbers for natural convection from porous media using the following expression:

$$Sh = 0.54Ra^{\frac{1}{4}}(2.2 \times 10^4 \leq Ra \leq 8 \times 10^6) \quad (5.9)$$

$$Sh = 0.15Ra^{\frac{1}{3}}(8 \times 10^6 \leq Ra \leq 1.6 \times 10^9) \quad (5.10)$$

Where, Sh is Sherwood number and Ra is Rayleigh number. Bower and Saylor [160] theoretically analyzed the correlation between Sherwood and Rayleigh numbers for natural convection-driven evaporation phenomena. The Rayleigh number was expressed as following:

$$Ra = \frac{g(\rho_w - \rho_\infty)L^*{}^3}{\bar{\rho}v\alpha} \quad (5.11)$$

Where, g is acceleration due to gravity, ρ_w is saturated water-vapor density at evaporative front, ρ_∞ is water-vapor density at ambient, $L^* = \frac{A}{P}$ is characteristic length, A and P are surface area and wetted perimeter, $\bar{\rho}$ is average of ρ_w and ρ_∞ , ν and α are kinematic viscosity and thermal diffusivity of air.

Goldstein et al. [161] theoretically modeled and validated natural convection of water from free surface as like convection from a horizontal flat plate and the following Rayleigh-Nusselt correlation was established:

$$Nu = 0.59 (Ra)^{1/4}, 200 < Ra < 10^4 \quad (5.12)$$

$$Nu = \frac{hL^*}{k_a} \quad (5.13)$$

where h is convective heat transfer coefficient, k_a is thermal conductivity of air and D is mass diffusivity. Mass diffusivity is derived from the following equation [33] :

$$D = D_{298K} \left(\frac{T}{298}\right)^{3/2} \quad (5.14)$$

In their work, Suzuki and Maeda [163] theoretically modeled natural evaporation of water from granular packed beds by analyzing Rayleigh-Nusselt correlation and Kumar and Arakeri [121, 164] experimentally determined the Rayleigh and Nusselt numbers. Table 5.3 represents the comparison of Rayleigh and Nusselt number calculation of present and previous studies. In this study, the calculated Rayleigh and Nusselt numbers were 2380 and 4.1 respectively. These values are almost similar order of magnitude as those found by the study of Kumar and Arakeri [121], although the temperature gradient and relative humidity were higher in that study.

Table 5.3: Rayleigh-Nusselt number calculation for natural evaporation at fully saturated state and comparison with previous studies

Reference	Porous material	Surface Temperature (° C)	Ambient Temperature (° C)	RH (%)	Ra [-]	Nu [-]
Kumar and Arakeri (2018)	Glass plate	38	26.7	69.3	1540	3.7
	Cover slip	37.9	26.4	72.7	883	3.2
Present work	Glass/ Teflon spheres	27	22	60	2380	4.1

5.2.4 Calculation of Bond number and Capillary number

In porous samples similar to present study, Bond and capillary numbers were calculated in previous studies [120, 130, 165] to understand the relation between capillary force with gravitational and viscous force. Following equations were used to calculate Bond and Capillary number in a porous sample:

$$Bo = \frac{\rho_L g r_{avg}^2 \sin \theta_{tilt}}{\sigma} \quad (5.15)$$

$$Ca = \frac{3\pi\mu DC_{sat}}{\sigma\rho_L r_{avg}} \quad (5.16)$$

Where, ρ_L is density of liquid, g is acceleration due to gravity, σ is interfacial surface tension, r_{avg} is average bead radius, θ_{tilt} is sample tilt angle, μ is dynamic viscosity, D is diffusion co-efficient, C_{sat} is saturated vapor concentration. The interfacial tension was calculated from the following equation [166]:

$$\sigma = 235.8 \left(1 - \frac{T_{sat}}{T_c}\right)^{1.256} \left[1 - 0.625 \left(1 - \frac{T_{sat}}{T_c}\right)\right] \quad (5.17)$$

Typically, Bond number depends on the liquid properties such as density, interfacial tension, and average radius of the porous media particle and since, Bond number is directly proportional to the square of average particle radius, it increases with increasing particle size [120, 130, 167]. In this study, Bond number was 193E-3 for 1.19 mm of average sphere's radius. The comparative analysis of Bond and capillary number calculation for previous and present studies is represented in Table 5.4. Yiotis et al. [130] and Cejas et al., [120] analyzed some effects of tilt angle on Bond number, but since in this study the test sample was vertical, 90° of tilt angle was considered to calculate Bond number. The Capillary number is inversely proportional to the average sphere's radius and for lower sphere size, higher capillary number [130] was found and vice versa [120] [123]. In some studies [23, 123], capillary number was calculated as a function of constant evaporation rate, but due to absence of constant rate, in this study, the capillary number was calculated as a function of particle or sphere's radius.

Table 5.4: Bond and Capillary number calculation for different studies

Reference	Porous media material	Average sphere radius (mm)	Working fluid	Bond number, Bo [-]	Capillary number, Ca [-]
Rogers and Kavinay, 1990 [167]	Glass spheres	0.1	Water	1.4E-3	Not reported
		0.5	Water	33.7E-3	
		1.5	Water	302E-3	
Yiotis et al., 2012 [130]	Glass spheres	0.065	n-pentane/ n-hexane	1.62E-3	8520E-8
		0.225	n-pentane/ n-hexane	19.5E-3	2460E-8
Cejas et al., 2017 [120]	Glass spheres	0.25	Water	9.1E-3 – 49E-3	0.85E-8 – 4.93E-8
		0.5	Water	36.2E-3 – 196E-3	0.89E-8 – 3.33E-8
Kumar and Arakeri, 2019 [164]	Glass spheres	0.35	Water	2.34E-3	6.19E-8
		0.425	Water	2.48E-3	4.67E-8
Present work	Glass/ Teflon spheres	1.19	Water	193E-3	6.203E-8

5.2.5 Permeability modeling

Permeability is a measurement of how easily a working fluid can transmit through a porous media. For porous media made with uniform spheres, the traditional equation to calculate permeability is Kozeny-Carman [168, 169] equation which is expressed as following:

$$k = \frac{\bar{D}^2 \varphi^3}{72 \tau (1 - \varphi)^2} = \frac{\bar{D}^2 \varphi^3}{180 (1 - \varphi)^2} \quad (5.18)$$

Where, \bar{D} is grain diameter, φ is porosity and 180 is the product of a constant coefficient 72 and an average tortuosity, $\tau = 2.5$, estimated by Lake et al. [170]. Several previous studies [27, 171, 172] postulated that, Kozeny-Carman equation overestimates the value of permeability of uniform porous sample especially in lower porosity. One of the models of modifying Kozeny-Carman equation for uniform porous media created with uniform spheres is the RGPZ (Revil, Glover, Pezard, and Zamora) model [27, 173] :

$$k = \frac{\Lambda^2}{cF} \quad (5.19)$$

where, k is permeability, Λ is characteristic pore radius, c is pore shape factor, and F is formation factor, where Λ and F are expressed by following equations:

$$\Lambda = \frac{d}{2mF} \quad (5.20)$$

$$F = \phi^{-m} \quad (5.21)$$

where, d is representative grain diameter, m is cementation exponent, and ϕ is porosity. For spherical particles, $m = 1.5$ and $c = 8/3$. The model was validated for 15 spherical uniform glass beads packing [26, 27] and the following equations were used to introduce effective pore radius within same permeability model:

$$\Theta = \sqrt{\frac{cm^2F^2}{8}} \quad (5.22)$$

$$\Lambda = \frac{\Theta r_{eff}}{mF} = r_{eff} \sqrt{\frac{c}{8}} \quad (5.23)$$

$$k \approx \frac{\Lambda^2}{cF} = \frac{r_{eff}^2}{8F} \quad (5.24)$$

Where, Θ is theta transform (unitless) and r_{eff} is effective pore radius. Alternatively, Ghanbarian et al. [25] proposed another model named CPA (Critical Path Analysis) to predict permeability of a uniform homogeneous porous sample. The predicted model (CPA) matched well with the experimental permeability with minimum RMSLE (Root Mean Square Log-Transformed Error) of 0.16. In this model, the critical diameter $d_c = 0.42\bar{D}$, where \bar{D} is average bead's diameter. The permeability is expressed as following equation:

$$k = \frac{d_c^2}{CF} \quad (5.25)$$

Where, C is a constant co-efficient and for spherical mono-disperse particle, the value was set as 72.2 which produced significantly better (RMSLE=0.16) permeability results. Using, these two above-mentioned models, the permeability of this study was achieved as $k(RGPZ) = 3.163E - 9 m^2$ and $k(CPA) = 3.287E - 9 m^2$. In a study [26], using glass beads of several sizes, permeability was calculated using the RGPZ model and Table 5.5 demonstrates the permeability results of previous and this studies:

Table 5.5: Calculation of permeability of previous and this study

Reference	Effective grain	Cementation exponent, m	Porosity, ϕ	Effective pore	Permeability, k (m^2)

	diameter, (μm)			radius, μm	
Glover, et al., 2006	1000 \pm 34	1.56 \pm 0.005	0.3954	150.6 \pm 10.2	0.724E-9
	2000 \pm 67	1.49 \pm 0.005	0.3856	281 \pm 18.9	2.386E-9
	3350 \pm 184	1.48 \pm 0.005	0.3965	498.5 \pm 44.2	7.902E-9
Glover and Walker, 2009	3000 \pm 154	1.56 \pm 0.005	0.3978	395.4 \pm 32.9	4.638E-9
	4000 \pm 198	1.55 \pm 0.005	0.3854	509.84 \pm 41. 7	7.411E-9
Present work	2380	1.5	0.477	326.4	3.163E-9 (RGPZ)
					3.287E-9 (CPA)

5.2.6 Physical measurement of permeability

Hydraulic conductivity of the porous system was measured physically in this study using a constant head technique (Figure 5.11) and the relationship between hydraulic conductivity and permeability was used to determine permeability. Two porous samples were created with 1300 glass and Teflon spheres (2.38-mm-diameter) in two 2.54-cm-diameter and 2.86-cm-tall glass tubes with both sides open. To allow the water to flow through the sample and to hold the spheres in their places, two metal meshes were used in both open sides of the glass tubes. Water was placed in a sufficiently large reservoir ($l = 42$ cm, $w = 30$ cm, and $h = 17$ cm) to maintain a near-constant pressure head. A 24-cm long translucent plastic tube with inner diameter of 2.54 cm was used to connect the reservoir with the porous sample. The initial head of the water in the reservoir was maintained at 42 cm and the water was let to pass through the porous sample for 10 seconds by the action of gravity. Each sample was tested five times and for each test the water was collected in a tank and the mass was measured in real-time using a scale. From the mass of water collected,

the flow rate was measured, and the hydraulic conductivity of each sample was calculated using following equation:

$$K = \frac{Q}{iA} \quad (5.26)$$

$$Q = \frac{V}{t} \quad (5.27)$$

$$i = \frac{-\Delta h}{L} \quad (5.28)$$

where, K is hydraulic conductivity, Q is volumetric flow rate, V is amount of water collected, t is time, Δh is the pressure head difference, L is height, and A is cross sectional area of the test sample. The following permeability-hydraulic conductivity relationship was used to calculate permeability of the porous system [174]:

$$k = \frac{K\mu}{\rho g} \quad (5.29)$$

where, k is permeability, μ is viscosity, ρ is density of water, and g is acceleration due to gravity. The measured permeability of the glass sample was approximately 6% higher than Teflon due to hydrophilicity. For glass, the average permeability was $9.5\text{E-}10 \text{ m}^2$ with a standard deviation of $2.7\text{E-}11 \text{ m}^2$ and for Teflon, the average permeability was $8.9\text{E-}10 \text{ m}^2$ with a standard deviation of $1.21\text{E-}11 \text{ m}^2$. The comparable values of predicted (RGPZ and CPA models) and measured permeabilities are presented in Table 5.6.

Table 5.6: Predicted and measured values of permeability for the porous sample

Predicted		Experimental	
k (RGPZ) (m^2)	k (CPA) (m^2)	k (measured), glass, (m^2)	k (measured), Teflon, (m^2)
3.163E-9	3.287E-9	9.5E-10	8.9E-10

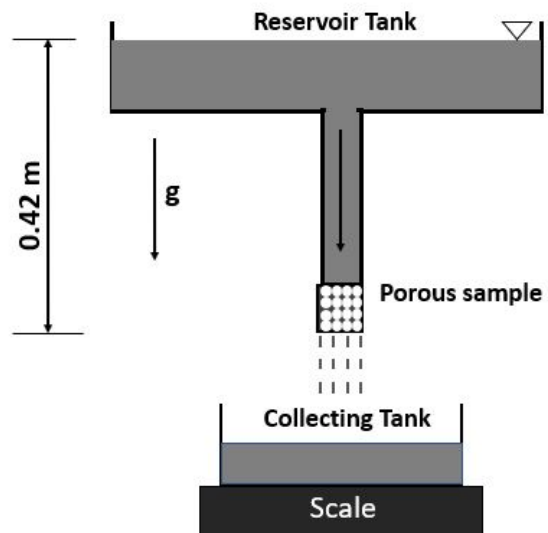


Figure 5.11: Physical measurement of hydraulic conductivity of the porous system using constant head method [151]

Chapter 6 - Droplet penetration and water evaporation from 3D-printed porous structures

6.1 Evaporation of deionized water from 3D-printed porous structure

The experimental procedure of water evaporation from 3D-printed porous structures were discussed in section 3.3.3. Initially, the structure was dipped in deionized water until the water invaded all the pores. Subsequently, the structure, which was holding water, was placed on the top of a sensitive scale and 1000 W/m^2 of heat flux were applied to the top surface using a solar simulator. The evaporative mass loss was recorded with the sensitive scale at 15 minutes' time intervals and the evaporation phenomenon and drying front propagation was visualized with a high-speed camera. Evaporation mechanisms from three 3D-printed structures were investigated, including drying front propagation, transient saturation, thermal gradients due to incident heat flux and evaporative mass losses.

6.1.1 Evaporative mass loss

At the beginning of the experiment, all three 3D-printed structures were weighed, and the masses were recorded. Then they were immersed into the water and placed on the scale. After the experiment, the mass of 3D structure was subtracted from the transient mass recorded, and the evaporative mass loss of water was calculated at 15 minute's intervals. The average total mass of the 3D structure with holding water and the initial mass of water (i.e., the water holding capacity) of each 3D structure is presented in following table:

Table 6.1: Mass properties of 3D-printed porous structures

Mass	3D structure-1	3D structure-2	3D structure-3
Total initial mass with water (g)	0.87	0.91	2.1
Mass of 3D structure (g)	0.42	0.61	1.31
Initial mass of water (g)	0.45	0.3	0.79

3D structure-3 held more water (i.e., 0.79 g) than the other two due to its larger size and volume. Due to its higher porosity, 3D structure-1 held more water than 3D structure-2. Additionally, 3D structure-2 had two layers of solid filled material in the y - z direction, resulting in the lowest porosity and lowest water holding capacity. Since, the empty volume of the 3D-printed structure was invaded by water, the porosity was calculated using the following formula:

$$\varphi = \frac{V_E}{V_T} \times 100\% \quad (6.1)$$

where, φ is porosity, V_E is empty volume, V_T is total volume of the 3D printed structure. The porosity was calculated using two methods: first, it was calculated based on the mass [equation (6.1)] and second, it was calculated using the “mass properties” toolbox of SolidWorks 2018 (Table 6.2). The porosity calculated with equation and SolidWorks toolbox matched well with 0.09-0.65% of percent difference.

Table 6.2: Porosity calculation of 3D printed porous structure

	3D structure 1	3D structure 2	3D structure 3
Porosity [equation (6.1)]	45.87%	30.58%	33.27%
Porosity (Solidworks)	46%	31.5%	34.2%
Percent difference	0.09%	0.6%	0.65%

The evaporative mass loss of water from three 3D-printed structures were recorded and plotted (Figure 6.1). Each experiment was replicated three times and the transient mass losses were plotted in the same graph. The experiments were continued until at least 80% of the water was evaporated from the porous structure. 3D structure-3 experienced the sharpest decrease in the evaporative mass loss as the water evaporated from 0.8 g to approximately 0.1 g within 180 minutes. 3D structures 1 and 2 experienced similar trends in evaporative mass loss as both the structures were nearly identical. Due to greater water holding capacity of 3D structure-1, it took more time to evaporate water from it than the 3D structure-2. It took around 225 minutes to evaporate approximately 0.38 g of water (i.e., 86% of total water) from 3D structure-1 while 0.28 g (i.e., 88% of total water) of water was evaporated in 150 minutes from 3D structure-2.

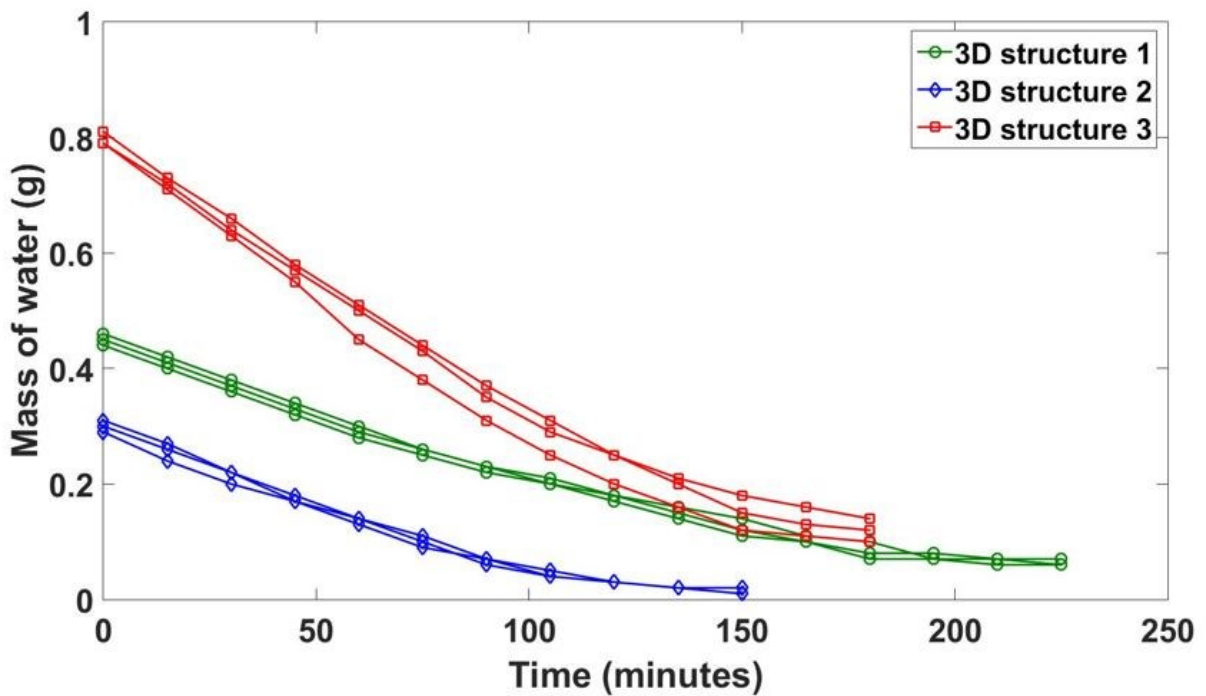


Figure 6.1: Evaporative mass loss of water from three 3D-printed structures

6.1.2 Transient saturation and drying front propagation

During evaporation, the saturation of the porous structure decreased, and portion of unsaturated areas increased over time. The drying front depth is defined as the vertical distance from the top of unsaturated portion to the saturated part of the porous media, and it depends on the transient saturation of the porous media. Throughout the porous structure, the transient saturation was calculated using the following equation:

$$S = \frac{V_t}{V_i} \quad (6.2)$$

where, V_i is initial water volume and V_t is transient volume of water. Figure 6.2 demonstrates the transient saturation due to evaporative mass loss from three structures for all three replications. The saturation decreased gradually with time for all three structures but 3D structure-2 experienced sharpest decrease in saturation due to lower initial volume of water.

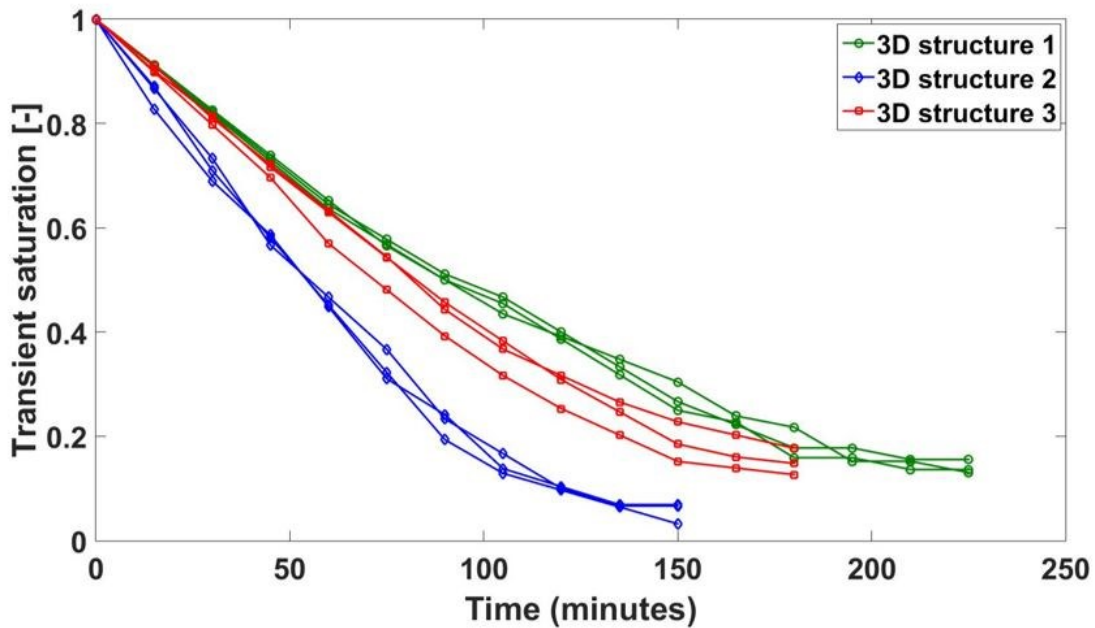
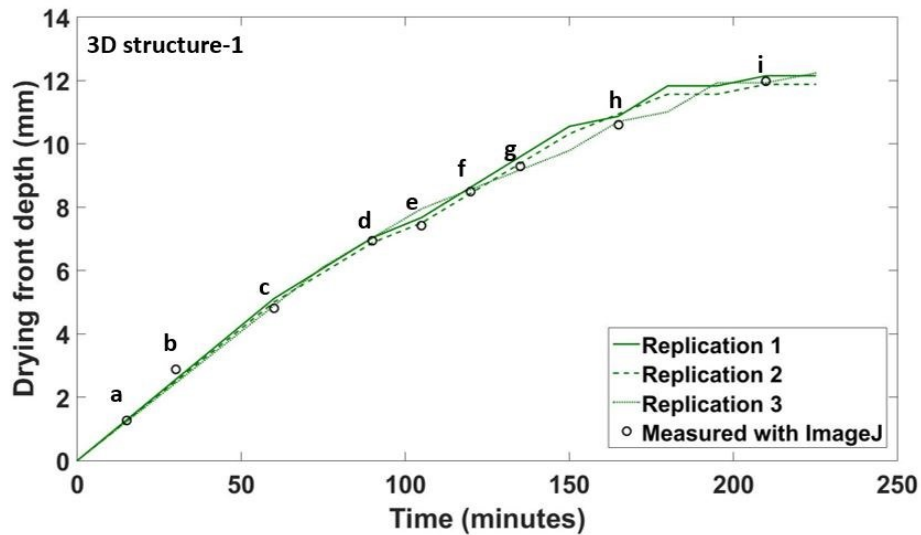


Figure 6.2: Transient saturation vs. time for 3D structure-1, 3D structure-2 and 3D structure-3

During evaporation, drying fronts propagate through the porous medium and portion of unsaturated areas increases. In this experiment, due to evaporative mass loss, the length of drying front increased gradually with time and encapsulated the whole structure. Since the drying front is a function of transient saturation, the length of drying front can be estimated by the following formula:

$$L_D = H(1 - S) \quad (6.3)$$

where L_D is drying front depth, H is height of the porous structure, and S is transient saturation of the porous medium. Figure 6.3, Figure 6.4 and Figure 6.5 show the drying front propagation in 3D structure 1, 2 and 3. The drying front depths calculated using equation (6.3) were plotted against time. During evaporation, the drying fronts propagated throughout the porous structure and the depths increased with time. The drying fronts were also measured from the images captured with high-speed camera with ImageJ and plotted in the same graph. The drying fronts calculated from the equation and measured from the images matched well.



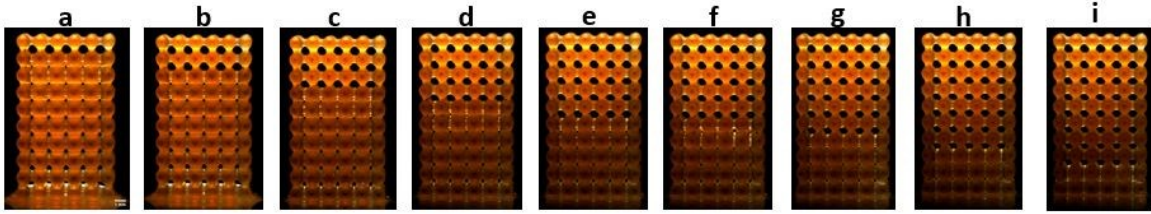


Figure 6.3: Drying front depth during evaporation from 3D structure-1.

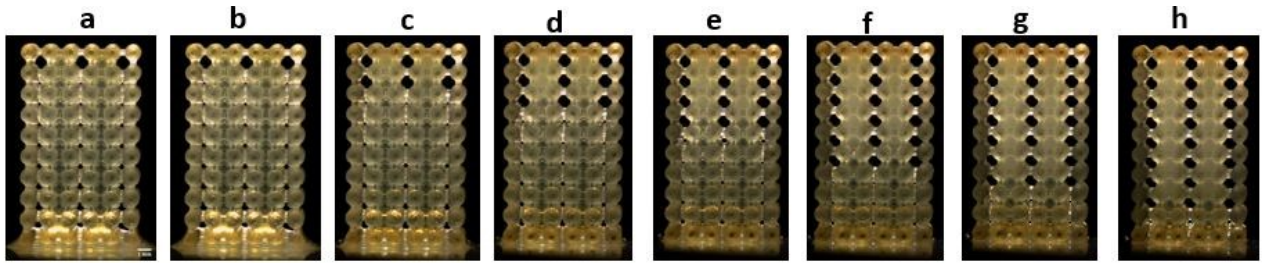
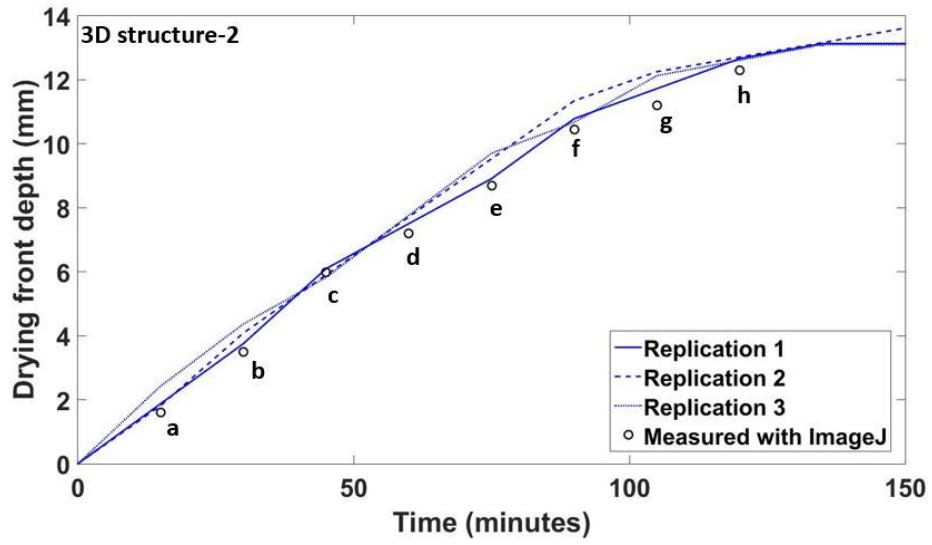


Figure 6.4: Drying front depth during evaporation from 3D structure-2

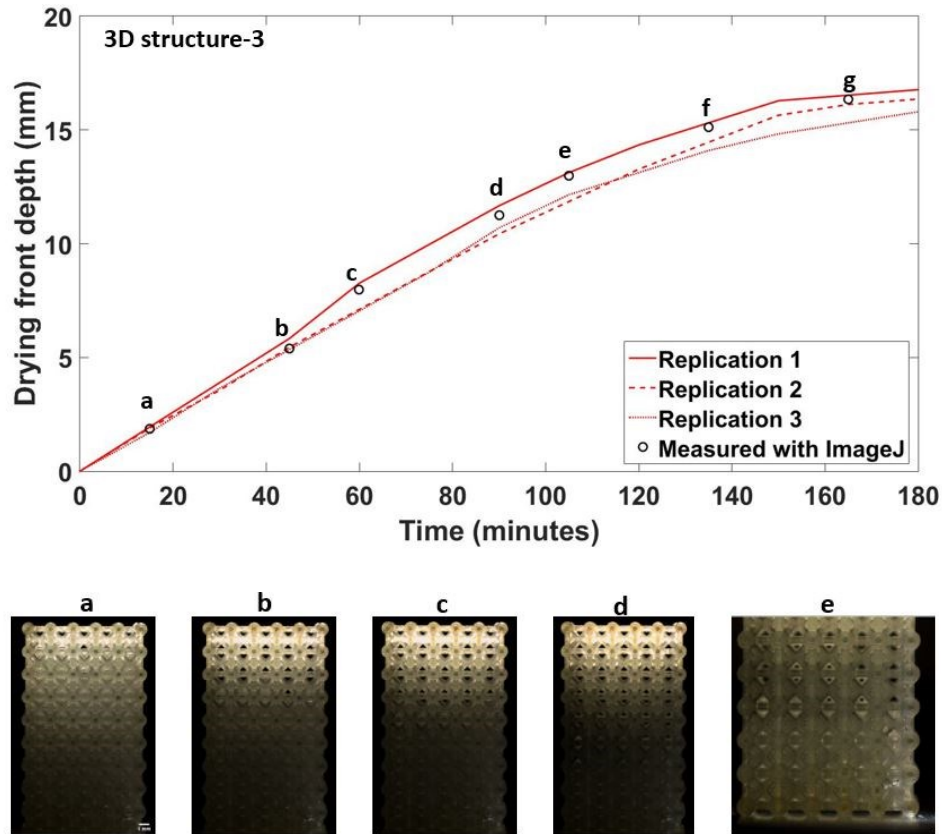


Figure 6.5: Drying front depth during evaporation from 3D structure-3

6.1.3 Modeling evaporation rates

The evaporation rates (i.e., $\frac{dm}{dt}$) were calculated from the mass loss data. Consequently, a heat transfer model was formulated based on the energy balance on different layers of the porous structure. Figure 6.6 demonstrates the schematic diagram of the energy balance on a single layer of the porous structure. The following assumptions were made to predict the model:

- (a) The model assumed steady state.
- (b) Energy balance was considered only in the vertical direction of the porous structure.
- (c) The model predicted mass loss in a layer-by-layer consideration.
- (d) In a layer, the 3D-printed material and water were assumed to be in isothermal state.

- (e) Energy and mass loss from the sides were neglected.
- (f) The area was predicted as the total top surface of the porous structure.
- (g) The temperature of the porous structure during evaporation was measured and recorded with a thermal camera and the subsequent layer temperature was estimated from the thermal images.

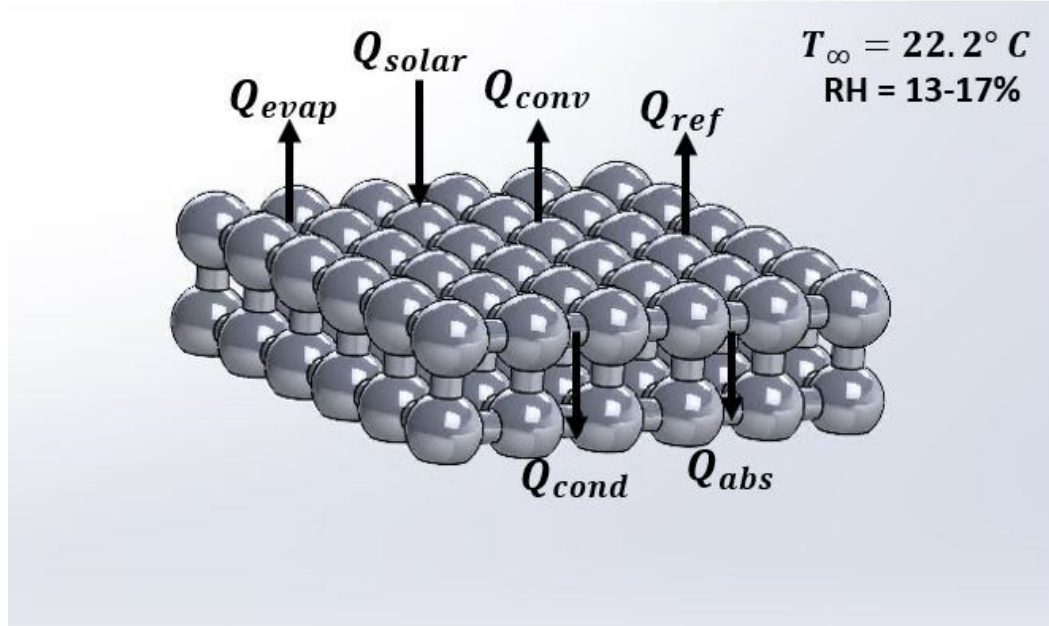


Figure 6.6: Steady-state heat transfer in a single layer of the porous structure

For a single layer of the porous structure, the energy balance equation is stated as follows:

$$\begin{aligned}
 (1 - \varphi)A\alpha Q_{solar} & \qquad \qquad \qquad (6.4) \\
 = A (1 - \varphi) \frac{\sigma(T_s^4 - T_\infty^4)}{[\frac{1}{\epsilon_s} + \frac{1}{\epsilon_a} - 1]} + A\varphi \frac{\sigma(T_w^4 - T_\infty^4)}{[\frac{1}{\epsilon_w} + \frac{1}{\epsilon_a} - 1]} \\
 + h_{conv}A\varphi(T_w - T_\infty) + K_{eff}A \left(\frac{T_s - T_B}{L} \right) + \dot{m}\varphi h_{lg}
 \end{aligned}$$

where φ is porosity, A is surface area of the top layer of the porous surface, α is absorptivity of the porous structure, Q_{solar} is applied heat flux by solar simulator, σ is Stefan-Boltzman constant,

T_s is surface temperature, T_w is water temperature, T_∞ is ambient temperature, ϵ_s is emissivity of the porous structure, ϵ_a is emissivity of air, h_{conv} is convective heat transfer coefficient, T_w is water temperature, K_{eff} is effective thermal conductivity, T_B is bottom temperature of single layer, L is single layer thickness, \dot{m} is the evaporation rate, and h_{lg} is latent heat of vaporization. The effective thermal conductivity is expressed by following equation:

$$K_{eff} = (1 - \phi)K_s + \phi K_w \quad (6.5)$$

where K_s is thermal conductivity of the porous material and K_w is thermal conductivity of water.

To calculate the convective heat transfer coefficient, the following equation was used to calculate Rayleigh number:

$$Ra = \frac{g\beta k(T_w - T_\infty)x}{\nu_a \alpha_m} \quad (6.6)$$

where Ra is Rayleigh number, g is acceleration due to gravity, β is the thermal expansion coefficient, k is intrinsic permeability of the porous medium, x is length of the porous top surface, ν_a is kinematic viscosity of air, and α_m is thermal diffusivity. The intrinsic permeability is expressed as follows:

$$k = 0.01 \phi r_{eff}^2 \quad (6.7)$$

where ϕ is porosity and r_{eff} is effective pore radius. The following Raleigh-Nusselt correlation was used to calculate Nusselt number for laminar flow:

$$Nu = 0.413 Ra^{\frac{1}{3}} \quad (6.8)$$

$$h_{conv} = \frac{Nu K_a}{x} \quad (6.9)$$

where Nu is Nusselt number, h_{conv} is the convective heat transfer coefficient, and K_a is thermal conductivity of air. Since all the 3D structures were manufactured with same material (i.e., ABS

plastic), the common parameters to estimate steady state evaporation rate are presented in the following table:

Table 6.3: Common parameters to model the steady-state evaporation rate

Ambient temperature, T_{∞}	22.2° C
Applied heat flux, Q_{solar}	1000 W/m ²
Absorptivity, α	0.98
Stefan-Boltzmann constant, σ	$5.67 \times 10^{-8} \text{ Wm}^{-2}\text{K}^4$
Emissivity of solid surface, ϵ_s	0.92
Emissivity of air, ϵ_a	0.85
Emissivity of water, ϵ_w	0.96
Thermal conductivity of solid, K_s	0.163 W/ m-k
Thermal conductivity of water, K_w	0.6049 W/ m-k
Thermal conductivity of air, K_a	0.02529 W/ m-k
Thermal expansion coefficient, β	0.003405 K ⁻¹
Kinematic viscosity of air, ν_a	$8.63 \times 10^{-8} \text{ m}^2\text{s}^{-1}$

For the evaporative rate flux calculations, the temperature of each layer was measured from the images captured with thermal camera. As an example, for the first layer, the top layer of the 3D structure was considered the surface temperature, T_s . After the evaporation of water from first layer, the temperature of the second layer was considered as the surface temperature T_s , as determined from thermal images, Figure 6.7, and the similar procedure was followed until the water level reached to the tenth layer (i.e., the last layer). The three 3D-printed structures, all

manufactured from ABS plastic, exhibited similar temperature gradients throughout all layers. Since the surface temperature and water temperature were assumed to be in thermal equilibrium, for each layer's calculation, $T_s = T_w$ was assumed. For each layer, K_{eff} , Ra , k , Nu and h_{conv} were calculated using equation (6.5), (6.6), (6.7), (6.8), and (6.9), respectively. In different layers, the heat flux, the surface temperature, water temperature and bottom temperature changed. Then, using equation (6.4), the evaporative rate was calculated. At the last two layers (i.e., 9th and 10th) the temperatures were almost similar (e.g., with approximately 0.5K temperature difference), and thus they were considered to be in equilibrium with 8th layer's temperature. Figure 6.7 demonstrates the layer-by-layer thermal gradient during evaporation from 3D structure-1. The solar heat flux in each layer was measured with pyranometer. The heat flux was measured at three points [i.e., at the top (layer 1), at the middle (layer 5) and at the bottom (layer 10)] and by simple interpolation, the heat flux in each layer was estimated. Table 6.4 represents the temperature and heat flux in each layer of the 3D-printed structures. For all structures, the temperature and heat flux in each layer were similar.

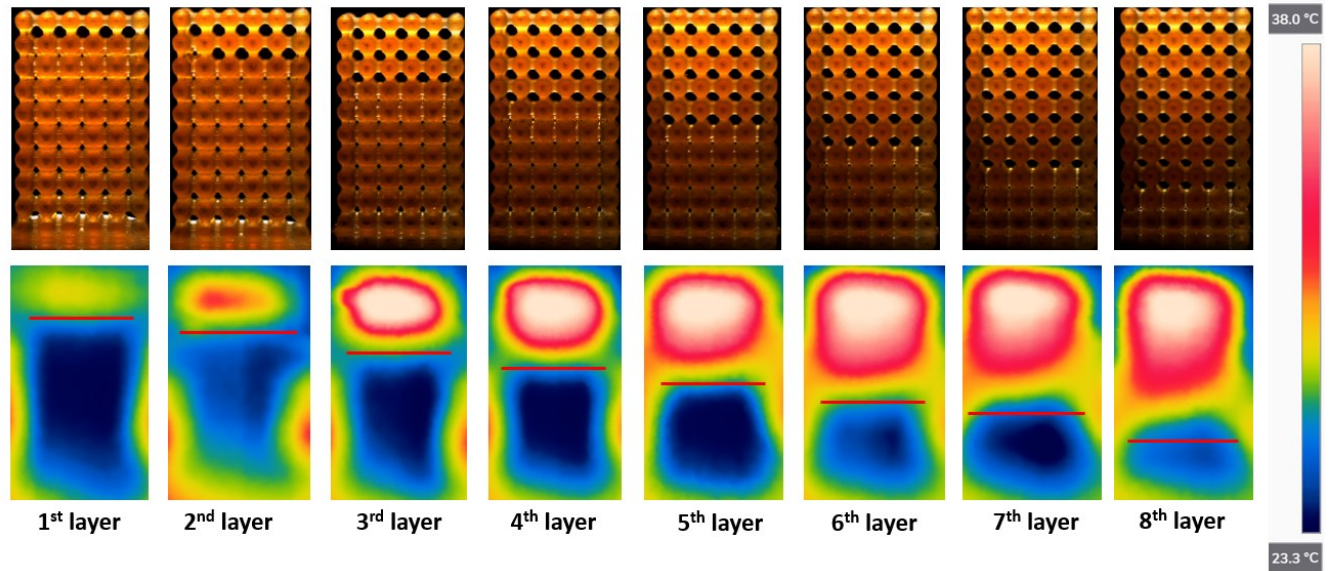


Figure 6.7: Layer by layer thermal gradient while evaporation of water from 3D-printed structure-1

Table 6.4: Temperature and heat flux in different layers of the 3D-printed structures

Layers	Temperature, ($T_s = T_w$), K	Heat flux (Q_{solar}), W/m ²
1	297	1000
2	298	990
3	298	980
4	299	970
5	299	960
6	300	950
7	301	940
8	302	930
9	302	920
10	302	910

The following equation was used to calculate evaporative rate for all layers:

$$\dot{m}_{i..n} = \left[(1 - \varphi)A\alpha Q_{solar\ i..n} - A(1 - \varphi) \frac{\sigma(T_{s\ i..n}^4 - T_{\infty}^4)}{\left[\frac{1}{\epsilon_s} + \frac{1}{\epsilon_a} - 1\right]} \right. \\ \left. - A\varphi \frac{\sigma(T_{w\ i..n}^4 - T_{\infty}^4)}{\left[\frac{1}{\epsilon_w} + \frac{1}{\epsilon_a} - 1\right]} - h_{conv}A\varphi(T_{w\ i..n} - T_{\infty}) \right. \\ \left. - K_{eff}A \left(\frac{T_{s\ i..n} - T_{B\ i..n}}{L} \right) \right] / \varphi h_{lg} \quad (6.10)$$

where, i is layer 1 and n is layer 10. Due to the small distance between top and bottom surface of each layer (i.e., 1.43 mm for 3D structure-1 and -2, and 2 mm for 3D structure-3), the temperature difference, (i.e., $T_s - T_B$) were measured as 0.5 K for each layer.

Figure 6.8, Figure 6.9, and Figure 6.10 demonstrate the evaporation rates for the three 3D structures. All three structures experienced a period of constant rate of evaporation and then the evaporation rate started to decrease. The highest evaporation rate was found for 3D structure-3, approximately 0.005 g/min, and it continued until 80 minutes, and then it started to decrease and experienced falling rate of evaporation (Figure 6.10). The larger evaporation rate was associated with a larger surface area (125.21 mm²) and smaller effective pore size (0.16 mm) which resulted in extended period of constant evaporation rate. The evaporation rate in constant period were similar for 3D structure-1 and 3D structure-2 (e.g., 0.0025-0.003 g/min), but the constant rate period lasted longer in 3D structure-2 (e.g., approximately 90 minutes) than in 3D structure-1 (e.g., approximately 70 minutes). Due to the larger void fraction, 3D structure-1 held more water than the others and it took the longer time (e.g., approximately 250 minutes) to evaporate water. The steady-state evaporation data from the modeling were also plotted in the same graph. Due to assumption of steady state heat transfer, the data followed similar trend though in 3D structure-2

and 3D structure-3, the data from model matched better with the experimental data than 3D structure-1.

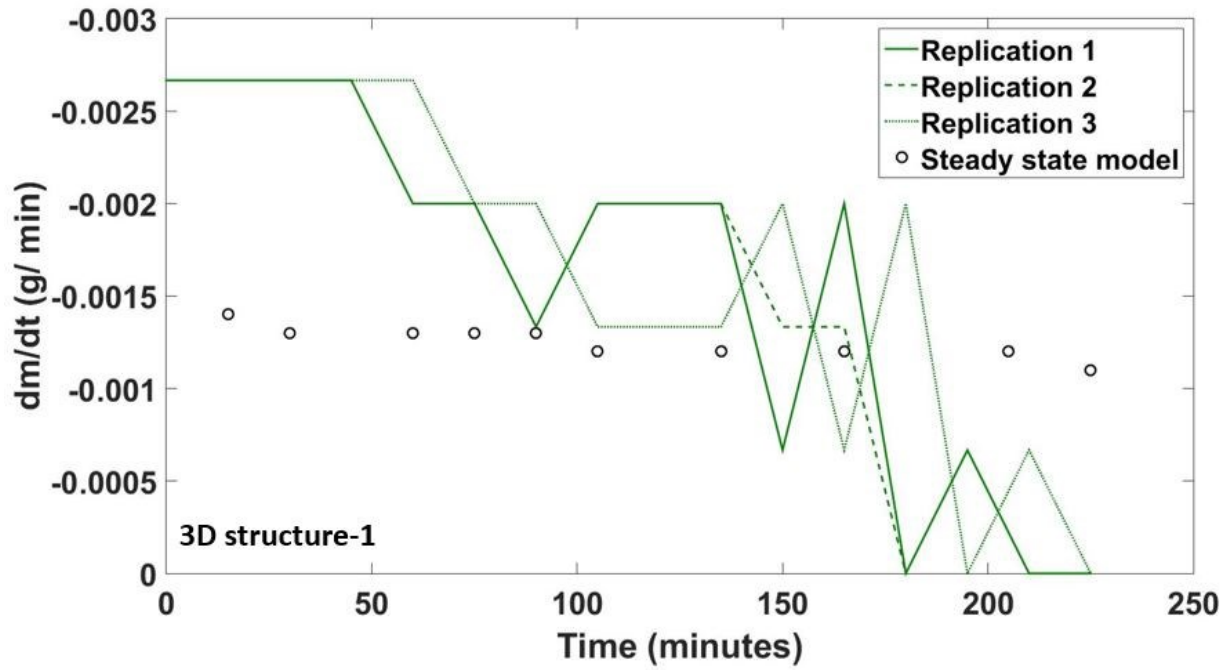


Figure 6.8: Evaporation rate (dm/dt) in g/min for 3D structure-1

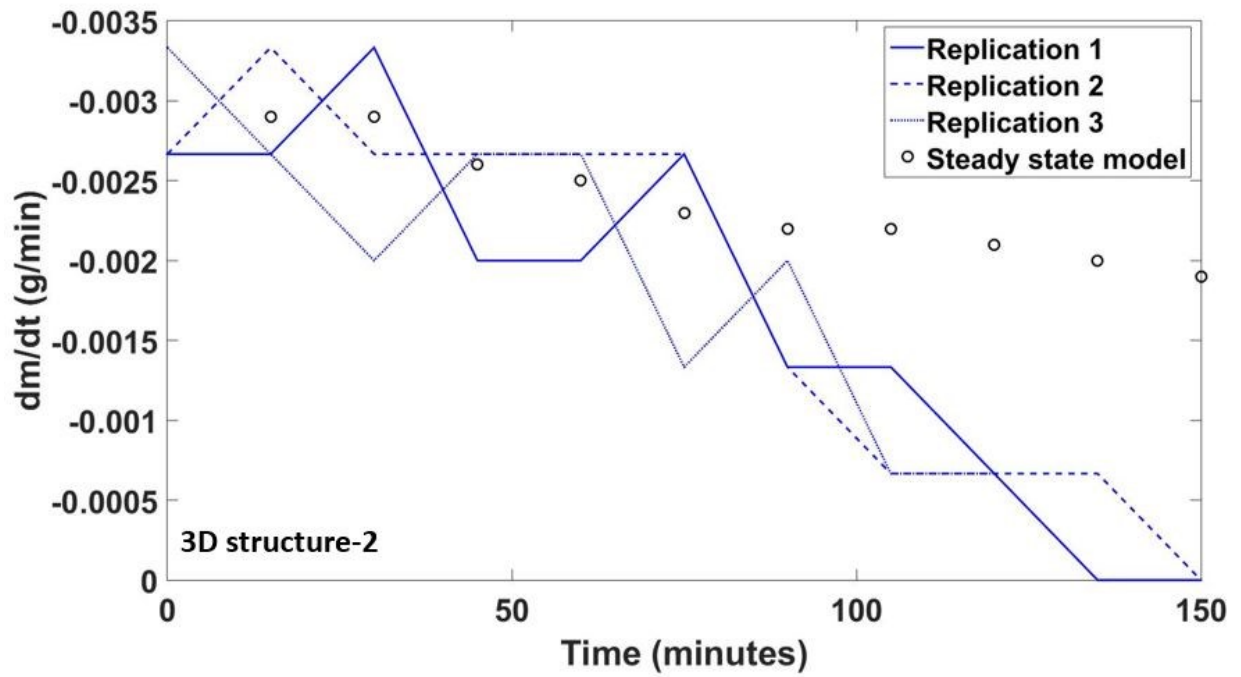


Figure 6.9: Evaporation rate (dm/dt) in g/min for 3D structure-2

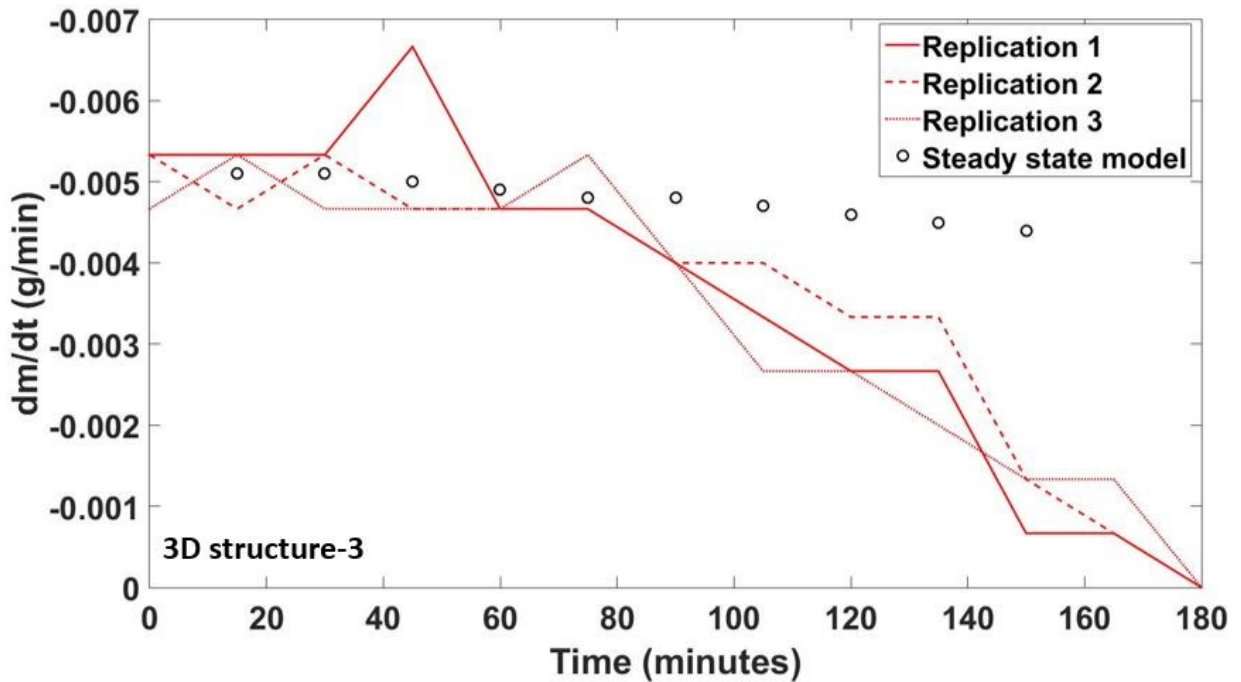


Figure 6.10: Evaporation rate (dm/dt) in g/min for 3D structure-3

Chapter 7 - Conclusions and future works

7.1 Conclusions

This study aimed to analyze consequences of wettability (i.e., hydrophilic, and hydrophobic) on evaporation of water from single and multi-porous media. For single pores, a simulated soil pore was created using three hydrophilic glass or hydrophobic Teflon pores of same sizes (2.38-mm-diameter) and 4- μ L water droplet was evaporated from the soil pore with different relative humidities (30%, 45%, 60% and 75%). Different pore sizes were also evaluated by changing the center-to-center distances of the spheres (e.g., 3.1 mm, 3.13 mm, 2.7 mm and 2.8 mm). Droplet pinning and depinning phenomena in hydrophilic and hydrophobic pores were evaluated. During evaporation, the whole droplet broke up due to evaporative mass loss and formed a liquid island between two of the three spheres. The formation of liquid island, deformation of radius of curvature of the liquid island, contact angle dynamics and rupture energy needed to break up the liquid island were also analyzed. For evaporation from single pores, the following conclusions can be made:

- The relative humidity directly affected the evaporation of droplet from single pore. As example, for 45% RH, evaporation rate was 1.3 and 1.44 times higher in glass and Teflon than 60% RH.
- Since glass is hydrophilic, the evaporation rate in glass was 1.11 and 1.23 times higher than Teflon for 45% and 60% RH, respectively.
- For an isothermal situation at 22.2° C, the liquid island formed between two spheres and experienced a decrease in radius of curvature from both sides, and the radius of curvature decreased gradually until breakup of liquid island.

- For same relative humidity (i.e., 60% RH), the pore size of single pore affected the evaporation rate. At 60% RH, the evaporation rate was 1.23 and 1.3 times higher with larger pore (i.e., center-to-center distance of 3.1 mm) than the smaller (i.e., center-to-center distances were 2.7 and 2.8 mm) for glass and Teflon respectively.
- The initial rupture strength to break up the liquid islands were greater in Teflon pores (i.e., 177 μN and 215 μN) than glass pores (i.e., 170 μN and 212 μN) and they decreased gradually until the breakup of whole droplet.
- The solid-liquid-vapor contact lines were pinned in one sphere in glass pore and decreased in the other two, while in Teflon, all the three solid-liquid-vapor contact lines experienced depinning (i.e., the lines decreased until the breakup of liquid droplet).
- The curvature of the liquid-vapor interface prior to rupture increased in glass and Teflon pores from beginning of evaporation until breakup at both 30% and 75% RH. The ultimate curvature of the liquid-vapor interface just before breakup was found higher in glass than Teflon at both 30% and 75% RH.

In evaporation from porous columns, two sets of experiments were conducted. First, small hydrophilic simulated soil columns were prepared by filling a 2-cm diameter and 3-cm high glass beaker filled with 1720 borosilicate glass spheres of same sizes (2-mm-diameter) and 5.5 mL of water was evaporated from the porous column with 1500 W/m^2 heat flux projected on top with a solar simulator. The evaporative drying front's propagation were visualized with x-ray imaging to understand the liquid dynamics during evaporation from a porous column. The following conclusions can be made from that experiment:

- Due to uniformity of the porous sample (i.e., similar sized spheres), the constant rate period was insignificant or absent; rather, the sample experienced a sharp decrease in evaporation denoted as falling rate period followed by slower rate of evaporation.
- The evaporation rate decreased from maximum of 0.03 mm/min to 0.0064 mm/min until 625 minutes where the evaporation rate was stabilized until the 1300th minute. From the beginning of the experiments until the 1300th minute, evaporation was in the falling rate period and 3.84 g of water (approximately 70% of total water) was evaporated during that time
- After the 1800th minute, the evaporation entered slower rate period and continued until the end. After slower rate period, only 0.6 g of water was evaporated until the end of evaporation.

In evaporation from hydrophilic and hydrophobic porous columns created with approximately 1165 glass or Teflon spheres (2.38-mm-diameter) filled in two 6-cm-height, 1.88-cm-diameter glass beakers, the experiment was conducted for seven days, and each experiment was replicated five times with application of 1000 W/m² heat flux applied from the top. The following conclusions can be made from this experiment:

- After seven days of experiment, approximately 25% more water was evaporated from glass (i.e., 3 g) than Teflon sample (i.e., 2.4 g).
- Due to homogeneity, the constant period of evaporation was insignificant in both samples and from the beginning, evaporation experienced a sharp decrease initiating the falling rate of evaporation. After that, evaporation entered into diffusion controlled slower rate period with negligible evaporation rate (i.e., 0-1 mm/day).

- The drying front propagated faster in glass than Teflon sample and after seven days, drying front depths were greater in glass (i.e., 30 mm) than Teflon (i.e., 24 mm).
- Due to its wettability, the glass sample was susceptible to form more liquid islands creating a hydraulic connection between saturated and unsaturated parts which led to higher evaporation rate than Teflon.

Three 3D-printed structures were created with hydrophilic, translucent ABS material with different sizes and shapes to study evaporation of water with the application of external heat flux. The steady-state heat transfer analysis was modeled to predict evaporation rates. The following conclusion could be drawn from this experiment:

- 3D structure-3 experienced the sharpest decrease in the evaporative mass loss as the water evaporated from 0.8 g to approximately 0.1 g within 180 minutes. 3D structures 1 and 2 experienced similar trends in evaporative mass loss as both the structures were nearly identical.
- 3D structure-1 had greater water holding capacity compared to 3D structure-1 due to higher porosity
- Drying fronts calculated from the transient saturation and measured from high-speed imaging with ImageJ matched well and significantly.
- The heat transfer model predicting the evaporative mass loss matched with the experimental data in the beginning (i.e., when the evaporation was in constant rate period). But due to transient mode of heat transfer, the model did not coincide well the experimental data at the later part of evaporation.

The major contributions and uniqueness of this work lies in analyzing evaporation dynamics from single pores, and applying the knowledge in evaluating evaporation phenomena

from porous media at larger scales. In previous studies, single pore research was confined to the evaluation of liquid islands formed between two spheres [111, 118], and analyzing the capillary effects and rupture strength of the liquid islands [102, 105, 106, 116]. In contrast, in this study, the droplet formation and liquid island formation after breakup of whole droplets were analyzed for single pores created with three spheres. In addition, the effects of wettability (i.e., hydrophilic and hydrophobic) on small droplets in single pores was studied. The effects of wettability on droplet rupture, liquid island formation and subsequent rupture of the liquid islands were also investigated thoroughly in this study with respect to some pore geometry and air relative humidities (RH). Subsequently, the knowledge was applied to distinguish evaporation stages in hydrophilic and hydrophobic porous columns. The nature of liquid island formation and subsequent creation of hydraulic connections in a porous column were also analyzed with the information gained from single pore experiments.

7.2 Future works

In this study, the analysis of evaporation of single pore and multi-porous columns with the impacts of wettability was evaluated. The wettability influenced the evaporation process, as the evaporation rate was significantly lower from hydrophobic media than hydrophilic media for both single pores and porous columns. The fundamental findings of the study can be applied where inclusion of hydrophobicity can restrict evaporation from soil and the soil water conservation can be estimated. This study can also be used to develop new models to predict restrictive evaporation and increasing soil water yields. Some of the future research opportunities are as follows:

- Develop a transient heat and mass transfer model with inclusion of wettability factor to predict soil-water evaporation and numerical modeling of evaporation from porous media with mixed wettability.

- Use of bio-surfactant to alter the surface tension of water in soil and increase water availability of soil. During application of bio-surfactants, how the surfactant droplets penetrate the soil surface can be an important phenomenon to be studied. In further investigation, inclusion of hydrophobicity on the top surface of the soil to conserve the under-water bio-surfactants could be another significant study that can help soil-water conservation, restrict evaporation, increasing water yields and decreasing irrigation demands.

Nomenclature

A	Surface Area [m^2]
a	Separation distance [m]
C	Concentration [kg/m^3]
Ca	Capillary number [-]
d	Diameter [m]
d_c	Critical diameter [m]
D	Mass diffusivity [m^2/s]
E	Evaporation rate [mm/day]
F	Formation factor
g	Acceleration due to gravity [m/s^2]
H	Height of sample [m or mm]
h	Convective heat transfer coefficient, [W/m^2-K]
h_m	Mass transfer coefficient [m/s]
I	Attenuated x-ray intensity
J	Diffusive flux [kg/m^2-s]
k	Permeability [m^2]
K_a	Thermal conductivity of air [$W/m-K$]
K_s	Thermal conductivity of solid [$W/m-K$]
K_w	Thermal conductivity of water [$W/m-K$]
L_c	Characteristic length [m or mm]
L_D	Drying front depth [m or mm]

M	Molar mass [mol]
m	Mass [g or kg]
Nu	Nusselt Number [-]
P	Pressure [Pa]
Q	Flow rate [m^3/s]
Q_{solar}	Solar heat flux [W/m^2]
RH	Relative humidity [%]
Ra	Rayleigh number [-]
R	Radius [m or mm]
V	Volume [L or m^3]

Greek symbols

α	Thermal diffusivity [m^2/s]
Λ	Characteristic pore radius [m or mm]
β	Thermal expansion coefficient [K^{-1}]
γ	Interfacial tension [N/m]
δ	Thermal boundary layer thickness [m or mm]
ϵ	Emissivity
η	Attenuation coefficient
θ_{CA}	Contact angle [$^\circ$]
κ	Curvature [m^{-1}]
ν	Kinematic viscosity [m^2s^{-1}]
ρ	Density [kg/m^3]
σ	Stefan-Boltzman constant [W/m^2K^4]

φ	Porosity [%]
μ	Dynamic viscosity [<i>Pa-s</i>]

Subscripts

<i>w</i>	Water
<i>s</i>	Solid
<i>f</i>	Fluid
<i>a</i>	Air
<i>v</i>	Vapor
<i>sat</i>	Saturated

References

1. D'Odorico, P., et al., *The global food-energy-water nexus*. Reviews of geophysics, 2018. **56**(3): p. 456-531.
2. Najafi, E. and R. Khanbilvardi. *Evaluating global crop distribution in the 21st century to maximize food production*. in *AGU Fall Meeting Abstracts*. 2019.
3. Alexandratos, N. and J. Bruinsma, *World agriculture towards 2030/2050: the 2012 revision*. 2012.
4. Yang, Y.E., et al., *Modeling the agricultural water–energy–food nexus in the Indus River Basin, Pakistan*. Journal of Water Resources Planning and Management, 2016. **142**(12): p. 04016062.
5. Aquastat, F., *FAO's information system on water and agriculture*. Food and Agriculture Organization of the United Nations (FAO), Rome, Italy, 2011.
6. Hornbeck, R. and P. Keskin, *The historically evolving impact of the ogallala aquifer: Agricultural adaptation to groundwater and drought*. American Economic Journal: Applied Economics, 2014. **6**(1): p. 190-219.
7. Chow, A., E.A. Khosa, and A. Ko, *A Drying Shame: The Ogallala Aquifer*.
8. Steward, D.R., et al., *Tapping unsustainable groundwater stores for agricultural production in the High Plains Aquifer of Kansas, projections to 2110*. Proceedings of the National Academy of Sciences, 2013. **110**(37): p. E3477-E3486.
9. de Vito, R., et al., *An index-based approach for the sustainability assessment of irrigation practice based on the water-energy-food nexus framework*. Advances in Water Resources, 2017. **110**: p. 423-436.
10. Butler Jr, J., et al., *Interpretation of water level changes in the High Plains aquifer in western Kansas*. Groundwater, 2013. **51**(2): p. 180-190.
11. Or, D., et al., *Advances in soil evaporation physics—A review*. Vadose Zone Journal, 2013. **12**(4): p. 1-16.
12. Shokri, N., P. Lehmann, and D. Or, *Characteristics of evaporation from partially wettable porous media*. Water Resources Research, 2009. **45**(2).
13. Shokri, N., P. Lehmann, and D. Or, *Critical evaluation of enhancement factors for vapor transport through unsaturated porous media*. Water resources research, 2009. **45**(10).
14. Shokri, N., et al., *Drying front and water content dynamics during evaporation from sand delineated by neutron radiography*. Water resources research, 2008. **44**(6).
15. Aboufoul, M., et al., *Dynamics of water evaporation from porous asphalt*. Construction and Building Materials, 2019. **202**: p. 406-414.
16. Shokri, N., P. Lehmann, and D. Or, *Effects of hydrophobic layers on evaporation from porous media*. Geophysical Research Letters, 2008. **35**(19).
17. Shokri, N., P. Lehmann, and D. Or, *Evaporation from layered porous media*. Journal of Geophysical Research: Solid Earth, 2010. **115**(B6).
18. Shokri, N., M. Sahimi, and D. Or, *Morphology, propagation dynamics and scaling characteristics of drying fronts in porous media*. Geophysical Research Letters, 2012. **39**(9).
19. Bachmann, J., R. Horton, and R. Van der Ploeg, *Isothermal and nonisothermal evaporation from four sandy soils of different water repellency*. Soil Science Society of America Journal, 2001. **65**(6): p. 1599-1607.

20. Davis, D.D., et al., *Wettability and hysteresis effects on water sorption in relatively dry soil*. Soil Science Society of America Journal, 2009. **73**(6): p. 1947-1951.
21. Philip, J. and D. De Vries, *Moisture movement in porous materials under temperature gradients*. Eos, Transactions American Geophysical Union, 1957. **38**(2): p. 222-232.
22. De Vries, D., *Simultaneous transfer of heat and moisture in porous media*. Eos, Transactions American Geophysical Union, 1958. **39**(5): p. 909-916.
23. Chen, C., et al., *Evaporation with the formation of chains of liquid bridges*. Journal of Fluid Mechanics, 2018. **837**: p. 703-728.
24. Alowaisy, A. and N. Yasufuku, *Characteristics of the second stage of evaporation and water redistribution through double layered sandy soil profiles*. Lowland Technology International, 2018. **20**(3, Dec): p. 273-284.
25. Ghanbarian, B., *Applications of critical path analysis to uniform grain packings with narrow conductance distributions: I. Single-phase permeability*. Advances in Water Resources, 2020. **137**: p. 103529.
26. Glover, P. and E. Walker, *Grain-size to effective pore-size transformation derived from electrokinetic theory*. Geophysics, 2009. **74**(1): p. E17-E29.
27. Glover, P., I. Zadjali, and K. Frew, *Permeability prediction from MICP and NMR data using an electrokinetic approach: Geophysics*. 2006.
28. Shokri, N. and D. Or, *What determines drying rates at the onset of diffusion controlled stage-2 evaporation from porous media?* Water Resources Research, 2011. **47**(9).
29. Lehmann, P., S. Assouline, and D. Or, *Characteristic lengths affecting evaporative drying of porous media*. Physical Review E, 2008. **77**(5): p. 056309.
30. Chakraborty, P.P. and M.M. Derby, *Contact Line Pinning and Depinning Prior to Rupture of an Evaporating Droplet in a Simulated Soil Pore*. International Conference on Nanochannels, Microchannels, and Minichannels, 2020. **83693**.
31. Chakraborty, P.P. and M.M. Derby, *Evaporation From a Simulated Soil Pore: Effects of Relative Humidity*. International Conference on Nanochannels, Microchannels, and Minichannels, 2018. **51197**.
32. Cengel, Y.A. and A.J. Ghajar, *Heat and mass transfer. A practical approach*, 2007.
33. Incropera, F.P., et al., *Fundamentals of heat and mass transfer*. 2007: Wiley.
34. Birdi, K., D. Vu, and A. Winter, *A study of the evaporation rates of small water drops placed on a solid surface*. The Journal of physical chemistry, 1989. **93**(9): p. 3702-3703.
35. Deegan, R.D., et al., *Contact line deposits in an evaporating drop*. Physical review E, 2000. **62**(1): p. 756.
36. Erbil, H.Y., *Evaporation of pure liquid sessile and spherical suspended drops: A review*. Advances in colloid and interface science, 2012. **170**(1-2): p. 67-86.
37. Hu, H. and R.G. Larson, *Evaporation of a sessile droplet on a substrate*. The Journal of Physical Chemistry B, 2002. **106**(6): p. 1334-1344.
38. Nguyen, T.A., et al., *Theoretical and experimental analysis of droplet evaporation on solid surfaces*. Chemical engineering science, 2012. **69**(1): p. 522-529.
39. Orejon, D., K. Sefiane, and M.E. Shanahan, *Stick-slip of evaporating droplets: substrate hydrophobicity and nanoparticle concentration*. Langmuir, 2011. **27**(21): p. 12834-12843.
40. Uno, K., et al., *Particle adsorption in evaporating droplets of polymer latex dispersions on hydrophilic and hydrophobic surfaces*. Colloid and polymer science, 1998. **276**(9): p. 810-815.

41. Yu, H.Z., et al., *Evaporation of Water Microdroplets on Self-Assembled Monolayers: From Pinning to Shrinking*. ChemPhysChem, 2004. **5**(7): p. 1035-1038.
42. Park, J. and J. Moon, *Control of colloidal particle deposit patterns within picoliter droplets ejected by ink-jet printing*. Langmuir, 2006. **22**(8): p. 3506-3513.
43. Carroll, G.T., et al., *Photochemical micropatterning of carbohydrates on a surface*. Langmuir, 2006. **22**(6): p. 2899-2905.
44. Calvert, P., *Inkjet printing for materials and devices*. Chemistry of materials, 2001. **13**(10): p. 3299-3305.
45. Yu, Y., et al., *Evaporation and coverage area of pesticide droplets on hairy and waxy leaves*. biosystems engineering, 2009. **104**(3): p. 324-334.
46. Jia, W. and H.-H. Qiu, *Experimental investigation of droplet dynamics and heat transfer in spray cooling*. Experimental Thermal and Fluid Science, 2003. **27**(7): p. 829-838.
47. Dugas, V., J. Broutin, and E. Souteyrand, *Droplet evaporation study applied to DNA chip manufacturing*. Langmuir, 2005. **21**(20): p. 9130-9136.
48. Bensimon, D., et al., *Stretching DNA with a receding meniscus: experiments and models*. Physical review letters, 1995. **74**(23): p. 4754.
49. Khrustalev, D. and A. Faghri, *Heat transfer during evaporation on capillary-grooved structures of heat pipes*. 1995.
50. Mantelli, M.H., *Development of porous media thermosyphon technology for vapor recovering in cross-current cooling towers*. Applied Thermal Engineering, 2016. **108**: p. 398-413.
51. Saneinejad, S., et al., *Coupled CFD, radiation and porous media transport model for evaluating evaporative cooling in an urban environment*. Journal of Wind Engineering and Industrial Aerodynamics, 2012. **104**: p. 455-463.
52. Hanlon, M. and H. Ma, *Evaporation heat transfer in sintered porous media*. J. Heat Transfer, 2003. **125**(4): p. 644-652.
53. Li, Y., H.-f. He, and Z.-x. Zeng, *Evaporation and condensation heat transfer in a heat pipe with a sintered-grooved composite wick*. Applied Thermal Engineering, 2013. **50**(1): p. 342-351.
54. Purlis, E., *Modelling convective drying of foods: A multiphase porous media model considering heat of sorption*. Journal of food engineering, 2019. **263**: p. 132-146.
55. Chapuis, O., et al., *Two-phase flow and evaporation in model fibrous media: Application to the gas diffusion layer of PEM fuel cells*. Journal of Power Sources, 2008. **178**(1): p. 258-268.
56. Médici, E.F. and J.S. Allen, *Evaporation, two phase flow, and thermal transport in porous media with application to low-temperature fuel cells*. International Journal of Heat and Mass Transfer, 2013. **65**: p. 779-788.
57. Shin, D.H., et al., *Evaporating characteristics of sessile droplet on hydrophobic and hydrophilic surfaces*. Microelectronic Engineering, 2009. **86**(4-6): p. 1350-1353.
58. Kwok, D., et al., *Contact angle measurements and contact angle interpretation. 1. Contact angle measurements by axisymmetric drop shape analysis and a goniometer sessile drop technique*. Langmuir, 1997. **13**(10): p. 2880-2894.
59. Chakraborty, P.P., et al., *Evaporation From Simulated Soil Pores: Effects of Wettability, Liquid Islands, and Breakup*. Interfacial Phenomena and Heat Transfer, 2018. **6**(4).
60. Nachshon, U., et al., *Combined evaporation and salt precipitation in homogeneous and heterogeneous porous media*. Water Resources Research, 2011. **47**(3).

61. Imeson, A., et al., *The effects of fire and water repellency on infiltration and runoff under Mediterranean type forest*. Catena, 1992. **19**(3-4): p. 345-361.
62. Robichaud, P.R., *Fire effects on infiltration rates after prescribed fire in Northern Rocky Mountain forests, USA*. Journal of Hydrology, 2000. **231**: p. 220-229.
63. Kiesevalter, H.T., et al., *Secondary metabolites of Bacillus subtilis impact the assembly of soil-derived semisynthetic bacterial communities*. Beilstein journal of organic chemistry, 2020. **16**(1): p. 2983-2998.
64. Lowe, M.-A., et al., *Bacillus subtilis and surfactant amendments for the breakdown of soil water repellency in a sandy soil*. Geoderma, 2019. **344**: p. 108-118.
65. Phulpoto, I.A., et al., *Production and characterization of surfactin-like biosurfactant produced by novel strain Bacillus nealsonii S2MT and it's potential for oil contaminated soil remediation*. Microbial cell factories, 2020. **19**(1): p. 1-12.
66. Sachdev, D.P. and S.S. Cameotra, *Biosurfactants in agriculture*. Applied microbiology and biotechnology, 2013. **97**(3): p. 1005-1016.
67. Belnap, J. and O.L. Lange, *Biological soil crusts: structure, function, and management*. Vol. 150. 2001: Springer.
68. Kotoky, R. and P. Pandey, *Rhizosphere mediated biodegradation of benzo (A) pyrene by surfactin producing soil bacilli applied through Melia azedarach rhizosphere*. International Journal of Phytoremediation, 2020. **22**(4): p. 363-372.
69. Drelich, J., et al., *Hydrophilic and superhydrophilic surfaces and materials*. Soft Matter, 2011. **7**(21): p. 9804-9828.
70. Joanny, J. and P.-G. De Gennes, *A model for contact angle hysteresis*. The journal of chemical physics, 1984. **81**(1): p. 552-562.
71. Yuan, Y. and T.R. Lee, *Contact angle and wetting properties*, in *Surface science techniques*. 2013, Springer. p. 3-34.
72. Lourenço, S., et al., *Soil wettability in ground engineering: fundamentals, methods, and applications*. Acta Geotechnica, 2018. **13**(1): p. 1-14.
73. Wenzel, R.N., *Resistance of solid surfaces to wetting by water*. Industrial & Engineering Chemistry, 1936. **28**(8): p. 988-994.
74. Cassie, A. and S. Baxter, *Wettability of porous surfaces*. Transactions of the Faraday society, 1944. **40**: p. 546-551.
75. Ahmad, D., et al., *Hydrophilic and hydrophobic materials and their applications*. Energy Sources, Part A: Recovery, Utilization, and Environmental Effects, 2018. **40**(22): p. 2686-2725.
76. Drelich, J. and E. Chibowski, *Superhydrophilic and superwetting surfaces: definition and mechanisms of control*. Langmuir, 2010. **26**(24): p. 18621-18623.
77. Ueda, E. and P.A. Levkin, *Emerging applications of superhydrophilic-superhydrophobic micropatterns*. Advanced Materials, 2013. **25**(9): p. 1234-1247.
78. Jiang, L., Y. Zhao, and J. Zhai, *A lotus-leaf-like superhydrophobic surface: a porous microsphere/nanofiber composite film prepared by electrohydrodynamics*. Angewandte Chemie, 2004. **116**(33): p. 4438-4441.
79. Fang, X., et al., *Dewetting of the three-phase contact line on solids*. Langmuir, 2010. **26**(11): p. 7682-7685.
80. Fang, X., et al., *Factors controlling the drop evaporation constant*. The Journal of Physical Chemistry B, 2005. **109**(43): p. 20554-20557.

81. Liu, L., et al., *Evaporation of a sessile water droplet during depressurization*. International Journal of Thermal Sciences, 2021. **159**: p. 106587.
82. Kim, J.-H., et al., *Evaporation of water droplets on polymer surfaces*. Langmuir, 2007. **23**(11): p. 6163-6169.
83. Wang, Y. and Z.-g. Wang, *Sessile droplet freezing on polished and micro-micro-hierarchical silicon surfaces*. Applied Thermal Engineering, 2018. **137**: p. 66-73.
84. Derby, M.M., et al., *Flow condensation heat transfer enhancement in a mini-channel with hydrophobic and hydrophilic patterns*. International Journal of Heat and Mass Transfer, 2014. **68**: p. 151-160.
85. Chen, X. and M.M. Derby. *Visualization of Steam Flow Condensation in Hydrophobic and Hydrophilic Mini-Gaps*. in *ASME International Mechanical Engineering Congress and Exposition*. 2015. American Society of Mechanical Engineers.
86. Betz, A.R., et al., *Do surfaces with mixed hydrophilic and hydrophobic areas enhance pool boiling?* Applied Physics Letters, 2010. **97**(14): p. 141909.
87. Kadhim, M.A., et al., *Experimental and theoretical investigation of droplet evaporation on heated hydrophilic and hydrophobic surfaces*. Langmuir, 2019. **35**(19): p. 6256-6266.
88. Cioulachtjian, S., et al., *Experimental investigation of water drop evaporation under moist air or saturated vapour conditions*. International journal of thermal sciences, 2010. **49**(6): p. 859-866.
89. Bormashenko, E., A. Musin, and M. Zinigrad, *Evaporation of droplets on strongly and weakly pinning surfaces and dynamics of the triple line*. Colloids and Surfaces A: Physicochemical and Engineering Aspects, 2011. **385**(1-3): p. 235-240.
90. Armstrong, S., et al., *Pinning-free evaporation of sessile droplets of water from solid surfaces*. Langmuir, 2019. **35**(8): p. 2989-2996.
91. Gatapova, E.Y., et al., *Evaporation of a sessile water drop on a heated surface with controlled wettability*. Colloids and Surfaces A: Physicochemical and Engineering Aspects, 2014. **441**: p. 776-785.
92. Dash, S. and S.V. Garimella, *Droplet evaporation on heated hydrophobic and superhydrophobic surfaces*. Physical Review E, 2014. **89**(4): p. 042402.
93. Ramos, S., J. Dias, and B. Canut, *Drop evaporation on superhydrophobic PTFE surfaces driven by contact line dynamics*. Journal of colloid and interface science, 2015. **440**: p. 133-139.
94. Dhavaleswarapu, H.K., et al., *Experimental investigation of evaporation from low-contact-angle sessile droplets*. Langmuir, 2010. **26**(2): p. 880-888.
95. Dunn, G., et al., *The strong influence of substrate conductivity on droplet evaporation*. Journal of Fluid Mechanics, 2009. **623**: p. 329-351.
96. Fuchs, N.A., *Evaporation and droplet growth in gaseous media*. 2013: Elsevier.
97. Erbil, H.Y., *Control of stain geometry by drop evaporation of surfactant containing dispersions*. Advances in colloid and interface science, 2015. **222**: p. 275-290.
98. Topley, B. and R. Whytlaw-Gray, *LXXX. Experiments on the rate of evaporation of small spheres as a method of determining diffusion coefficients.—The diffusion coefficient of iodine*. The London, Edinburgh, and Dublin Philosophical Magazine and Journal of Science, 1927. **4**(24): p. 873-888.
99. Sefiane, K. and R. Bennacer, *An expression for droplet evaporation incorporating thermal effects*. Journal of Fluid Mechanics, 2011. **667**: p. 260-271.

100. Gao, M., et al., *An experimental investigation of sessile droplets evaporation on hydrophilic and hydrophobic heating surface with constant heat flux*. International Communications in Heat and Mass Transfer, 2017. **88**: p. 262-268.
101. De Bisschop, F.R. and W.J. Rigole, *A physical model for liquid capillary bridges between adsorptive solid spheres: the nodoid of plateau*. Journal of Colloid and Interface Science, 1982. **88**(1): p. 117-128.
102. Gladkyy, A. and R. Schwarze, *Comparison of different capillary bridge models for application in the discrete element method*. Granular Matter, 2014. **16**(6): p. 911-920.
103. Gras, J.-P., J.-Y. Delenne, and M.S. El Youssoufi, *Study of capillary interaction between two grains: a new experimental device with suction control*. Granular Matter, 2013. **15**(1): p. 49-56.
104. Lievano, D., S. Velankar, and J.J. McCarthy, *The rupture force of liquid bridges in two and three particle systems*. Powder Technology, 2017. **313**: p. 18-26.
105. Pitois, O., P. Moucheront, and X. Chateau, *Rupture energy of a pendular liquid bridge*. The European Physical Journal B-Condensed Matter and Complex Systems, 2001. **23**(1): p. 79-86.
106. Rabinovich, Y.I., M.S. Esayanur, and B.M. Moudgil, *Capillary forces between two spheres with a fixed volume liquid bridge: theory and experiment*. Langmuir, 2005. **21**(24): p. 10992-10997.
107. Simons, S., J. Seville, and M. Adams, *An analysis of the rupture energy of pendular liquid bridges*. Chemical Engineering Science, 1994. **49**(14): p. 2331-2339.
108. Wang, J.-P., et al., *Capillary force and rupture of funicular liquid bridges between three spherical bodies*. Powder Technology, 2017. **305**: p. 89-98.
109. Weigert, T. and S. Ripperger, *Calculation of the liquid bridge volume and bulk saturation from the half-filling angle*. Particle & Particle Systems Characterization: Measurement and Description of Particle Properties and Behavior in Powders and Other Disperse Systems, 1999. **16**(5): p. 238-242.
110. Willett, C.D., et al., *Capillary bridges between two spherical bodies*. Langmuir, 2000. **16**(24): p. 9396-9405.
111. Farmer, T.P. and J.C. Bird, *Asymmetric capillary bridges between contacting spheres*. Journal of colloid and interface science, 2015. **454**: p. 192-199.
112. Semprebon, C., et al., *Liquid morphologies and capillary forces between three spherical beads*. Physical Review E, 2016. **94**(1): p. 012907.
113. Rynhart, P., et al., *Solution of the Young-Laplace equation for three particles*. 2003.
114. Urso, M.E.D., C.J. Lawrence, and M.J. Adams, *Pendular, funicular, and capillary bridges: results for two dimensions*. Journal of colloid and interface science, 1999. **220**(1): p. 42-56.
115. Murase, K., et al., *Estimation on the strength of a liquid bridge adhered to three spheres*. Advanced Powder Technology, 2008. **19**(4): p. 349-367.
116. Lambert, P., et al., *Comparison between two capillary forces models*. Langmuir, 2008. **24**(7): p. 3157-3163.
117. Mielniczuk, B., T. Hueckel, and M.S.E. Youssoufi, *Evaporation-induced evolution of the capillary force between two grains*. Granular Matter, 2014. **16**(5): p. 815-828.
118. Rossetti, D., X. Pepin, and S.J. Simons, *Rupture energy and wetting behavior of pendular liquid bridges in relation to the spherical agglomeration process*. Journal of colloid and interface science, 2003. **261**(1): p. 161-169.

119. Hillel, D., *Environmental soil physics: Fundamentals, applications, and environmental considerations*. 1998: Elsevier.
120. Cejas, C.M., et al., *Experimental investigation of water distribution in a two-phase zone during gravity-dominated evaporation*. *Physical Review E*, 2017. **96**(6): p. 062908.
121. Kumar, N. and J.H. Arakeri, *Evaporation from layered porous medium in the presence of infrared heating*. *Water Resources Research*, 2018. **54**(10): p. 7670-7687.
122. Kumar, N. and J.H. Arakeri, *Evaporation from confined porous media due to controlled IR heating from above*. *Transport in Porous Media*, 2018. **125**(2): p. 311-340.
123. Kumar, N. and J.H. Arakeri, *Investigation on the effect of temperature on evaporative characteristic length of a porous medium*. *Drying Technology*, 2019.
124. Kumar, N. and J.H. Arakeri, *Mimicking some features of a root-soil system by dual porosity media*. *Agricultural Water Management*, 2020. **227**: p. 105855.
125. Mahmoudi, A.H., F. Hoffmann, and B. Peters, *Application of XDEM as a novel approach to predict drying of a packed bed*. *International Journal of Thermal Sciences*, 2014. **75**: p. 65-75.
126. Okuyama, K., S. Kawanishi, and R. Aoki, *Onset of drying of a porous particle bed immersed in saturated water and heated with a high surface heat flux*. *Applied Thermal Engineering*, 2020. **176**: p. 115358.
127. Peeters, R., et al., *Non-Isothermal Kinetic Model of Water Vapor Adsorption on a Desiccant Bed for Harvesting Water from Atmospheric Air*. *Industrial & Engineering Chemistry Research*, 2021. **60**(31): p. 11812-11823.
128. Prommas, R., *Theoretical and experimental study of heat and mass transfer mechanism during convective drying of multi-layered porous packed bed*. *International Communications in Heat and Mass Transfer*, 2011. **38**(7): p. 900-905.
129. Ranzinger, F., et al., *Quantification of evaporation and drainage processes in unsaturated porous media using magnetic resonance imaging*. *Water Resources Research*, 2020. **56**(2): p. e2019WR026658.
130. Yiotis, A., et al., *Drying in porous media with gravity-stabilized fronts: Experimental results*. *Physical Review E*, 2012. **86**(2): p. 026310.
131. Cejas, C.M., et al., *Effect of granular packing geometry on evaporation*. arXiv preprint arXiv:1601.04584, 2016.
132. Chapuis, O. and M. Prat, *Influence of wettability conditions on slow evaporation in two-dimensional porous media*. *Physical review E*, 2007. **75**(4): p. 046311.
133. Ceballos, L. and M. Prat, *Slow invasion of a fluid from multiple inlet sources in a thin porous layer: influence of trapping and wettability*. *Physical Review E*, 2013. **87**(4): p. 043005.
134. Cruz, B.C., et al., *Pore-scale water dynamics during drying and the impacts of structure and surface wettability*. *Water Resources Research*, 2017. **53**(7): p. 5585-5600.
135. Chraïbi, H., M. Prat, and O. Chapuis, *Influence of contact angle on slow evaporation in two-dimensional porous media*. *Physical Review E*, 2009. **79**(2): p. 026313.
136. Prat, M., *Pore network models of drying, contact angle, and film flows*. *Chemical engineering & technology*, 2011. **34**(7): p. 1029-1038.
137. Kuttanikkad, S.P., M. Prat, and J. Pauchet, *Pore-network simulations of two-phase flow in a thin porous layer of mixed wettability: application to water transport in gas diffusion layers of proton exchange membrane fuel cells*. *Journal of Power Sources*, 2011. **196**(3): p. 1145-1155.

138. Yiotis, A., et al., *Effect of liquid films on the drying of porous media*. AIChE Journal, 2004. **50**(11): p. 2721-2737.
139. Yiotis, A.G., et al., *Pore-network study of the characteristic periods in the drying of porous materials*. Journal of colloid and interface science, 2006. **297**(2): p. 738-748.
140. Metzger, T., A. Irawan, and E. Tsotsas, *Influence of pore structure on drying kinetics: A pore network study*. AIChE Journal, 2007. **53**(12): p. 3029-3041.
141. Prat, M., *Recent advances in pore-scale models for drying of porous media*. Chemical engineering journal, 2002. **86**(1-2): p. 153-164.
142. Prat, M. and F. Bouleux, *Drying of capillary porous media with a stabilized front in two dimensions*. Physical Review E, 1999. **60**(5): p. 5647.
143. Vorhauer, N., et al., *Drying with formation of capillary rings in a model porous medium*. Transport in Porous Media, 2015. **110**(2): p. 197-223.
144. Yiotis, A., et al., *Pore-network modeling of isothermal drying in porous media*, in *Upscaling Multiphase Flow in Porous Media*. 2005, Springer. p. 63-86.
145. Yiotis, A.G., et al., *A 2-D pore-network model of the drying of single-component liquids in porous media*. Advances in Water Resources, 2001. **24**(3-4): p. 439-460.
146. Borgman, O., et al., *Impact of spatially correlated pore-scale heterogeneity on drying porous media*. Water Resources Research, 2017. **53**(7): p. 5645-5658.
147. Aminzadeh, M. and D. Or, *Temperature dynamics during nonisothermal evaporation from drying porous surfaces*. Water Resources Research, 2013. **49**(11): p. 7339-7349.
148. Aminzadeh, M. and D. Or, *Energy partitioning dynamics of drying terrestrial surfaces*. Journal of hydrology, 2014. **519**: p. 1257-1270.
149. Thiery, J., et al., *Drying regimes in homogeneous porous media from macro-to nanoscale*. Physical Review Fluids, 2017. **2**(7): p. 074201.
150. Moldrup, P., et al., *Predicting the gas diffusion coefficient in repacked soil water-induced linear reduction model*. Soil Science Society of America Journal, 2000. **64**(5): p. 1588-1594.
151. Chakraborty, P.P., et al., *Evaporative Drying from Hydrophilic or Hydrophobic Homogeneous Porous Columns: Consequences of Wettability, Porous Structure and Hydraulic Connectivity*. Transport in Porous Media, 2022: p. 1-28.
152. Jury, W. and J. Letey Jr, *Water vapor movement in soil: Reconciliation of theory and experiment*. Soil Science Society of America Journal, 1979. **43**(5): p. 823-827.
153. Cary, J., *ONSAGER'S RELATION AND THE NON-ISOTHERMAL DIFFUSION OF WATER VAPOR*. The Journal of Physical Chemistry, 1963. **67**(1): p. 126-129.
154. Lu, S., et al., *A method to estimate the water vapour enhancement factor in soil*. European Journal of Soil Science, 2011. **62**(4): p. 498-504.
155. Pietsch, W. and H. Rumpf, *Haftkraft, kapillardruck, flüssigkeitsvolumen und grenzwinkel einer flüssigkeitsbrücke zwischen zwei kugeln*. Chemie Ingenieur Technik, 1967. **39**(15): p. 885-893.
156. Zhu, H., et al., *Discrete particle simulation of particulate systems: theoretical developments*. Chemical Engineering Science, 2007. **62**(13): p. 3378-3396.
157. Lian, G., C. Thornton, and M.J. Adams, *A theoretical study of the liquid bridge forces between two rigid spherical bodies*. Journal of colloid and interface science, 1993. **161**(1): p. 138-147.

158. Chakraborty, P.P., et al. *Liquid Transport During Evaporation of Water From a Small Simulated Soil Column*. in *Heat Transfer Summer Conference*. 2019. American Society of Mechanical Engineers.
159. Boelter, L., H. Gordon, and J. Griffin, *Free evaporation into air of water from a free horizontal quiet surface*. *Industrial & Engineering Chemistry*, 1946. **38**(6): p. 596-600.
160. Bower, S. and J. Saylor, *A study of the Sherwood–Rayleigh relation for water undergoing natural convection-driven evaporation*. *International Journal of Heat and Mass Transfer*, 2009. **52**(13-14): p. 3055-3063.
161. Goldstein, R.J., E.M. Sparrow, and D. Jones, *Natural convection mass transfer adjacent to horizontal plates*. *International Journal of Heat and Mass Transfer*, 1973. **16**(5): p. 1025-1035.
162. Lloyd, J. and W. Moran, *Natural convection adjacent to horizontal surface of various planforms*. 1974.
163. Suzuki, M. and S. Maeda, *ON THE MECHANISM OF DRYING OF GRANULAR BEDS Mass Transfer from Discontinuous Source*. *Journal of chemical engineering of Japan*, 1968. **1**(1): p. 26-31.
164. Kumar, N. and J.H. Arakeri, *Experimental and numerical investigation of evaporation from line sources of water in low porosity surfaces*. *Journal of Hydrology*, 2019. **569**: p. 795-808.
165. Yiotis, A., et al., *Analytical solutions of drying in porous media for gravity-stabilized fronts*. *Physical Review E*, 2012. **85**(4): p. 046308.
166. Carey, V.P., *Liquid-vapor phase-change phenomena: an introduction to the thermophysics of vaporization and condensation processes in heat transfer equipment*. 2018: CRC Press.
167. Rogers, J. and M. Kaviany, *Variation of heat and mass transfer coefficients during drying of granular beds*. 1990.
168. Carman, P.C., *Fluid flow through granular beds*. *Trans. Inst. Chem. Eng.*, 1937. **15**: p. 150-166.
169. Kozeny, J., *Über kapillare leitung der wasser in boden*. Royal Academy of Science, Vienna, Proc. Class I, 1927. **136**: p. 271-306.
170. Lake, L.W., et al., *Fundamentals of enhanced oil recovery*. Vol. 1. 2014: Society of Petroleum Engineers Richardson, TX.
171. Koch, K., A. Revil, and K. Holliger, *Relating the permeability of quartz sands to their grain size and spectral induced polarization characteristics*. *Geophysical Journal International*, 2012. **190**(1): p. 230-242.
172. Mavko, G. and A. Nur, *The effect of a percolation threshold in the Kozeny-Carman relation*. *Geophysics*, 1997. **62**(5): p. 1480-1482.
173. Johnson, D.L., J. Koplík, and L.M. Schwartz, *New pore-size parameter characterizing transport in porous media*. *Physical review letters*, 1986. **57**(20): p. 2564.
174. Chapuis, R.P. and M. Aubertin, *On the use of the Kozeny Carman equation to predict the hydraulic conductivity of soils*. *Canadian Geotechnical Journal*, 2003. **40**(3): p. 616-628.